Dissertation

submitted to the
Combined Faculties for the Natural Sciences and for Mathematics
of the Ruperto-Carola University of Heidelberg, Germany
for the degree of
Doctor of Natural Sciences

presented by
Diplom-Physiker Olivier La Schiazza
born in Luxembourg, Luxembourg

Oral examination: June 18th, 2008

Fast Two-Photon Excited Fluorescence Imaging for the Human Retina

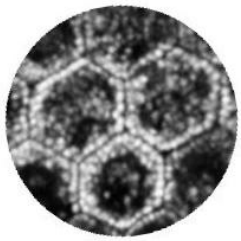

Referees: Prof. Dr. Josef F. Bille
Prof. Dr. Dr. Christoph Cremer

Zusammenfassung

In der vorliegenden Doktorarbeit wird ein neuartiges Zwei-Photonen-Mikrosokop, basierend auf einem schnellen ophthalmoskopischen Scanner, zur hochauflösenden strukturellen und funktionellen Abbildung der menschlichen Netzhaut entwickelt und aufgebaut. An menschlichen Spenderaugen werden die Autofluoreszenzeigenschaften der Netzhaut erprobt und auf ihren diagnostischen Wert hin analysiert. Die sich auf dem retinalen Pigmentepithel (RPE) mit Alter und Krankheit ansammelnde Lipofuszingranula können dabei hochauflösend mit Hilfe der Zwei-Photonen-Anregung abgebildet werden. Exzessive Lipofuszinmengen im RPE werden in der Ophthalmologie als mögliche Ursache für die Pathogenese u.a. der altersabhängigen Makulardegeneration (AMD) vermutet und dessen hochauflösende, selektive Anregung mittels Zwei-Photonen-Absorption erscheint besonders interessant. Zudem ist es erstmals möglich, die feinen Photorezeptor Zapfen und Stäbchen sowie die darüberliegenden Ganglionzellen und Nervenfaserschicht der neurosensorischen Netzhaut mittels Zwei-Photonen-Autofluoreszenz darzustellen, allerdings sind dazu höhere Anregungsenergien nötig. Desweiteren wird die Abhängigkeit von kurzen Pixelverweilzeiten auf die Fluoreszenzausbeute untersucht. Am RPE Lipofuszin wird experimentell nachgewiesen, dass vermutlich aufgrund von unterdrückter Tripletzustand-Ansammlung, durch schnelles Scannen eine Fluoreszenzsignalzunahme erzielt werden kann. Zuletzt wird die potenzielle Anwendung am lebenden menschlichen Auge zur diagnostischen Abbildung der RPE Zellschicht simuliert und diskutiert. Die Anwendung der Zwei-Photonen Scanning-Laser-Ophthalmoskopie erscheint unseren Berechnungen, nach neuesten Lasersicherheitsbestimmungen, zufolge als nichtinvasiv.

Abstract

In the present dissertation, a novel two-photon microscope, based on a fast ophthalmoscopic scanning unit, is designed and developed for high-resolution structural and functional imaging of the human retina. The autofluorescence properties of the retina from human donor eyes are studied for their diagnostic value. It is shown that single lipofuscin granules, which accumulate with age and disease on the retinal pigment epithelium (RPE), can be selectively imaged at high resolution by two-photon exited fluorescence. Excessive levels of lipofuscin within the RPE have been hypothesized to be responsible for the pathogenesis of retinal disorders such as age-related macular degeneration (AMD), and their direct visualization appears particularly attractive to ophthalmology. It is also found possible to image the subtle photoreceptor cones and rods as well as the overlying ganglion cells bodies and nerve fiber layer of the neural retina by two-photon excited autofluorescence, however at the expense of higher excitation energies. Furthermore we probe the influence of short pixel dwell times on fluorescence yield. An increase in two-photon excited fluorescence signal from RPE lipofuscin is experimentally found upon fast scanning, presumably as a result of repressed triplet state build-up. Finally a potential application of the prototype as a diagnostic tool for imaging the RPE layer is simulated and discussed. According to our calculations following the newest laser safety regulations, two-photon scanning laser ophthalmoscopy appears to be non-invasive.

Contents

1 Introduction

Most of our daily activities rely on a proper vision and any loss in visual acuity strongly influences our quality of life. One of the main concerns in ophthalmology is the preservation of vision throughout an individual's lifetime. Regarding the ever-increasing life span of human population in technologically advanced countries, this has become a more and more challenging task. In the aging eye, vision is compromised by an increased incidence of age-related degenerative diseases. In particular, age-related macular degeneration (AMD) is the most frequent cause for legally registered untreatable blindness in the developed countries. About 35% of the human population over the age of 75 years has some degree of AMD [Bok, 2002], a number that is expected to nearly double in the next twenty years unless effective interventions are developed.

AMD affects the macula, the region of the retina responsible for central visual acuity. It was first described by Donders in 1855 [Donders, 1855]. Although many studies are ongoing since, there is little knowledge about the precise origins and mechanisms that trigger this multifactorial disease, which results in a progressive irreversible degeneration of ocular structures in the macular region (choriocapillaries, Bruch's membrane, RPE, photoreceptors). This also explains the lack of effective therapeutic treatments against AMD, and every new imaging technique able to yield high in vivo structural and functional information of the ocular fundus with the potential to provide new insights in its pathogenesis is highly welcome.

Since the invention of the first ophthalmoscope by Hermann von Helmholtz in 1851 [von Helmholtz, 1851], the quest for quantitative in vivo image recordings of the ocular fundus for diagnostic and monitoring purposes was initiated. Boosted by the newest developments in microscopy, the state-of-the-art confocal scanning laser ophthalmoscope [Webb et al., 1987] proved itself as indispensable workhorse in clinical practice. By means of fluorescence microscopical techniques, which were originally designed for angiography, it became recently possible to quantify retinal health based on its fluorescence properties [Delori et al., 1990; von Rückmann et al., 1995; Delori et al., 1995a]. These are mainly derived from lipofuscin accumulating with age and disease on the RPE cells as a byproduct of incomplete cellular digestion of photoreceptor outer segment discs [Boulton et al., 1989]. Alterations in RPE lipofuscin are features of the pathophysiology of degenerative retinal diseases. A number of hereditary retinal diseases such as Stargardt's and Best's disease, but also AMD have been recognized to be associated with an excessive accumulation of lipofuscin, mimicking an accentuation of the aging process. It is therefore

widely believed among ophthalmologists that the metabolic functioning of the RPE cells is correlated with the amount of lipofuscin present and that a consequent impairment of the RPE cells may precede or coexist with the earliest stages of pathology in AMD. However, conclusive evidence for a causal link yet remains to be found.

As lipofuscin is strongly fluorescent upon blue light excitation, fundus autofluoresence measurements allow a direct non-invasive visualization of the pathological and functional state of the retina by highlighting defects and alterations in the RPE that remained unrevealed by traditional imaging techniques of fundus photography or simple ophthalmoscopy. Areas of increased autofluorescence may identify metabolically stressed RPE cells that are prone to dysfunction or loss.

Fundus autofluorescence imaging is therefore not only valuable in the diagnostic and monitoring of dynamic changes of RPE-related diseases, but also helps in the identification and classification of characteristic atrophy patterns in the search for cross-correlations to other pathologies and possible genetic factors of influence. It may further help to assess cell viability after RPE transplantation or pharmacological treatments that target the RPE.

Current fluorescence imaging tools however are not able to resolve the RPE on a cellular level. This is partially owing to a lack of effective resolution, as well as to strongly scattered or absorbed blue excitation light in the different layers of the human eye. This limits fundus autofluorescence measurements to the mapping of topographic distribution in search of areas of relative hyper- or hypo-autofluorescence.

With the introduction of ultrafast pulsed laser sources, two-photon excited fluorescence (TPEF) microscopy became practically feasible for the first time in 1990 [Denk et al., 1990], and experienced a tremendous success in biological microscopy since. Due to the simultaneous absorption of two lower energy (i.e. longer wavelength) photons, two-photon excited fluorescence microscopy provides a substantially increased sensing depth and reduced photodamage as compared with single-photon microscopical techniques. As a second-order effect, the fluorescence emission depends on the square of the excitation intensity. Consequently, two-photon absorption is only confined to the focal plane, resulting in an intrinsic three-dimensional diffraction-limited resolution providing highly selective optical sectioning in thick tissue without the practical constraints on resolution implied by a confocal pinhole.

Regarding these unique characteristics of TPEF and the transparency of the human eye to near-infrared (NIR) light, nonlinear retinal imaging has huge potential in developing novel high-resolution diagnostic methods in ophthalmology for the study of RPE-related metabolic alterations on a cellular and subcellular level, in order to enhance the understanding of the normal and diseased retina.

In the present dissertation this novel approach for retinal imaging is explored. It focuses on the design and development of a nonlinear microscope, based on the fast scanning and detection unit of a conventional scanning laser ophthalmoscope modified for high

optical 'zooming' to study the feasibility of two-photon excited fluorescence to provide structural and functional information of the human retina for a potential non-invasive in vivo application in fundus autofluorescence imaging. This will allow the direct observation of malignant changes on a cellular level preceding degenerative retinal pathologies, and help to design effective therapies at early stages of the disease.

After this introduction, Chapter 2 gives an overview of the anatomical and physiological basics of the human retina and the retinal pigment epithelium (RPE) in order to provide the biomedical context of this dissertation.
In Chapter 3, the physical background with the relevant theoretical and experimental fundamentals of fluorescence microscopy are presented. After an introduction to the basics of light microscopy, the physical principles of single- and two-photon excited fluorescence are outlined from an empirical and theoretical quantum mechanical point of view. Their practical realizations in fluorescence confocal laser scanning microscopy and two-photon excited fluorescence microscopy are further discussed.
Chapter 4 deals with the details of the design and technical implementation of the novel video-rate scanning two-photon ophthalmoscope-based microscope realized during this dissertation.
The first applications of fast two-photon excited fluorescence imaging on human donor eyes with the newly designed prototype are presented and discussed in Chapter 5. The RPE cells and the neural retina were investigated for endogenous fluorophores with diagnostic value.
In Chapter 6, the influence of a fast scanning illumination scheme on fluorescence yield is experimentally tested on a commercial two-photon microscope (Zeiss LSM 510 NLO) with variable scanning speed. A possible photophysical model considering triplet-state relaxation is discussed.
The performance of an optical imaging system for the living retina is ultimately limited by the eye's focusing optics. In Chapter 7, the expected resolution in the living emmetropic human eye for imaging RPE cells is simulated and the relevant laser safety limits of a potential nonlinear scanning laser ophthalmoscope are discussed according to the ANSI Z136.1-2000 Standard.
The dissertation closes with a summary and draws some conclusions toward a clinical in vivo application of two-photon excited fluorescence microscopy in the human eye.

2 The Human Retina

This chapter provides an overview of the anatomy and physiological functions of the retina and the underlying retinal pigment epithelium (RPE), in order to present the biomedical context for the work to follow.

2.1 Overview

A schematic of the human eye is shown in Figure 2.1. Light entering the eye is focused by the eye's refractive components, i.e. the cornea and the lens, through the anterior chamber and the vitreous onto the retina, the light sensitive tissue of the eye. The amount of light that reaches the retina is regulated by the size of the pupil, defined by the iris. At the retina, light triggers a photochemical process which evokes the neural impulses that lead to vision. The retina is an extension of the central nervous system and is directly connected to the brain by the optic nerve. The central processing system of the human visual system is the visual cortex in the brain but there are many intermediate processing centers located within the neural retina itself that will be discussed in the next section.

The total retina is a circular disc of approximately 42 mm diameter and 0.5 mm thickness. In the central part of the retina is located the optic disc, a circular to oval area measuring about 2.5 mm in diameter (5° wide horizontally and 7° wide vertically). From the center of the optic disc radiate the major blood vessels of the retina. 15° temporally and 1.5° downwards relative to the center of the optic disc, is located the fovea, which is the center of a 5.5 mm diameter (19°) area known as the macula.
The macula has a yellow pigmentation due to the presence of anthophyll carotenoids, zeaxanthin and lutein, present in the cone axons in that area, which are thought to act as a protective short wavelength filter - additionally to that of the lens.

2.2 The Neural Retina

2.2.1 Anatomy and Physiology

Figure 2.2 shows a schematic cross-section through the human retina emphasizing the nerves an their interconnections. It consists of a number of cellular and pigmented layers, and a nerve fiber layer that form together the neural part of the retina in which light is

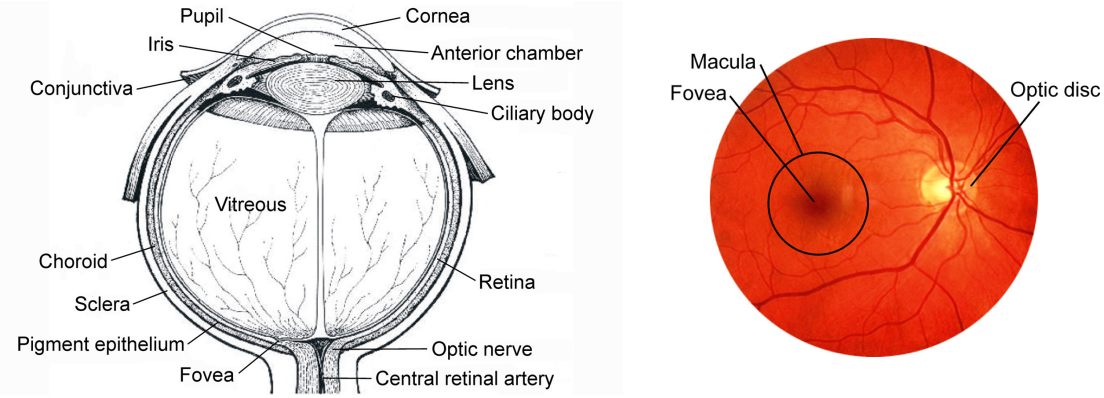

Figure 2.1: *Left hand side:* Horizontal section of the human eye highlighting its major components. *Right hand side:* View on the retina as seen by the ophthalmologist.

absorbed and converted to chemical and electrical potentials to be proceeded as visual impulse via the optic nerve to the brain.

Before reaching the light sensitive photoreceptors, light passes through a number of layers involved in signal transduction: the nerve fiber layer, the ganglion cell layer, the inner plexiform layer, the inner nuclear layer, the outer plexiform layer, and the outer nuclear layer.

The light sensitive cells at the back of the retina are the photoreceptors. They exist as two types, known as *rods* and *cones*. Their name refers to their shape but considerable variations in form occur with location, and it is not always possible to distinguish between the two types on this basis. There are about 6.5 million cones and 120 million rods in the human retina.
In general, rods are longer and narrower than cones. They are often described as low-level light sensitive detectors, which is mainly due to their neural wiring in comparison with the cones. The retinal network of the rods is such that about 100 rods are interconnected to produce a total combined output to the brain. This gives the rod system high sensitivity but poor spatial resolution. In contrast, the output of only a few cones is combined, so that the cone system functions at higher light levels but offers a higher spatial resolution. The cones are further subdivided in three types, each with different wavelength-sensitivities - the L (long), M (medium) and S (short) cones - which gives the conditions for color-vision.
At moderate to high light levels, vision is dominated by the cones and their spectral response is referred to as *photopic response*. S-cones have an absorption maximum at 420 nm, M-cones at 535 nm, and L-cones maximally absorb at 565 nm. At low light levels (i.e. at night), rods dominate vision and we are unable to distinguish between colors. This is known as the *scotopic response*. The peak wavelength of the scotopic response

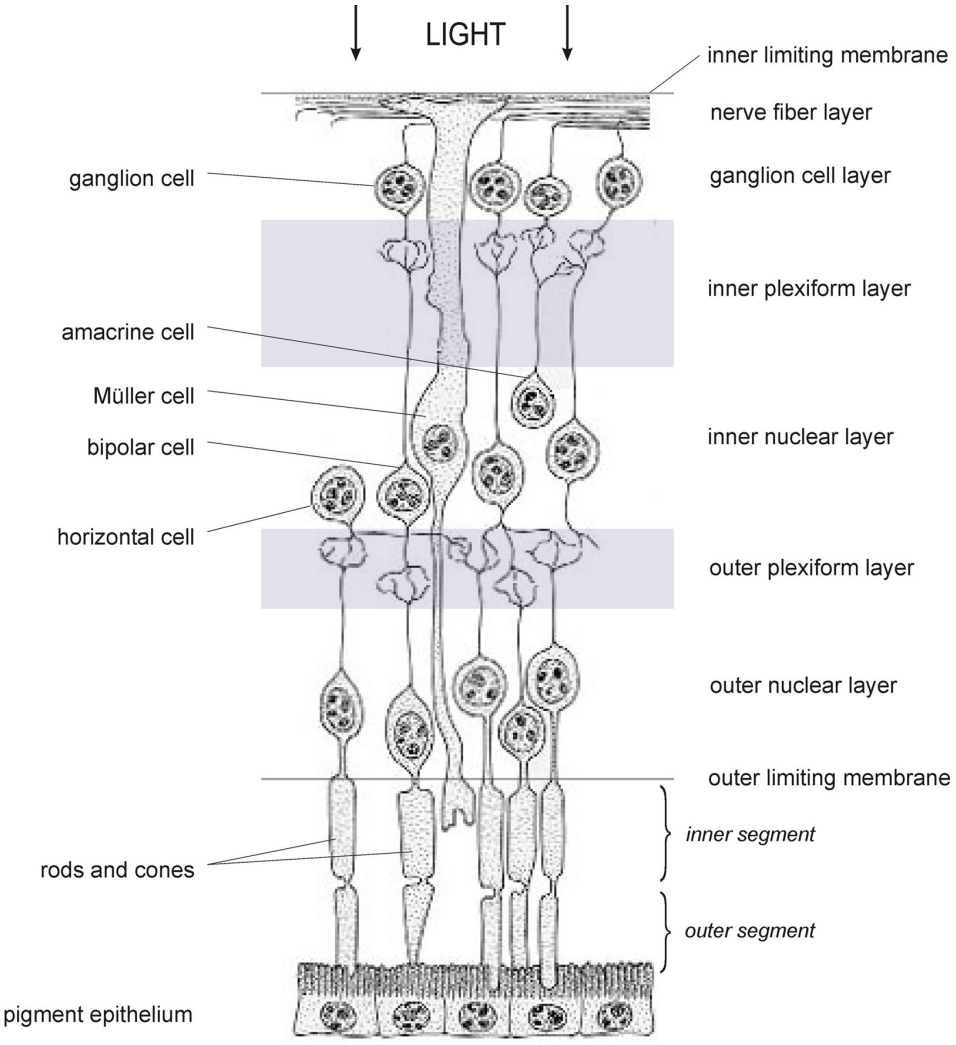

Figure 2.2: Cell layers of the human retina in a vertical section.

is at approximately 500 nm, and spectrally blue shifted compared to the photopic sensitivity. The rods as well as the L- and M-cones have a second absorption maximum at 350 nm, which is however functionally blocked by the transmission properties of the ocular media.

In the fovea, the layers overlying the photoreceptors are displaced concentrically, leaving only the receptors with their cell bodies, giving it a pit-like structure. This configuration allows most light to reach the photoreceptors. The 0.5° central part of the foveal pit is named the *foveola*, an avascular region of highest resolution. It has the highest concentration of cone photoreceptors and is responsible not only for color vision but also for vision of the greatest acuity as the cones (with elongated outer segments) are thinner (2.3 µm in diameter) and packed very tightly (2.5 µm intercone spacing) in a hexagonal mosaic. The foveola is free of rods. Toward the periphery, the density in cones is decreasing whereas the density in rods increases.

Rods and cones consist of a synaptic region (located in the outer plexiform layer), a nuclear region (located in the outer nuclear layer), an inner segment (containing the metabolic machinery of the cell, including mitcohondria, RER and Golgi), and an outer segment (containing the light sensitive membrane discs). The inner an outer segments are joined by a narrow channel containing a sensory cilium for the transport of newly synthesized proteins (opsins) from their site of synthesis in the inner segments to the site of assembly in the photoreceptive membranes of the outer segments.

The photoreceptor axons contact the dendrites of bipolar cells and horizontal cells. Horizontal cells are interneurons that interconnect groups of photoreceptors and aid in signal processing. The bipolar cells in the inner nuclear layer process the input from photoreceptors and horizontal cells. They transmit the signal to their axons in the inner plexiform layer where they contact with ganglion cell dendrides and amacrine cells, another class of interneurons that interconnect groups of ganglion cells and bipolar cells.

The ganglion cell layer contains the nuclei of the ganglion cells, which integrate the incoming impulses to one single impulse. They possess long axons, the nerve fibers, that course radially to the papilla where they bundle together to form the optic nerve (Figure 2.3), containing around 10^6 nerve fibers [Reim, 1993], from where the message concerning the visual image is transmitted to the brain. At the optic disc all photoreceptors and accessory cells are absent so that the nerve fibers can penetrate the choroid and the sclera where they leave the eyeball for the brain.

The different layers of the neural retina are kept together by connective gial cells, which are mainly astrocytes and Müller cells that distribute along the entire retina. Astrocytes originate embryonically from the optic nerve head and subsequently migrate to their final site in the retina. They distribute along the entire retina except in the nonvascular area of the fovea with lower densities found in the periphery, around the level of the nerve fiber layer and ganglion cell layer [Ogden, 1978]. They function as the metabolic and structural support of the nerve fibers.
Müller cells are the main glial cells of the neural retina. They span radially across the

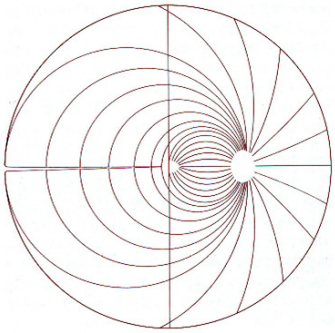

Figure 2.3: Course of the nerve fibers in the retina. All nerve fibers proceed radially to the papilla where they form the optic nerve, and their density is highest. After [Duke-Elder, 1961], modified from [Reim, 1993].

entire retina with their cell bodies located in the inner nuclear layer and their endings forming the inner and outer limiting membranes. The outer limiting membrane forms a barrier between the subretinal space, into which the inner and outer segments of the photoreceptors project to be in close association with the pigment epithelial layer behind the retina, and the neural retina proper. The inner limiting membrane is the inner surface of the retina, bordering the vitreous humor, and thereby forming a diffusion barrier. Müller cells provide the structural support of the retina and are also believed to function in the maintenance of retinal integrity by supporting photoreceptor and ganglion cell survival by yet unknown mechanisms [Zhong et al., 2007].

The vascular supply to the outer layers of the retina is provided by the choroid, which lies in between the retina and the sclera. The choroid contains large blood vessels optimized for very high flow rates. The vascular supply to the inner retinal layers, i.e. the ganglion cell layer and the inner nuclear layer, is provided by the central retinal artery that emanates from the optic nerve. It pierces the optic disc close to the eyeball, sending four main branches over the internal surface of the retina where they distribute in the ganglion cell layer, curving toward and around the blood vessel- and capillary-free central fovea.

2.2.2 Signal Transduction

Light of the visible wavelength is absorbed in the visual pigments located in the flattened membrane sacs of the photoreceptor outer segments. The undulating membranes of the cones contain the photopigment *photopsin* (photopsin I, photospsin II, photopsin III in the L-, M-, S-cones, respectively), while the discs of the rods contain the visual pigment, *rhodopsin*. The mechanism by which light energy is converted to neural signals is identical in rods and cones. What differs is the specific spectral sensitivity of the two types of receptors. Accordingly, the following description of visual signal transduction is explained using the example of rods, which are by far the more prominent photoreceptors in the human retina.
Every incident photon is source of a cascade of absorption processes in the layered discs,

each resulting in a photochemical reaction of the photopigment.
Rhodopsin is a complex of a glycoprotein opsin and a bound chromophore retinal, an aldehyde of vitamin A (retinol). The main molecular conversion upon absorption of light is an isomerization from 11-*cis*-retinal to all-*trans*-retinal. This event breaks apart activated rhodopsin (metarhodopsin II), an enzyme which acts to activate a second membrane-bound protein known as transducin. Transducin is in its turn an enzyme activating phosphodiesterase, a third enzyme in the cascade, capable of hydrolyzing cyclic GMP (cGMP), which leads to a transient closing of the plasma membrane bound cGMP-gated sodium channels (which are open in the resting state) and a consequent *hyperpolariation* of the photoreceptor plasma membrane. This hyperpolarization results in a *reduced* release of the neurotransmitter glutamate from the photoreceptor cell synaptic terminals. The release of neurotransmitter at the synapse and the resulting response is proportional to the incident light intensity. The activated state is in turn terminated by phosphorylation by rhodopsin kinase and subsequent binding of arrestin. Inactive rhodopsin binds again 11-*cis*-retinal, so that it can once more be activated by absorption of light.

The connections between the photoreceptors and the brain, are mediated through the various layers of the retina in such a way that the actual input to the brain is controlled by the neural circuitry with corresponding receptive fields. The neural circuitry is very complex and only a short overview should be given here.

Rod and cone photoreceptors synapse with integrator neurons in the outer plexiform layer. There are two types of such neurons and the pathway by which the signal is processed is different for rods and cones. Horizontal cells, whose communication is entirely within the outer plexiform layer, connect to the rods and cones, and to the bipolar cells. Bipolar cells can receive the signal directly from a photoreceptor cell or via the mediation of a horizontal cell. Horizontal cells are specialized cells that have an inhibitory output, and because of being connected laterally to numerous bipolar and photoreceptor cells, they can selectively suppress the generation of information along some pathways and routes with the purpose to increase vision acuity. Bipolar cells, on their hand, can hyperpolarize (*off-center response*) or depolarize (*on-center response*), depending on their type. The different responses of these types of bipolar cells is due to different types of post-synaptic glutamate receptors. They can thus send two sorts of signals via the ganglion cells to the brain which has the capacity to interpret both differently. This mechanism allows for two types of signals to be sent, and also enhances the lateral inhibition phenomenon. The axons of the bipolar cells synapse with the amacrine cells and ganglion cells in the inner plexiform layer. The amacrine cells mediate signals between bipolar cells, other amacrine cells, and ganglion cells. The ganglion cells are the final signal transmitting neurons in the retina. Their output signal is directly processed to the visual cortex via the optic nerve that collects all the axons of the ganglion cells. They receive input from either the bipolar cells or the amacrine cells. The bipolar cells connected to the rods, transmit their signal to the ganglion cells via an amacrine cells which spreads out the rod signal before converging on ganglion cells. The cone-bipolar cells

directly synapse with ganglion cell dendrites and the signal pathway is therefore more direct, more narrow-field and more convergent than the rod pathway. Fewer cones converge onto cone-bipolars than rods to rod-bipolars and only a relatively small number of cone bipolar cells converge onto their corresponding ganglion cells - another phenomena that helps to increase spatial resolution.

2.3 The Retinal Pigment Epithelium (RPE)

2.3.1 Role of the RPE in Visual Function

The outer segments of the photoreceptors are directly anterior to the retinal pigment ephithelium (RPE), a single layer of pigmented hexagonal cells that forms part of the blood/retina barrier. The RPE cells have a diameter of approximately 15 µm and a height of 9–12 µm, in the macular area [Eichner, 1958]. When viewed in section, each cell consists of an outer non-pigmented part containing a large oval nucleus and an inner pigmented portion. The basolateral membrane of the RPE faces Bruch's membrane which forms the basement membrane separating the RPE from the cellular components of the blood from the underlying choroid. The apical membrane of the RPE extends numerous long projections (microvilli) upward around the photoreceptor outer segments, establishing a complex of close interaction.

The RPE is a dark pigmented cover of the inner bulbus that aids in the absorption of scattered light, which is mediated via melanin in the melanosomes. It forms the outer blood-retinal barrier and supports the metabolic functioning and integrity of the photoreceptors. Both form together one functional unit with integrated interaction. The proper functioning of the RPE is therefore essential for vision.

Nutritional metabolites such as glucose, oxygen and fatty acids can diffuse from the choroid to the photoreceptors via the RPE cells. On the other hand, the RPE also transports water, electrolytes and metabolic end products from the subretinal space to the blood. Microvilli maximize the apical surface of interaction for this epithelial transport.

Retinal, the light sensitive component in the photoreceptors outer segments (POS), is constantly cycled between photoreceptors and RPE. The POS are unable to convert all-*trans*-retinal back into 11-*cis*-retinal after photodetection. In a first step, all-*trans*-retinal is released in the cytosol of the photoreceptors where it is reduced to all-*trans*-retinol by a membrane-bound retinol dehydrogenase. All-*trans*-retinol is then carried to the RPE cells where it is reisomerized to all-*cis*-retinol to regenerate 11-*cis*-retinal that is transported back to the photoreceptors via carrier molecules (retinal binding proteins, IRBP) to rebind to opsin and serve its function for light transduction, so that vision is possible again. In this way, the RPE ensures constant excitability of the photoreceptors. This process of regenerating the visual pigment rhodopsin, is called the *visual cycle*. A detailed description of the involved reactions can be found in [Strauss, 2005].

The other important function of the RPE in the maintenance of the photoreceptors is the constant renewal of photoreceptor outer segments that are exposed to intense light levels causing photodamage to proteins and lipids and containing photooxidative radicals from retinal. The outermost stacks of discs are continually shed and consumed by the apical processes of the RPE cells. In the RPE the phagocytised discs are digested in the lysosomes with the help of some 40 lytic enzymes. New discs are build from their bases at the cilium. Important molecules such as retinal and docosahexaenoic acid are recycled and redelivered to the photoreceptors, similar to the pathway described in the visual cycle.

The process of phagocytosis occurs in a 24 hour circadian rhythm. The rate of disc shedding is greatest in the morning. The renewal and phagocytosis of the POS by the RPE is tightly coordinated in order to maintain a constant POS length. The turnover rate for an entire POS to be renewed is ten days.

2.3.2 RPE Lipofuscin

In the RPE cells, lipofuscin accumulates within residual bodies (lipofuscin granules) of the lysosomal compartments mainly as a byproduct of phagocytosis of shed photoreceptor outer segments [Boulton et al., 1989] from indigestible end-products that cannot be degraded by the lysosmal enzymes. Lipofuscin is a heterogeneous mixture of lipids, proteins, and different fluorescent pigments [Kennedy et al., 1995]. The most prominent fluorophore of lipofuscin has been positively identified as A2-E, a pyridinium bisretinoid which is a product of the reaction of all-*trans*-retinal with ethanolamine [Eldred and Lasky, 1993; Eldred, 1993] both of which are components of the photoreceptor outer segments.

When exposed to blue light, lipofuscin is potentially toxic to the cell as it can act as a sensitizer for the generation of reactive-oxygen species (ROS) including oxygen ions, free radicals, and peroxides [Gaillard et al., 1995; Rózanowska et al., 1995; Boulton et al., 2004]. It has been shown that an accumulation of A2-E in the RPE cells affects the lysosomal metabolism by deranging the acidic environment. This potentially impairs lysosomal enzymatic capacity and consequently leads to an accumulation of undegraded material [Holz et al., 1999]. A2-E was also demonstrated to be a significant contributor to lipofuscin's phototoxicity, causing blue-light mediated disruption of lysosomal membranes [Schütt et al., 2000] and RPE cell death by means of apoptotic mechanisms [Sparrow et al., 2000]. Constituents of human lipofuscin other than A2-E able to induce photostress to the RPE have been reported as well, although of unknown origin, corroborating lipofuscin's phototoxic properties [Avallet et al., 2005; Pawlak et al., 2002].

Lipofuscin in the RPE cells increases with age, and is greatest in the macula [Feeney-Burns et al., 1984], presumably because of the higher density of photoreceptors as well as higher photon absorption and the consequent increased phagozytic and metabolic load

on the RPE in this area [Dorey et al., 1989]. It has been hypothesized that excessive levels of lipofuscin turn out noxious for the cell, leading to retinal degeneration with consequent vision loss [Dorey et al., 1989]. Age-related lipofuscin accumulation is accompanied with a decline of melanin granules in the RPE cells [Feeney-Burns et al., 1984]. Loss of melanin, which is thought to have a photoprotective function [Sarna, 1992], makes the RPE even more vulnerable to incident light and free radical damage.
While lipofuscin in general accumulates with age, excessive accumulations have been linked to a number of retinal degenerative and hereditary pathologies, including Best's disease [Weingeist et al., 1982], Stargardt's disease (juvenile macular degeneration) [Delori et al., 1995b], and age-related macular degeneration (AMD). Especially in AMD, abnormal lipofuscin accumulations topologically correlate with histopathological indicators of disease and functional loss of retinal sensitivity [Dorey et al., 1989; Schmitz-Valckenberg et al., 2004]. However, conclusive evidence for a causal link between lipofuscin and RPE atrophy has not yet been found.

2.4 Age-Related Macular Degeneration (AMD)

Age-related macular degeneration (AMD) is characterized by the progressive degeneration of the RPE in the macular region and a consequent impairment of the relevant photoreceptor cells, which results in an irrevocable loss of central vision. It is the major cause for untreatable blindness in developed countries. Around 35% of the human population over 75 years has some degree of AMD [Bok, 2002]. The pathogenesis of this complex ocular disease is, however, poorly understood.
The first clinical indication of AMD is the extracellular accumulation of drusen (waste material) between the RPE and Bruch's membrane. Clinicians divide drusen in two forms depending on their size and morphology: "hard" drusen, frequently associated with the nonneovascular (atrophic, dry) form of AMD, and "soft" drusen that are most often associated with the neovascular (exudative, wet) form of AMD. A fundus photography of both forms of AMD is shown in Figure 2.4. The athropic form is generally characterized by a gradual, progressive degeneration of the RPE and photoreceptors, starting in the macular area. The advanced form of atrophic AMD over a large area is termed geographic athropy (GA) and can lead to a severe loss of vision. The exudative form is an advanced form of AMD that is characterized by the growth of new blood vessels from the choroid into the subretinal macular region as response to drusen. These new blood vessels are very fragile and usually leak fluid and blood, causing damage and a sudden vision loss. Choroidal neurovascularization (CNV) is controlled by a large number of modulating factors and presumably occurs due to an imbalance of pigment epithelium-derived factor (PEDF, an antiangiogenic factor) and vascular endothelial growth factor (VEGF, an angiogenic factor), both of which are derived from the RPE cells [Bhutto et al., 2006]. More than 80% of patients with intermediate or advanced AMD have the

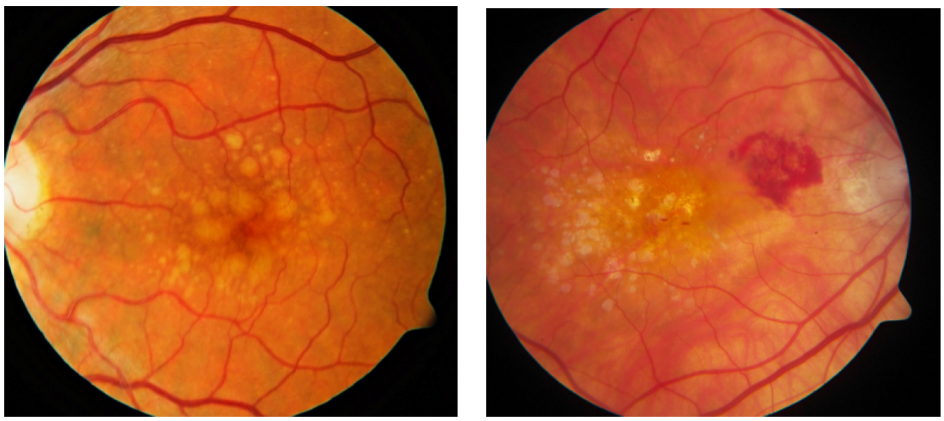

(a) (b)

Figure 2.4: Fundus photography of a retina suffering from dry age-related macular degeneration: discrete drusen are visible as yellow deposits in the deep layers of the macula (a). Advanced wet age-related macular degeneration: choroidal neurovascularization causes blood and fluid leakage into the subretinal space (b). Image source: [Bourla and Young, 2006].

dry form, which may progess to the more aggressive wet form [Nowak, 2006].

The origin of drusen formation remains controversial. One widely accepted hypothesis suggests that the drusen are formed as result of progressive death and/or exocytosis of the RPE cells [Suter et al., 2000], which may be mediated by the age-related accumulation of lipofuscin described above. Additionally, large drusen can establish diffusion barriers between blood vessels and the RPE, which reduce the oxygen and glycose supply, resulting in a further degeneration of involved photoreceptors.

Current treatments to avoid blindness in advanced AMD are limited and poorly effective, in part because the mechanisms that trigger the disease are not resolved. There are currently no established treatments for dry AMD, and most therapies target CNV including thermal laser coagulation, photodynamic therapy (PDT), and recently developed angiogenesis inhibitor (anti-VEGF) treatments that block the growth of new blood vessels [Hooper and Guymer, 2003].
Todays treatments help to slow down the secondary effects of AMD and avoid further vision loss, but there are no pharmacological modulations able to cure or target the origins of AMD.

3 Fluorescence Microscopy

Fluorescence microscopy has become the technique of choice to view structural and functional information in living specimens. The present chapter should provide a short overview of some basic concepts of light microscopy in terms of wave theory that are important for the following considerations. A brief introduction to the Maxwell equations for electromagnetic waves is followed by the important practical concepts of the point spread function and resolution. The second part of this chapter begins with an empirical description of the fluorescence process followed by its quantum mechanical analysis for both single- and two-photon excitation. Further, the experimental concepts of fluorescence microscopy, namely *confocal laser scanning microscopy* and *two-photon excited fluorescence microscopy* will be explained, as they are recent powerful developments for non-invasive three-dimensional biological imaging and form the framework of the present thesis.

3.1 Basics of Light Microscopy

3.1.1 The Electromagnetic Field

The behavior of the electromagnetic field, represented by the electric vector $\mathbf{E}$ and the magnetic vector $\mathbf{H}$, in material objects is described by the four Maxwell equations which relate the space and time derivatives of the electric displacement $\mathbf{D}$, the magnetic induction $\mathbf{B}$, and the electric current density $\mathbf{j}$

$$\mathrm{div}\mathbf{D} = \rho, \tag{3.1}$$

$$\mathrm{div}\mathbf{B} = 0, \tag{3.2}$$

$$\mathrm{rot}\mathbf{E} = -\frac{\partial \mathbf{B}}{\partial t}, \tag{3.3}$$

$$\mathrm{rot}\mathbf{H} = \mathbf{j} + \frac{\partial \mathbf{D}}{\partial t}, \tag{3.4}$$

where ρ is the electric charge density.
A homogeneous, isotropic and linear material under the influence of an electromagnetic

field is described by the material equations

$$\mathbf{D} = \epsilon\epsilon_0\mathbf{E}, \tag{3.5}$$

$$\mathbf{H} = \mu\mu_0\mathbf{B}, \tag{3.6}$$

$$\mathbf{j} = \sigma\mathbf{E}, \tag{3.7}$$

where ϵ_0 and ϵ are the dielectric permittivity in vacuum and material, respectively, μ_0 and μ are the magnetic permeability in vacuum and material, respectively, and σ is the specific conductivity.

In optics, the propagation of a light is described in materials (e.g. air, glass) that are transparent and must be electrical nonconductors ($\sigma = 0$). We can further confine our attention to that part of the space that contains no charges or currents, i.e. where $\rho = 0$ and $\mathbf{j}$=0. The Maxwell equation can than be rewritten in the form

$$\left(\Delta - \frac{1}{\tilde{c}^2}\frac{\partial^2}{\partial t^2}\right)\mathbf{E} = 0, \tag{3.8}$$

$$\left(\Delta - \frac{1}{\tilde{c}^2}\frac{\partial^2}{\partial t^2}\right)\mathbf{H} = 0. \tag{3.9}$$

These are standard equations of wave motion whose solution are the electromagnetic waves propagating with a velocity

$$\tilde{c} = \frac{c}{n}, \tag{3.10}$$

with $c = (\epsilon_0\mu_0)^{-1/2} = 3 \times 10^8$ m/s the speed of light in vacuum, and $n = \sqrt{\epsilon\mu}$ the refractive index.
The interaction behavior of electromagnetic waves with obstacles is described by diffraction theory which forms the very basis of optical image-forming systems [Born and Wolf, 1980].

3.1.2 The Point Spread Function

In microscopy the behavior of the electric field in the neighborhood of the focal plane of a circular lens is of particular practical interest. In the theory of a scalar wave function[1], the properties of a monochromatic image of a point source by a well-corrected circular lens are given by the three-dimensional diffraction limited light distribution near the focal plane that is derived from the Huygens-Fresnel principle to be [Born and Wolf, 1980]

$$h_A(v,u) = 2C\int_0^1 \exp\left(-\frac{iu}{2}\rho^2\right) J_0(\rho v)\rho d\rho, \tag{3.11}$$

[1] A complete description of the electromagnetic field requires the magnitude of the field vectors as well as their direction (polarization). However for the majority of problems encountered in optics an approximate description in terms of single complex scalar wave functions turns out sufficient [Born and Wolf, 1980].

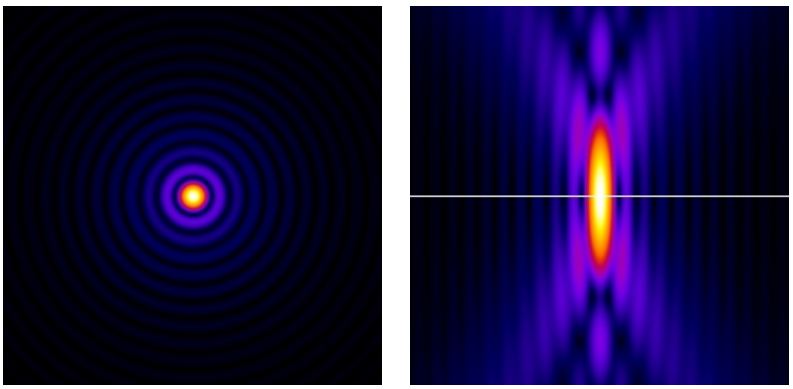

(a) lateral (b) axial

Figure 3.1: Simulated absolute value of the amplitude of the electric field in the focal region of a circular lens: along the focal plane (a); in the meridional plane of the optical axis, where the horizontal line denotes the plane of focus (b).

where

$$v = \frac{2\pi}{\lambda} r \sin(\alpha) \quad \text{and} \quad u = \frac{2\pi}{\lambda} z \sin^2\left(\frac{\alpha}{2}\right) \tag{3.12}$$

are the respective axial and radial normalized optical coordinates in the image plane, with $r = \sqrt{x^2 + y^2}$, λ the wavelength of light and $\mathrm{NA} = \sin(\alpha)$ the lens' numerical aperture. J_0 denotes the zero-order Bessel function, ρ the normalized radius of the aperture, C a constant that gives the electromagnetic field at the geometrical focus ($u = v = 0$) and may be dropped as one is usually only interested in relative distributions.
Equation (3.11) represents the strength of the electromagnetic field in the image plane for a single point object and is called the *amplitude point spread function* (PSF). It describes the response of an optical system to a point source and is an useful tool to quantify its optical performance.
The absolute value of expression (3.11) in the geometrical focal plane ($u = 0$), and along the optical axis ($v = 0$) is shown in Figure 3.1.

However we cannot observe amplitude variations directly. Light detectors usually detect the intensity distribution, which is the squared modulus of the electric field. Accordingly the *intensity PSF* is the squared modulus of the amplitude PSF and gives the intensity distribution of the image for a single point object near the focal plane

$$h(v,u) = |h_A(v,u)|^2 = h_A(v,u)h_A^*(v,u). \tag{3.13}$$

Figure 3.2 gives a graphical illustration of the intensity distribution in the geometrical focal plane, and along the optical axis of an aberration-free circular lens. The central

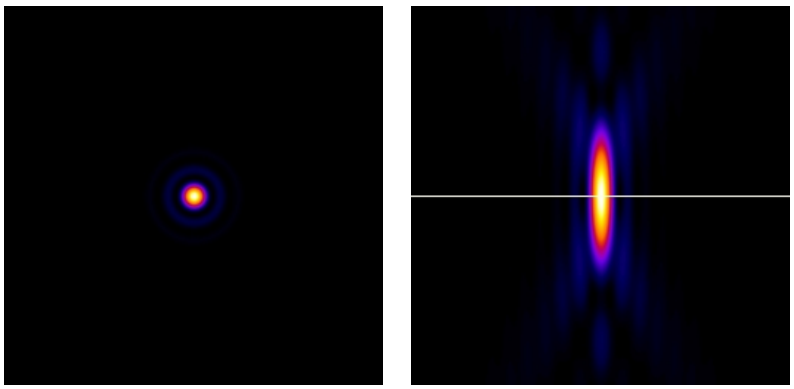

(a) lateral (b) axial

Figure 3.2: Simulated intensity distribution in the focal region of a circular lens: along the focal plane (a); in the meridional plane of the optical axis, where the horizontal line denotes the plane of focus (b).

bright spot enclosed by the first zero crossings in Fig. 3.2 a, concentrates about 84% of the total photon flux and is known as the *Airy disc*, after G. B. Airy who first derived its mathematical description in 1835:

$$h(v,0) = h_0 \left[\frac{2J_1(v)}{v}\right]^2 . \tag{3.14}$$

The intensity along the optical axis is described by

$$h(0,u) = h_0 \left[\frac{\sin(u/4)}{u/4}\right]^2 . \tag{3.15}$$

In fluorescence microscopy, the three-dimensional intensity PSF has a descriptive significance as it gives the spatial absorption pattern of a uniform fluorophore solution in the vicinity of the focus.

3.1.3 Resolution

Resolution is one key feature in optical microscopy. It is generally defined as the minimum spacing between two point objects so that they can still be distinguished with a certain contrast in the image formed by the optical system. Two closely spaced pointlike objects may have overlapping images, each described by its intensity PSF. In general, two overlapping images consist of two peaks with a gap in between. Contrast is here defined as the difference between the lowest intensity in between the two objects and their maximum intensity. Spatial resolution can be quantified using the width of the intensity PSF.

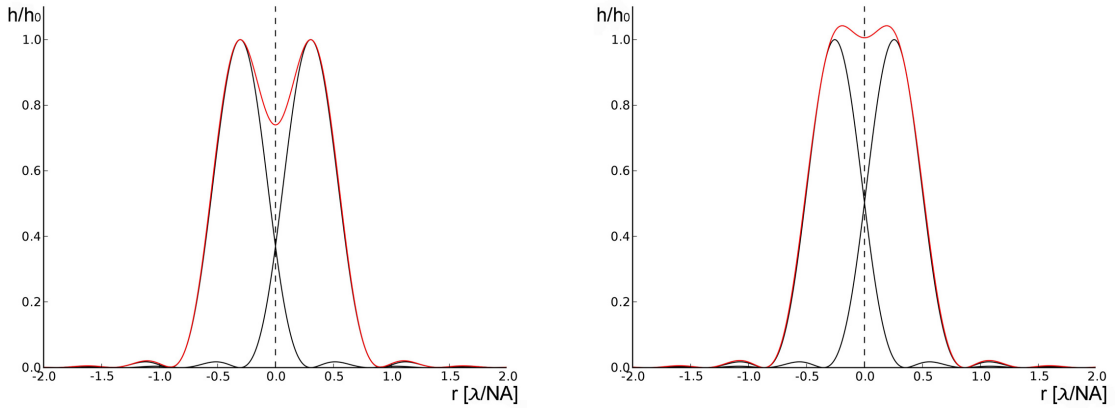

(a) (b)

Figure 3.3: Resolution limit: (a) Rayleigh criterion: Two images are separated if the first minimum of one coincides with the central maximum of the other. (b) Full width at half maximum (FWHM) criterion.

In the Rayleigh criterion, two equally bright spots are separately resolved when the first minimum of one Airy disc coincides with the principal maximum of the second Airy disc (Fig. 3.3 a). This corresponds to a separation at which a 26% contrast is achieved, i.e. the summed intensity in the gap between the two equally bright intensity PSFs is at 74% of the maximum intensity. This criterion relies on the assumption that the two point sources radiate incoherently (a condition that is fullfilled in fluorescence microscopy). If they emit coherently, their amplitude rather than their intensity in the image plane must be considered. Using the intensity PSF described above, the resolution limit can be expressed to be

$$\Delta r = 0.61 \frac{\lambda}{\mathrm{NA}}, \tag{3.16}$$

$$\Delta z = 2.0 \frac{n\lambda}{\mathrm{NA}^2} \tag{3.17}$$

in lateral and axial direction, respectively, where $\mathrm{NA} = n \sin(\alpha)$ is the numerical aperture of the focusing objective lens with n the refractive index of the object medium.

Another common measure for the resolution uses the full width at half maximum (FWHM) of the intensity PSF as the minimal spacing between two point objects to be

separately resolved (Fig. 3.3 b). Consequently

$$\Delta r = 0.51\frac{\lambda}{\mathrm{NA}}, \tag{3.18}$$

$$\Delta z = 1.77\frac{n\lambda}{\mathrm{NA}^2} \tag{3.19}$$

for the lateral and axial resolution, respectively.

It should be noted that the above considerations are established under the assumption of diffraction limited imaging. In practice however, resolution might be reduce by aberrations in the optical path. Lens aberrations can be grouped into either wavelength-independent (monochromatic) or chromatic aberrations. The major monochromatic aberration encountered in light microscopy is spherical aberration, which is due to the fact that peripheral rays of light do not intersect at the optimal focus of paraxial rays. Besides originating from the lens itself in which spherical aberration can be relatively well corrected by the lens' optical design, additional spherical aberration is induced if a refractive index mismatch between immersion medium and sample exists [Enger and Hell, 2006]. Also refractive index inhomogeneities within biological specimens, caused predominately by cellular structures and blood vessels, will affect the resolution and contrast of optical imaging [Helmchen and Denk, 2005; Pawley, 2006].
Chromatic aberrations result from the fact that the refractive index of optical glass varies with the wavelength of light (dispersion). This results in a wavelength dependent shift of the focal plane. In general, there is only one sharp focal plane for a given wavelength, for all others, the image plane is slightly defocused. Chromatic aberration can virtually be eliminated by the use of achromatic doublets, containing a positive and a negative lens element, each having a different dispersion to make the chromatic effect cancel out.

3.2 Fluorescence

Single-Photon Excited Fluorescence

Fluorescence is a luminescence that occurs upon absorption of light by a fluorophore. Absorption of light causes electrons to be excited to a higher electronic state where they remain for nanoseconds before returning to the ground state by the emission of a longer wavelength photon of lesser energy. This process is illustrated in the Figure 3.4, showing the major molecular pathways of a fluorophore in a Jablonski diagram. The lowest energy state, the ground state, is denoted by S_0. This state is for most organic molecules an electronic singlet, in which all electrons have opposite spin. For any molecule several excited states (S_1, S_2, ...) exist depending on the total electron energy. Each electron state is further subdivided into several vibrational and rotational states, each with distinct energy levels. At room temperature, most of the molecules exist in the lowest vibrational state of the ground state and hence, the excitation process

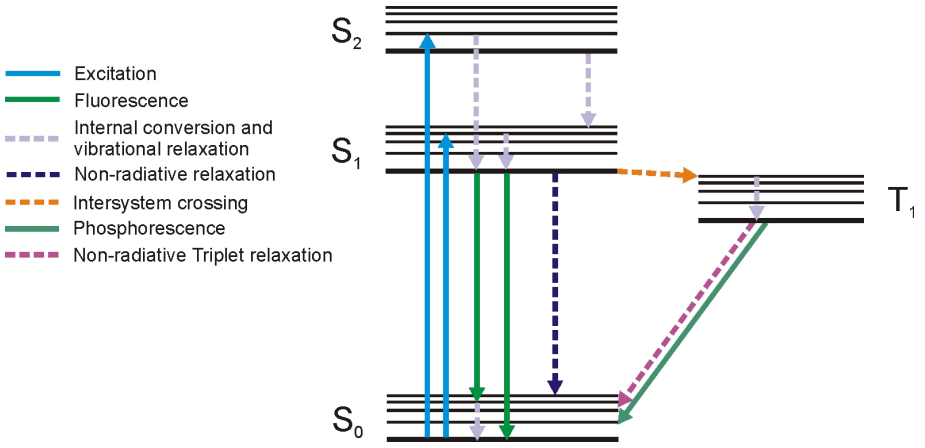

Figure 3.4: Jablonski diagram illustrating the major molecular pathways of a fluorophore upon absorption of a single photon. Straight lines mark radiative transitions, dashed lines non-radiative energy dissipation. Singlet states S_0, S_1, S_2; triplet state T_1.

usually originates from this energy level. A molecule is excited from its ground state to an excited state upon absorption of a photon of energy

$$E = h\nu = h\frac{c}{\lambda}, \tag{3.20}$$

where h is Planck's constant (6.626×10^{-34} Js), c is the speed of light in vacuum (3×10^8 m/s), ν is the frequency and λ the wavelength of the incoming photon. This process, which occurs due to an interaction of the oscillating electric field of the incoming photon with the electrons in the molecule, takes place in the order of 10^{-15} seconds and only if the energy of the photon is higher or equal the energy gap between the ground state and an excited state. The excess in energy is converted into vibrational or thermal energy resulting in a broad absorption spectrum that enables a range of photon energies with varying absorption probabilities to match a particular transition. Due to the conservation of spin momentum, the excited state is also a singlet. Upon absorption, higher energy levels mostly relax to the lowest vibrational energy state of S_1, by *internal conversion* or *vibrational relaxation* (both are non-radiative transitions), on a timescale of 10^{-12} seconds or less. An excited molecule persists in S_1 for about 10^{-9} seconds before finally relaxing under the emission of a photon to the ground state S_0. This process is called *fluorescence*. The different closely spaced vibrational states of the ground state, in which the molecule can relax, produce a wide range of emission photon energies and are the reason for a broad emission spectrum observed for most fluorophores. The probability for transitions in different vibrational energy levels of the excited state as well as the ground state is ruled by the fact that transitions associated with the absorption and emission of a photon are essentially instantaneous compared with the time scale of nuclear motions,

and therefore preferentially occur between energy levels whose vibrational wave functions overlap more significantly for a given internuclear distance (Franck-Condon principle). The rapid non-radiative energy loss due to internal conversion to the lowest vibrational energy level prior and after to fluorescence emission, causes the emitted photons to be less energetic (longer wavelength) than the photons responsible for excitation. This difference between the maximum wavelengths in excitation and emission spectra is termed *Stokes shift*, and is usually in the range of 20–100 nm, depending on the molecular structure of the fluorophore. It thus represents the mean energy loss while the molecule was in the excited state.
Other, less probable, relaxation pathways are the dissipation of the excited state energy as heat or transfer to another molecule by collision (non-radiative relaxation). Also *intersystem crossing* to the lowest excited triplet state T_1 is possible. This transition is favored when the triplet state vibrational energy levels overlap with the lower vibrational energy level in S_1. The transition to T_1 is followed by vibrational relaxation to the lowest energy state of T_1 and results in the emission of a photon through *phosphorescence* or a non-radiative conversion to the ground state. Quantum mechanical transitions from the triplet excited state to the singlet ground state are spin forbidden, which result in low probabilities for triplet emission with long lifetimes, ranging from microseconds to seconds.

The probability of the fluorescence emission relative to all other possible relaxation pathways for a given fluorophore, is measured by the *emission quantum yield* Q_e, which gives a measure for the maximum fluorescence intensity that can be obtained with a fluorophore. It is defined as the ratio of fluorescence photons emitted to the number of absorbed photons

$$Q_e = \frac{k_{fl}}{k_{fl} + k_{nr}}, \tag{3.21}$$

where k_{fl} is the fluorescence emission rate and k_{nr} is the decay rate of non-radiative transitions. For very good fluorophores, like fluorescein, the emission quantum yield is about 0.9, but is in most cases considerably lower [Hell, 2005].

The absorption rate of a fluorophore in interaction with an electromagnetic field can be calculated using the laws of quantum-mechanical time-dependent perturbation theory. The following formal analysis for a simple atom follows a description by R. W. Boyd [Boyd, 2003].
All properties of an atomic system can be described in terms of its atomic wavefunction $\psi(\mathbf{r}, t)$, which is a solution of the time-dependent Schrödinger equation

$$i\hbar \frac{\partial \psi}{\partial t} = H\psi, \tag{3.22}$$

where H is the Hamiltonian operator

$$H = H_0 + V(t) \tag{3.23}$$

expressed as the sum of the Hamiltonian H_0 of the free atom and an interaction Hamiltonian $V(t)$, which describes the interaction of the atom with the electric field. The interaction Hamiltonian is of the form

$$V(t) = -\mu E(t), \tag{3.24}$$

where $\mu = -er$ is the electric dipole operator, $-e$ is the charge of the electron, and $E(t)$ the applied electrical field strength written in the form

$$E(t) = E' e^{-i\omega t} + \text{c.c.} \tag{3.25}$$

for a monochromatic wave of angular frequency ω which is switched on suddenly at time $t = 0$ (c.c. means complex conjugate).
We assume that the solutions of the Schrödinger equation for a free atom with no external field applied are known, and that they can be represented as

$$\psi_n(\mathbf{r}, t) = u_n(\mathbf{r}) e^{-i\omega_n t} \quad \text{where} \quad \omega_n = E_n/\hbar. \tag{3.26}$$

Substituting this expression into the Schrödinger equation (3.22), we find that the spatially varying part of the wavefunction must satisfy the eigenvalue equation

$$H_0 u_n(\mathbf{r}) = E_n u_n(\mathbf{r}). \tag{3.27}$$

Since the energy eigenstates of H_0 form a complete set, the solution of Eq. (3.22) can be expressed as a linear combination of these eigenstates

$$\psi(\mathbf{r}, t) = \sum_l a_l(t) u_l(\mathbf{r}) e^{-i\omega_l t}. \tag{3.28}$$

Introducing Eq. (3.28) into Eq. (3.22) and making use of the orthogonality condition

$$\int u_m^*(r) u_l(r) d^3r = \delta_{ml} \tag{3.29}$$

we obtain

$$i\hbar \frac{da_m}{dt} = \sum_l a_l(t) V_{ml} e^{-i\omega_{lm} t}, \tag{3.30}$$

where $\omega_{lm} = \omega_l - \omega_m$ and

$$V_{ml} = \int u_m^*(\mathbf{r}) V u_l(\mathbf{r}) d^3r \tag{3.31}$$

are the matrix elements of the interaction Hamiltonian V.
For the general case in which an atom is exposed to an electromagnetic field, Eq. (3.30) can usually not be solved exactly, and perturbation theory is used. In order to solve Eq. (3.30) systematically in terms of a perturbation expansion, the Hamiltonian (3.23) is replaced by

$$H = H_0 + \lambda V(t), \tag{3.32}$$

where λ is a continuously varying parameter ranging from zero to one, characterizing the strength of the interaction; the value $\lambda = 1$ corresponds to the actual physical situation. Further expanding $a_m(t)$ in powers of the interaction as

$$a_m(t) = a_m^{(0)}(t) + \lambda a_m^{(1)}(t) + \lambda^2 a_m^{(2)}(t) + \ldots, \tag{3.33}$$

Eq. (3.30) yields

$$\frac{da_m^{(N)}}{dt} = \frac{1}{i\hbar} \sum_l a_l^{(N-1)}(t) V_{ml} e^{-i\omega_{lm}t}, \quad N = 1, 2, 3, \ldots \tag{3.34}$$

Single-photon (linear) absorption is described for $N = 1$ to correspond to an interaction first-order in the field. Assuming that in the absence of the applied excitation field, the atom is in the state g (typically the ground state) so that

$$a_g^{(0)}(t) = 1, \quad a_l^{(0)}(t) = 0 \quad \text{for} \quad l \neq g \tag{3.35}$$

Using Eqs. (3.24) and (3.25), V_{mg} is expressed as

$$V_{mg} = -\mu_{mg}(Ee^{-i\omega t} + E^* e^{i\omega t}). \tag{3.36}$$

Eq. (3.30) then becomes

$$\frac{da_m^{(1)}}{dt} = -\frac{\mu_{mg}}{i\hbar} \left[Ee^{-i(\omega_{mg}-\omega)t} + E^* e^{i(\omega_{mg}+\omega)t} \right]. \tag{3.37}$$

Integration of this equation gives

$$\begin{aligned} a_m^{(1)}(t) &= -\frac{\mu_{mg}}{i\hbar} \int_0^t dt' \left[Ee^{-i(\omega_{mg}-\omega)t'} + E^* e^{i(\omega_{mg}+\omega)t'} \right] \\ &= \frac{\mu_{mg}E}{\hbar(\omega_{mg}-\omega)} \left[e^{-i(\omega_{mg}-\omega)t} - 1 \right] + \frac{\mu_{mg}E^*}{\hbar(\omega_{mg}+\omega)} \left[e^{i(\omega_{mg}+\omega)t} - 1 \right]. \end{aligned} \tag{3.38}$$

The first term of this expression can become resonant for the process of one-photon absorption, and the second term can become resonant for the process of stimulated emission, i.e. if m lies below g. We can therefore drop the second term from our consideration

(rotating wave approximation).
Since $a_m^{(1)}(t)$ is the probability amplitude, the probability $p_m^{(1)}(t)$ that an atom is in state m at time t is given by

$$\begin{aligned} p_m^{(1)}(t) &= \left|a_m^{(1)}(t)\right|^2 = \frac{|\mu_{mg}E|^2}{\hbar^2}\left|\frac{e^{i(\omega_{mg}-\omega)t}-1}{\omega_{mg}-\omega}\right|^2 \\ &= \frac{|\mu_{mg}E|^2}{\hbar^2}\frac{4\sin^2[(\omega_{mg}-\omega)t/2]}{(\omega_{mg}-\omega)^2}. \end{aligned} \tag{3.39}$$

It can be shown that

$$\lim_{t\to\infty}\frac{4\sin^2[(\omega_{mg}-\omega)t/2]}{(\omega_{mg}-\omega)^2} = 2\pi t\delta(\omega_{mg}-\omega), \tag{3.40}$$

where $\delta(\omega_{mg}-\omega)$ is the Dirac delta function.
For large t, the probability to be in the upper state m is thus given as

$$p_m^{(1)}(t) = \frac{2\pi|\mu_{mg}E|^2 t}{\hbar^2}\delta(\omega_{mg}-\omega). \tag{3.41}$$

In physically realistic situation, the transition frequency is not perfectly well defined as given by expression (3.41), but the final state m is spread into a continuous density of final states $\rho_f(\omega_{mg})$, where $\rho_f(\omega_{mg})d\omega_{mg}$ gives the probability that the transition frequency lies between ω_{mg} and $\omega_{mg}+d\omega_{mg}$, normalized such that

$$\int_0^\infty \rho_f(\omega_{mg})d\omega_{mg} = 1. \tag{3.42}$$

For a transition characterized by a density of final states, the probability to be in the upper level given by Eq. (3.41) has to be averaged over all possible transition frequencies

$$\begin{aligned} p_m^{(1)}(t) &= \frac{2\pi|\mu_{mg}E|^2 t}{\hbar^2}\int_0^\infty \rho_f(\omega_{mg})\delta(\omega_{mg}-\omega)d\omega_{mg}. \\ &= \frac{2\pi|\mu_{mg}E|^2 t}{\hbar^2}\rho_f(\omega_{mg}=\omega). \end{aligned} \tag{3.43}$$

One can finally define a transition rate for single-photon absorption, which is given by the time derivative of Eq. (3.43)

$$k_{mg}^{(1)} = \frac{dp_m^{(1)}}{dt} = \frac{2\pi|\mu_{mg}E|^2}{\hbar^2}\rho_f(\omega_{mg}=\omega). \tag{3.44}$$

Using the intensity of the field, measured in photons/(cm^{2}s),

$$I = \frac{2n}{\hbar\omega}\left(\frac{\epsilon_0}{\mu_0}\right)^{1/2}|E|^2, \tag{3.45}$$

where n is the refractive index, $\epsilon_0 = 8.85 \times 10^{-12}$ F/m and $\mu_0 = 4\pi \times 10^{-7}$ H/m the permittivity and permeability of free space, respectively, one can write the absorption rate $k_{mg}^{(1)}$ as

$$k_{mg}^{(1)} = \sigma_{mg}^{(1)} I \tag{3.46}$$

with the *single-photon absorption cross section* $\sigma_{mg}^{(1)}$ defined such as

$$\sigma_{mg}^{(1)} = \frac{\pi\omega}{n} \left(\frac{\mu_0}{\epsilon_0} \right)^{1/2} \frac{|\mu_{mg}|^2}{\hbar} \rho(\omega_{mg} = \omega). \tag{3.47}$$

$\sigma_{mg}^{(1)}$ is typically in the order of 10^{-16} cm^2 [Xu et al., 1996].

Two-Photon Excited Fluorescence

In 1931 Maria Göppert-Mayer first theoretically predicted that the excited molecule state produced by the absorption of a single photon can alternatively be reached upon 'simultaneous' absorption of two lower energy, i.e. longer wavelength, photons in the same quantum event in a process called *two-photon excitation* [Göppert-Mayer, 1931]. The timescale for simultaneity is the timescale for molecular energy fluctuations at photon energy scales as determined by Heisenberg's uncertainty principle, namely 10^{-16} s. The energy sum of both photons being equivalent to the one required for single-photon excitation, such that

$$\lambda_{1P} \approx \left(\frac{1}{\lambda_A} + \frac{1}{\lambda_B} \right)^{-1}, \tag{3.48}$$

where λ_{1P} is the wavelength needed to promote a fluorescent molecule to the excited state in single-photon mode. The wavelengths of the two simultaneously absorbed photons do not have to be necessarily the same, but usually are for practical reasons (as they come from the same excitation light source)

$$\lambda_A = \lambda_B \approx 2\lambda_{1P}. \tag{3.49}$$

The fluorescence emission pathway is the same as described above for single-photon fluorescence. The fluorescence process upon simultaneous absorption of two photons is illustrated in Figure 3.5.

To calculate the two-photon absorption probability we use the second-order in the field in the perturbation theory described above. The probability amplitude $a_n^{(2)}(t)$ for the atom to be in level n at time t is thus given by Eq. (3.34) to be

$$\frac{da_n^{(2)}}{dt} = \frac{1}{i\hbar} \sum_m a_m^{(1)}(t) V_{nm} e^{-i\omega_{mn}t}, \tag{3.50}$$

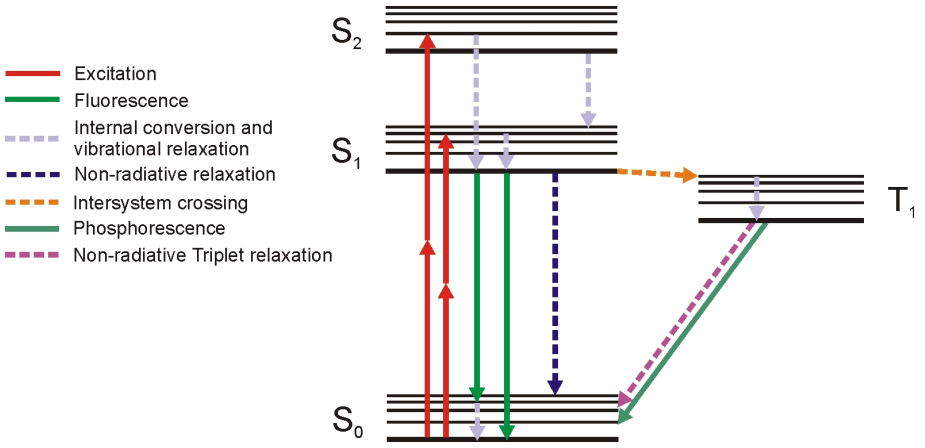

Figure 3.5: Jablonski diagram illustrating the major molecular pathways of a fluorophore upon simultaneous absorption of two photons.

with $a_m^{(1)}(t)$ given by Eq. (3.38). Using considerations analog as for single-photon absorption we obtain

$$\frac{da_n^{(2)}}{dt} = -\frac{1}{i\hbar}\sum_m \frac{\mu_{nm}\mu_{mg}E^2}{\hbar(\omega_{mg}-\omega)}\left[e^{i(\omega_{ng}-2\omega)t} - e^{i(\omega_{nm}-\omega)t}\right]. \tag{3.51}$$

The second term in square brackets can be dropped, as it does not lead to two-photon absorption. The obtained equation can be integrated to obtain

$$a_n^{(2)}(t) = \sum_m \frac{\mu_{nm}\mu_{mg}E^2}{\hbar^2(\omega_{mg}-\omega)}\left[\frac{e^{i(\omega_{ng}-2\omega)t}-1}{\omega_{ng}-2\omega}\right]. \tag{3.52}$$

The probability for the atom to be in level n is then again given by

$$p_n^{(2)}(t) = \left|a_n^{(2)}(t)\right|^2 = \left|\sum_m \frac{\mu_{nm}\mu_{mg}E^2}{\hbar^2(\omega_{mg}-\omega)}\right|^2 \left|\frac{e^{i(\omega_{ng}-2\omega)t}-1}{\omega_{ng}-2\omega}\right|^2. \tag{3.53}$$

For large t, the expression becomes

$$p_n^2(t) = \left|\sum_m \frac{\mu_{nm}\mu_{mg}E^2}{\hbar^2(\omega_{mg}-\omega)}\right|^2 2\pi t\delta(\omega_{ng}-2\omega) \tag{3.54}$$

and if we assume that the level n is smeared into a density of states, where $\rho_f(\omega_{ng})d\omega_{ng}$ is the probability that the transition frequency lies between ω_{ng} and $\omega_{ng}+d\omega_{ng}$, we obtain

$$p_n^2(t) = \left|\sum_m \frac{\mu_{nm}\mu_{mg}E^2}{\hbar^2(\omega_{mg}-\omega)}\right|^2 2\pi t\rho_f(\omega_{ng}=2\omega). \tag{3.55}$$

The transition rate for two-photon absorption can then be defined as

$$k_{ng}^{(2)} = \frac{dp_n^{(2)}(t)}{dt} = \left| \sum_m \frac{\mu_{nm}\mu_{mg}E^2}{\hbar^2(\omega_{mg} - \omega)} \right|^2 2\pi\rho_f(\omega_{ng} = 2\omega). \tag{3.56}$$

Using the intensity of the field, measured in photons/(cm^{2}s), the two-photon absorption transition rate is expressed as

$$k_{ng}^{(2)} = \sigma_{ng}^{(2)} I^2, \tag{3.57}$$

where $\sigma_{ng}^{(2)}$ is the *two-photon absorption cross section*

$$\sigma_{ng}^{(2)} = \frac{\pi\omega^2}{2n^2} \left| \sum_m \frac{\mu_{nm}\mu_{mg}}{\hbar(\omega_{mg} - \omega)} \right|^2 \rho f(\omega_{ng} = 2\omega) \tag{3.58}$$

which determines the efficiency of the two-photon absorption process for a given excitation intensity I. Two-photon excitation cross sections are typically in the order of 10^{-48} to 10^{-50} cm^{4}s/photon [Xu et al., 1996]. The important result of the above considerations is that the two-photon absorption transition rate is proportional to the square of the illumination intensity. This square dependency implies a number of practical advantages compared to single-photon excitation that are discussed below.

The quantum-mechanical selection rules for the two-photon process are different from those for the single-photon process and consequently, the two-photon peak absorption wavelength cannot be translated to be a priori twice the single-photon absorption peak. In fact, for isolated atoms a transition allowed for single-photon absorption is strictly forbidden for two-photon absorption and vice versa. For complex dye molecules however, due the effect of molecular vibrations and their reduced symmetry, strict parity selection rules do not hold anymore. It was found that the two-photon excitation spectra frequently appear blue shifted relative to twice the single-photon absorption peak [Xu et al., 1996]. The emission spectra are independent on the excitation process because the molecular relaxation process almost always occurs to the same state (lowest excited singlet state) prior to fluorescence emission and hence erases the memory of the excitation pathway.

As the lifetime of the excited sate S_1 is usually in the order of 1 ns which is 6 orders of magnitude larger than the oscillating period of the illumination light, the phase information of the incoming illumination light is destroyed upon absorption of a fluorescent molecule and thus fluorescence is an incoherent process.

3.3 Fluorescence in Microscopy

Fluorescence microscopy requires that the object of interest fluoresces upon excitation by illumination light. This can be achieved by labeling specific cellular or subcellular

compounds by specially synthesized exogenous fluorophores. In addition, organic substances often possess endogenous fluorophores inherent to the tissue (autofluorescence) that can be used as intrinsic monitor of the tissue's physiological state without the need for labeling. Fluorescence imaging only highlights the objects of interest in an otherwise black background and thus provides intrinsic selectivity and contrast.
Two revolutionary developments for non-invasive three-dimensional biological imaging are the *confocal laser scanning microscope* and the *two-photon excited fluorescence microscope*.

3.3.1 Confocal Laser Scanning Microscopy

Compared to a conventional microscope where an object is imaged by a magnifying lens simultaneously and parallel for all objects in one plane, a scanning microscope moves a focused spot of light over the specimen in a defined raster pattern while imaging only one object point at a time. The reflected or fluorescent light from the same volume is serially collected by a photodetector to synchronously build up a digital image from a series of point-by-point intensity measurements.

The main drawbacks of such a system, however, still are its limited resolution and finite depth of focus as unwanted contribution of signal from planes above and below the focal plane produce a strong background flare that degrades the image, and consequently restrict its application for three-dimensional imaging of depth structures. One way to overcome these limitation is achieved in *confocal scanning microscopy*.

The confocal principle was first described and patented by Minsky in 1961 [Minsky, 1961, 1988] as an attempt to reduce the amount of multiply scattered light from the sample under inspection in a conventional microscope. The decisive advantage of a confocal microscope is its confocal aperture, called *pinhole*, arranged conjugate to the object plane of the microscope with its center located on the optical axis. As a result the photodetector can only detect light that passes through the pinhole. This offers dramatic depth discriminating advantages over conventional microscopy, as out-of-focus signals are detected much less strongly than in-focus information.
Theoretical considerations of confocal image formation and technological advancements in illumination light sources and detection systems culminated in the development of confocal laser scanning microscopy to become an invaluable tool for biological research [Sheppard and Choudgury, 1977; Wilson and Sheppard, 1984; Cremer and Cremer, 1978; Brakenhoff et al., 1979; Wilke, 1985; White et al., 1987] and the most widely used optical sectioning technique for fluorescence imaging.

The basic optical layout of a confocal laser scanning microscope in epifluorescence mode[2] is diagramed in Figure 3.6. Laser light (usually from a UV or visible laser, as most fluorophores are excitable in this wavelength range), is focused by the objective

[2] the illumination and fluorescence light pass through the same objective lens

onto the sample in a diffraction limited spot. The excited fluorescence signal from the illuminated area, is spectrally separated from the excitation light by a dichroic mirror and focused as a confocal point onto the detector pinhole, positioned directly in front of the photodetector (usually a photomultiplier tube (PMT) or an avalanche photodiode (APD)) where the fluorescence intensity is converted from an analog signal into a pixel value by an analog-to-digital converter. By raster scanning the laser spot over the specimen, local and temporal intensity fluctuations are serially recorded from different parts in the sample to synchronously integrate them into a coherent digital image.
The pixel size should be chosen according to the *Nyquist sampling criterion*, i.e. there is a fixed relationship between the highest spatial (or temporal) frequency of interest in the data and the minimum sampling rate in order to record all the possible significant variations in the signal accurately. Specifically, for non-periodic data, the sampling frequency should be 2.3 times higher than the highest frequency in the data. This means that the Airy pattern image of a pointlike object should be 4–5 pixels across the diameter of the first dark ring. At smaller pixel sizes, the data will be oversampled, which results in an unnecessary higher radiation dose and more photobleaching. On the other hand, at larger pixel sizes, the recorded images are under-sampled and smaller features might be entirely missing or aliased. Therefore the pixel size is a fixed number defined by the optical resolution and the field of view.
To move the laser light across the sample, different scanner arrangements are possible. Besides tandem (Nipkow disc) scanning [Egger and Pétrăn, 1967] and stage-scanning, probably the most popular way to raster scan the sample in confocal fluorescence microscopy is the beam scanning (or flying spot) method that uses two (typically galvanometer driven) mirrors to change the angle the beam passes through the back-focal-plane of the objective. If the rotational axis of the mirrors coincide with the optical axis, a pair of scanning mirrors moves the laser beam across the focal plane in x-y-direction.
The straight lines in Fig. 3.6 show the optical path for an object that lies in the focal plane. Light emanating from a plane above or below the focal plane (dashed lines), arrives at the detector pinhole as a defocused blur, only the central region of which is detected and contributes to the image. In this way the system discriminates against features that do not lay in the focal region of the objective. The larger the defocus distance, the weaker the detected signal. This property is the major reason for the popularity of confocal microscopes as it allows to image detail from one specific volume by the choice of the focal position in thick translucent samples (*optical sectioning*) and reconstruct its three-dimensional structure by a stack of sections at different depth without necessarily mechanically slicing the object. Acquisition and visualization is generally computer-controlled by appropriate software.

The intensity PSF of a confocal microscope can be described as the probability for a fluorescence photon to be emitted in a point (v, u), expressed by the illumination PSF $h_{ill}(v, u)$, times its probability to pass through the confocal pinhole and be detected, expressed by the detection PSF $h_{det}(v/\beta, u/\beta)$. The factor $\beta = \lambda_{fl}/\lambda_{ill}$ is the ratio of

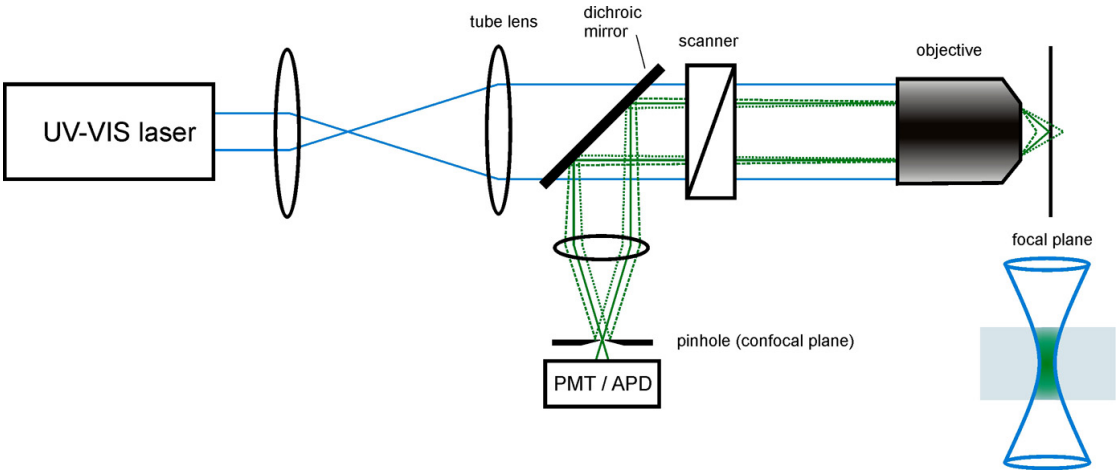

Figure 3.6: Basic setup of a fluorescence confocal laser scanning microscope. Fluorescence excited upon single-photon absorption from an UV or visible laser occurs over the whole illuminating cone in the specimen. The excitation path is marked in *blue*, the fluorescence emission path in *green*.

the illumination to the fluorescence wavelength. Typically one approximates β by 1, and obtains for the effective PSF of a confocal microscope

$$h_{confocal}(v,u) = h_{ill}(v,u) \cdot h_{det}\left(\frac{v}{\beta}, \frac{u}{\beta}\right) \approx h_{ill}^2(v,u). \tag{3.59}$$

The simulated intensity PSF of a confocal microscope along the lateral and axial direction is shown in Figure 3.7. The quadratic dependence of the PSF has the two major consequences to make the width of the PSF smaller, resulting in a resolution improvement by a factor of 1.4 compared to conventional microscopy [Brakenhoff et al., 1979], and to reject fluorescence from molecules that are not in focus.
Assuming an uniform illumination of the objective lens, the FWHM resolution of an ideal confocal microscope depends on both the excitation and emission wavelength, and can be expressed as [Zeiss, 2003]:

$$\Delta r = 0.37\frac{\overline{\lambda}}{\mathrm{NA}}, \tag{3.60}$$

$$\Delta z = 1.28\frac{n\overline{\lambda}}{\mathrm{NA}^2} \tag{3.61}$$

in lateral and axial direction, respectively, where $\overline{\lambda}$ is the mean wavelength defined as

$$\overline{\lambda} = \sqrt{2}\frac{\lambda_{ill}\lambda_{fl}}{\sqrt{\lambda_{ill}^2 + \lambda_{fl}^2}}. \tag{3.62}$$

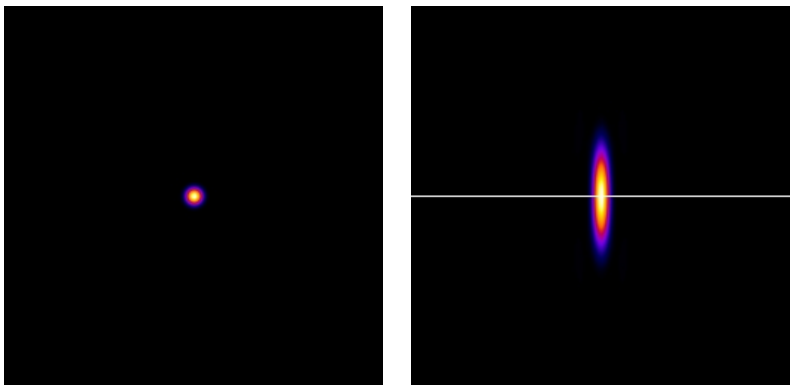

(a) lateral (b) axial

Figure 3.7: Simulated sections through the intensity PSF of a confocal microscope along the lateral (a) and axial (b) plane. The horizontal line denotes the plane of focus. The resolution improvement compared to Fig. 3.2 is obvious.

The above considerations are based on the concept of an ideal point illumination and point detection. In practice, the pinholes are of finite size and the confocal PSF has to be convolved with the respective illumination and detection pinhole functions. A laser running in TEM_{00} can be regarded as an ideal point source smaller than the Airy pattern and therefore be neglected. The detection pinhole however sets a practical limit to the effectively achieved confocal resolution and is always a trade-off between resolution and signal strength. A pinhole considerably smaller than the Airy pattern does only marginally improve resolution and blocks most of the light intensity, whereas a larger pinhole primarily degrades depth resolution. A good compromise is achieved for a pinhole size of 1–2 Airy units[3] [Pawley, 2006].

One of the main problems of confocal microscopy is its wasteful use of excitation light, since absorption occurs throughout the whole illumination cone in the specimen, but useful information is only gathered from a thin slice around the focal plane [Denk and Svoboda, 1997].

One elegant way to circumvent this problem became recently available with the introduction of *two-photon excited fluorescence microscopy*.

3.3.2 Two-photon Excited Fluorescence Microscopy

30 years after Maria Göppert-Mayer's theoretical prediction of two-photon excitation, Kaiser and Garrett [Kaiser and Garrett, 1961] were, thanks to the invention of the first laser sources, the first to experimentally demonstrate two-photon excited fluorescence

[3] One Airy unit is defined as the diameter of the Airy disc, i.e. 1 Airy $= 1.22\lambda_{fl}/\mathrm{NA}$.

emission in a CaF_2:Eu^{2+} crystal in 1961. In 1990 Denk et al. were the first to apply this technology to scanning laser microscopy and introduced its way to biological applications [Denk et al., 1990]. From there on, two-photon excited fluorescence (TPEF) microscopy has developed to a powerful new optical microscopy technique for three-dimensional fluorescence imaging of biological specimens, and experienced a tremendous success in biological research and live sciences to become the technique of choice in non-invasive fluorescence microscopy for thick tissues and live animals with still unexplored potential [Zipfel et al., 2003b].

The huge impact of TPEF microscopy is mainly derived from its unique property of localized excitation which leads to qualitatively and quantitatively new imaging characteristics. As the emission of two-photon fluorescence is quadratically dependent on the excitation intensity, two-photon absorption is only confined to the vicinity of the focal plane where the light intensity is highest [Denk et al., 1990], in contrast to single-photon fluorescence where absorption occurs through the entire illumination cone even while only imaging a single plane. This spatial localization is at the basis of a number of major advantages for bioimaging applications. It results in an intrinsic three-dimensional diffraction limited resolution providing optical sectioning in thick tissues without the need of a confocal pinhole to spatially filter the emission light as no out-of-focus background fluorescence is produced. This allows the implementation of wide-field detectors in combination with a non-descanned optical emission path with the advantage of higher collection efficiency in scattering tissues, as all fluorescence photons, even those scattered, are known to originate from the focal plane and constitute useful signal [Denk, 2006].
The penetration depth of the illumination light in thick biological samples is also greatly improved, up to one millimeter [Theer et al., 2003], by the use of near infrared (NIR) light, due to less scattering and absorption outside the focal plane [Centonze and White, 1998; Gerritsen and De Grauw, 1999]. In the easiest case, scattering in biological tissue produced by particles that are small compared to the wavelength of light can be described by Rayleigh-scattering and is proportional to the inverse fourth power of the wavelength of light being scattered ($\propto \lambda^{-4}$). For particles of size comparable to λ, the scattering process is described by Mie-scattering and the wavelength dependency is slightly less ($\propto \lambda^{-3}$). Consequently longer wavelength illumination light provides a larger sensing depth. All the more, scattered light removes energy from the incident beam and thereby attenuates the intensity of the transmitted excitation light in the focal plane.
Because two photons are absorbed for each transition event, the use of red or NIR excitation light to excite fluorophores that normally absorb in the UV or visible light in single-photon fluorescence microscopy, allows access to a range of fluorescent indicators that would otherwise require UV lasers for single-photon excitation in combination with specialized UV optics.
In TPEF microscopy, photobleaching and photodamage may only occur in the focal plane where photointeraction takes place, and consequently, tissue viability is increased. Due to the lack of efficient single-photon endogenous cellular absorbers in the spectral range

from about 700 nm to 1100 nm, NIR TPEF microscopy is considered less phototoxic [König, 2000] compared to single-photon fluorescence microscopy, and living organisms can be imaged over extended periods without compromising viability [Squirrell et al., 1999].

The basic setup of a TPEF microscope is shown in Figure 3.8. Just as in confocal laser scanning microscopy, the focused excitation laser beam is raster scanned across the specimen. Beam scanning and data acquisition are essentially identical than in confocal laser scanning microscopy described above. However, due to the nonlinear character of the excitation, the fluorescence is only emitted from a thin focal plane and spatially resolved detection is not necessary. A confocal pinhole before the detector is therefore obsolete. An appropriate dichroic mirror is used to spectrally separate excitation and emission light. The large spectral separation gap between excitation and fluorescence emission, allows an efficient signal collection and greatly simplifies multiple fluorophore detection in the same sample. The absence of a confocal pinhole makes several epifluorescence detection schemes possible: In (1), the fluorescence signal is descanned and projected to a point detector that can be a photomultiplier tube (PMT) or an avalanche photodiode (APD) which have higher quantum efficiencies than conventional PMTs and are favorable at low fluorescence levels [Tan et al., 1999]. This setup still allows the implementation of an optional detector pinhole, which was shown to provide an additional resolution improvement, albeit at the expense of signal strength [Gauderon et al., 1999] which is rarely desirable in TPEF microsocopy where emission photons are usually scarce. Besides from simplifying the optical path, a superior fluorescence collection for deep tissue imaging is achieved by non-descanned detection (2) where the emitted radiation is collected without passing through the scanning mirrors using a large-area PMT. Consequently ballistic as well as scattered photons that are collected by the objective, reach the detector and contribute to the total acquired signal.

As two-photon absorption cross sections are usually very low, high illumination intensities in the $MWcm^{-2}$ to $GWcm^{-2}$ are necessary to increase the probability that two photons simultaneously interact with a molecule. The maximum fluorescence output is obtained by high spatial and temporal concentration of the excitation intensity. This is best achieved by tightly focusing a pulsed laser with high peak intensity and moderate time-averaged intensity (still tolerated by the target tissue). With a pulsed laser, the two-photon excited fluorescence emission depends on the average squared intensity $< I(t)^2 >$ rather than on the squared average intensity $< I(t) >^2$ [Zipfel et al., 2003b]. The average intensity is equal to the number of pulses per second f, times the instantaneous intensity during a pulse, which gives

$$< I(t)^2 >= \xi < I(t) >^2 \qquad \text{with} \qquad \xi = \frac{g}{\tau f}, \tag{3.63}$$

where g is a unitless factor that depends on the temporal laser pulse shape (0.66 for a Gaussian pulse), τ is the full width at half maximum (FWHM) of the pulse, and <>

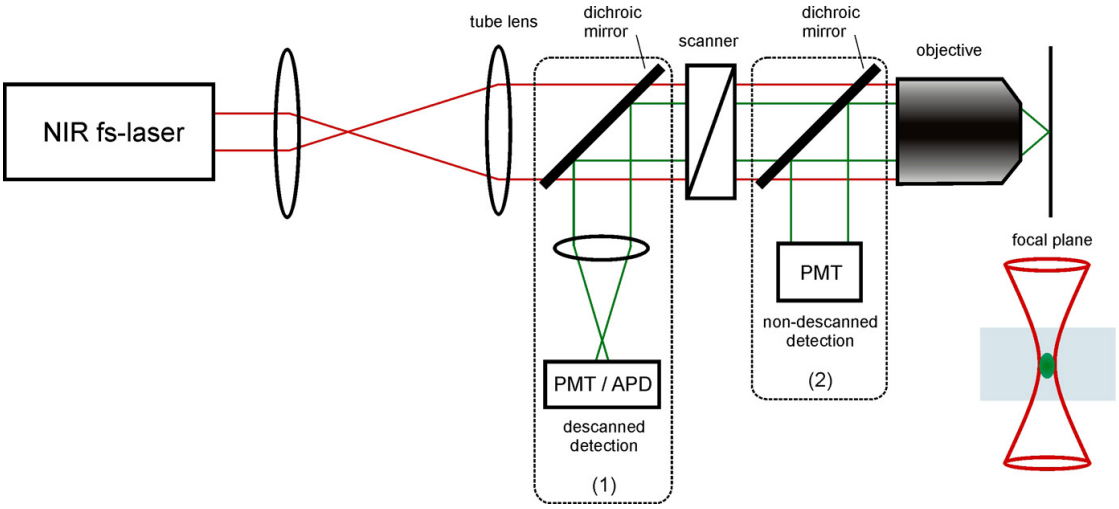

Figure 3.8: Basic setup of a two-photon excited fluorescence microscope with descanned (1) and non-descanned (2) detection. The fluorescence emission is intrinsically localized to the vicinity of the focal spot. The excitation path is marked in *red*, the fluorescence emission path in *green*.

denotes the time-averaged value. Thus the two-photon excitation probability is enhanced by the factor of ξ compared to a continuous wave (CW) illumination. Practically, only mode-locked laser with pulse durations below 1 ps and repetition rates in the range of 100 MHz with a 'two-photon advantage' of about 10^5 made TPEF microscopy feasible [Denk, 2006].
Due to dispersive optical glass components in the microscope's excitation path, pulses are spread in time, which leads to a chirped pulse that is longer than the original one but still contains the same optical frequency spectrum. For a given amount of dispersion, shorter pulses, which have a broader spectrum, are spread more than longer pulses. This limits the pulselength range that can be used for efficient TPEF microscopy (if not using optical elements of negative dispersion for pulse compression) to the order of 150–250 fs. For a Gaussian pulse, pulse broadening B can be estimated using the following expression

$$B = \frac{\tau_{out}}{\tau_{in}} = \sqrt{1 + (4 \ln 2)^2 \left(\frac{D}{\tau_{in}^2} \right)^2}, \tag{3.64}$$

where D is the total dispersion in fs^2. In a typical microscope with $D = 5000\ \text{fs}^2$, an incoming chirp-free 180 fs pulse is broadened to 195 fs, whereas in comparison a 10 fs pulse translates to about 1.5 ps.
Another restricting factor to pulsewidth is that photobleaching and photodamage show a highly nonlinear nature, which would favor longer pulsewidth [Hopt and Neher, 2001;

König, 2000]. This is however still subject to ongoing research and no universal quantitative conclusions have been found yet.

The probability p that a fluorophore at the center of the focus simultaneously absorbs a photon pair during a pulse, is finally dependent on the average illumination power P_{av}, the pulsewidth τ, the repetition rate f, the wavelength λ, and the numerical aperture NA of the focusing optics as [Denk et al., 1990]

$$p \approx \frac{\sigma P_{av}^2}{\tau f^2} \left(\frac{\mathrm{NA}^2}{2\hbar c \lambda} \right)^2 , \tag{3.65}$$

where σ is the two-photon absorption cross section, c the speed of light, $\hbar$ the Planck quantum of action, saturation is neglected and the paraxial approximation is assumed.

In two-photon microscopy, the effective PSF is the square of the illumination PSF

$$h_{2P}(v,u) = h_{ill}^2 \left(\frac{v}{2}, \frac{u}{2} \right) \tag{3.66}$$

assuming $\lambda_{ill}/2 \approx \lambda_{fl}$, and $v/2$ and $u/2$ indicating an about doubled illumination wavelength compared to single-photon excitation. At first sight the theoretical PSF of TPEF microscopy seems larger than in single-photon confocal microscopy in both lateral and axial directions, due to the longer illumination wavelength. However, the achievable practical resolutions are similar because finite-sized pinholes used in practical confocal microscopy broaden the theoretical PSF [Cox and Sheppard, 2004].
Assuming a uniform illumination of the objective lens to achieve a diffraction limited focus, the resolution of the two-photon microscope can be expressed as FWHM of a Gaussian fit to the squared illumination point spread function. Fitting the lateral and axial intensity squared profiles yields [Zipfel et al., 2003b]

$$\Delta r = \begin{cases} \frac{0.320\sqrt{2\ln 2}\lambda}{\mathrm{NA}} & , \quad \mathrm{NA} \leq 0.7 \\ \frac{0.325\sqrt{2\ln 2}\lambda}{\mathrm{NA}^{0.91}} & , \quad \mathrm{NA} \geq 0.7 \end{cases} \tag{3.67}$$

$$\Delta z = 0.532\sqrt{2\ln 2}\lambda \left(\frac{1}{n - \sqrt{n^2 - \mathrm{NA}^2}} \right) , \tag{3.68}$$

where λ is the excitation wavelength, NA the numerical aperture of the focusing objective lens, and n the refractive index of the immersion medium.

4 Toward Two-Photon Excited Fluorescence Ophthalmoscopy: A New Approach In Retinal Imaging

Fluorescence microscopy has recently found a niche in ophthalmology for non-invasive monitoring of retinal disease. Mainly lipofuscin in the retinal pigment epithelial cells is strongly autofluorescent upon blue light excitation. Its fluorescent properties permit a direct visualization of retinal health which has become a useful diagnostic tool for age-related macular degeneration.
The following chapter explains the design and realization of a two-photon excited fluorescence microscope based on the fast scanning unit of a conventional laser scanning ophthalmoscope for a potential implementation of nonlinear microscopy to ophthalmology for imaging the human retina.

4.1 Imaging of Endogenous Fluorophores and Fundus Autofluorescence

In most fluorescence applications, autofluorescence from endogenous fluorophores within the tissue is undesirable, as it acts as a source of background that reduces detector sensitivity. However, under certain conditions, imaging of native biological fluorophores may provide crucial quantitative information on cell activity that requires neither labeling nor slicing. It provides a mean for direct visualization of tissue morphology, cell metabolism and disease [Zipfel et al., 2003a], especially for in vivo functional imaging of cells in their natural environment.
The primary tissue autofluorophores are mainly derived from aromatic amino acids such as Tryptophan (Trp), Tyrosine (Tyr), Phenylalanine (Phe), with absorption and emission bands in the UV, and from blue to yellow emitting vitamin derivatives such as retinol, oxidized flavin proteins (FP) (flavin adenine dinucleotide, FAD, and flavin mononucleotide, FMN), reduced pyridine nucleotides (both reduced nicotinamide-adenine dinucleotide, NADH, and reduced nicotinamide-adenine dinucleotide phosphate, NADPH, denoted following as NAD(P)H). Their fluorescent properties provide direct feedback on tissue's physiological and pathological state. The major site of localization of flavins and NAD(P)H is the mitochondria. Their fluorescence has been extensively used to monitor the cellular energy metabolism using both single- and two-photon excited fluorescence

[Masters, 1984a,b; Kunz et al., 1994; Kuznetsov et al., 1998; Shiino et al., 1999; Piston et al., 1995]. Because only the oxidized FPs and reduced NAD(P)H are significantly fluorescent, their relative signal oppositely reflects changes in mitochondrial metabolic state [Huang et al., 2002].

In the human retina a number of intrinsic fluorescent molecules enable direct non-invasive functional visualization of tissue morphology and disease. In ophthalmology, the strong intrinsic fluorescence of lipofuscin within the RPE cells has predominately been recognized for clinical diagnostic. In vivo recordings of the ocular fundus have identified RPE lipofuscin to primarily express strong natural autofluorescence when excited with blue light [Delori et al., 1990; von Rückmann et al., 1995; Delori et al., 1995a]. The fluorescence is derived from a number of intrinsic fluorophores, counting at least ten [Eldred and Katz, 1988], present in the lipofuscin granules that accumulate with age and degenerative diseases, suggesting that metabolic functioning of the RPE correlates with the amount of lipofuscin present in RPE cells. Fundus autofluorescence measurements thus allow a direct visualization of the pathological and functional state of the retina by highlighting defects in the RPE that remain unrevealed with traditional procedures of fundus photography or simple ophthalmoscopy [von Rückmann et al., 1997]. By means of autofluorescence, possible configurations and developments of atrophic states in age-related macular degeneration (AMD) or other degenerative diseases can be identified and classified for diagnostic and prognostic reasons with tremendous potential [Framme et al., 2005; Bindewald et al., 2005b].

Besides the RPE, other fluorophores anterior and posterior to the RPE cell layer show autofluorescent properties which are a direct indicator of aging and disease [Han et al., 2007]. Although their excited signal intensity is far below that derived from lipofuscin, they potentially open new imaging ways to quantitatively measure retinal health.

4.2 State-of-the-Art in Fundus Autofluorescence Imaging

With the development of the first ophthalmoscope in 1851 by Hermann von Helmholtz [von Helmholtz, 1851], live imaging of the ocular fundus has developed from simple photographically recorded images to more complex and specific digital recording laser scanning devices providing quantitative and reproducible information on retinal health over time [Lois et al., 1999].

Fundus autofluorescence (FAF) imaging was first clinically demonstrated in 1995 by von Rückmann [von Rückmann et al., 1995]. It is a recent useful diagnostic tool for quantitative, non-invasive in vivo monitoring of RPE related retinal degenerative pathologies [Lois et al., 2000] and more specifically AMD [von Rückmann et al., 1997], which became available with the introduction of the *confocal scanning laser ophthalmoscope (cSLO)* in the 90s [Webb et al., 1987].

Nowadays the clinically most common used and the only one to provide high quality

autofluorescence images of the ocular fundus [Framme et al., 2005; Bellmann et al., 2003] is the *Heidelberg Retina Angiograph (HRA)* (Heidelberg Engineering GmbH[1]), originally designed for performing fluorescein angiography. The HRA is a confocal scanning laser ophthalmoscope in nature. Figure 4.1 shows a simplified schematic of the cSLO used in FAF imaging. A blue laser beam (Argon or DPSS laser) at 488 nm wavelength is

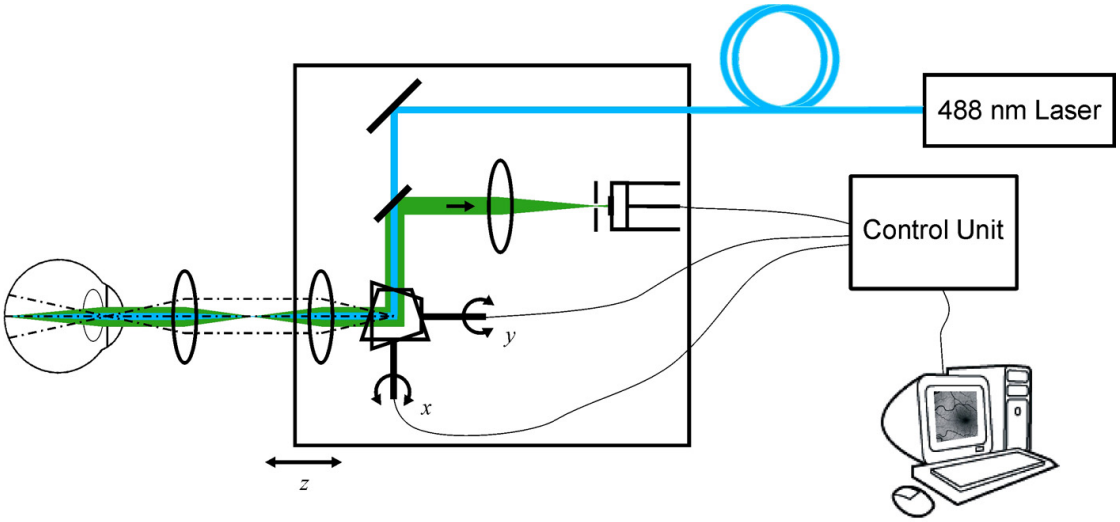

Figure 4.1: Simplified schematic of a confocal laser scanning ophthalmoscope (cSLO) used for fundus fluorescence imaging in the living eye. The excitation light path is marked in *blue*, the fluorescence emission path in *green*.

focused by the patient's eye internal optics (cornea and lens) onto the retina via two orthogonal scanning mirrors that deviate the beam in x- and y-direction to trace out a raster. The successive small retinal regions containing fluorescent proteins are excited by the laser light, so that at any instant, the fluorescence intensity is proportional to the local concentration of fluorophores. The fluorescence signal (> 500 nm) passes back out through the full eye's pupil, is descanned, and focused onto a confocal pinhole. The position of the confocal pinhole is by definition conjugate to the focal plane of the illumination system to suppress out-of-focus light. A dichroic mirror separates the fluorescence light from the excitation light. The light passing through the pinhole is recorded by a photodetector and is thus a direct measure of the local fluorescence (index of RPE lipofuscin content) in the focal plane. The HRA implements a high-sensitivity silicon avalanche photodiode (APD) to keep the light level at the retina low. The field of view can be varied by altering the scan angle by $30° \times 30°$, $15° \times 15°$, $10° \times 10°$ corresponding to a retinal field of view of approximately 9 mm $\times$ 9 mm, 4.5 mm $\times$ 4.5 mm,

[1]Heidelberg, Germany; `http://www.heidelberg-engineering.com`

3 mm × 3 mm, respectively. The optic block together with the scan lens is movable along the optical axis and thus allows to vary the focal depth (z-scan) and to compensate for an eventual refractive error of the patient's eye optics (up to +/- 12 diopters).

Autofluorescence images are usually evaluated for the presence of areas or abnormal intensity. An example of a cSLO FAF image, showing the topographic distribution of the lipofuscin content throughout the fundus of a healthy retina, is given in Figure 4.2 a. The picture is characterized by an uniform fluorescence distribution with lacking signal at the optic nerve head (absence of RPE cells) as well as at the retinal blood vessels (blockade) and gradual decrease in the macula toward the fovea due to the presence of blue light absorbing neuroretinal luteal pigment. There is also a slight decrease in fluorescence intensity toward the periphery, in agreement with histological findings that lipofuscin concentration is proportional to the photoreceptor density which declines toward the periphery as well [Delori et al., 2001].
In contrast, Figure 4.2 b shows a FAF image of an AMD patient with geographic atrophy in the macular region corresponding to an area of signal absence due to a complete loss of RPE cells. The atrophic area is bordered by a ring of elevated fluorescence resulting from an abnormal increase of lipofuscin in the corresponding RPE cells. Findings that the number of photoreceptors is reduced in the presence of high contents of lipofuscin in the RPE cells, leads to the conclusion that areas of increased autofluorescence may precede RPE cell loss and the development of the geographical atrophy [Dorey et al., 1989; Holz et al., 2001]. Focal reticular alterations of the fluorescence signal outside the atrophic area are probably associated with the presence of small drusen [Bindewald et al., 2005a,b; Delori et al., 2000].

FAF evaluation has not only become invaluable in the diagnosis and monitoring of RPE-related degenerative diseases, but also assists in the identification and classification of different pathological phenotypes, which are particularly important in the search of possible genetic factors of influence on the disease. It further also helps to assess cell viability after RPE transplantation or pharmacological treatments that target RPE cells. As fluorescence recordings are directly correlated to the pathological state of the RPE cells, FAF possibly provides crucial hints in the understanding of the underlying mechanisms that trigger these degenerative RPE-related retinal diseases, and to identify areas of high risk for vision loss.
All these applications demand high-resolution imaging devices providing best achievable image quality to reveal the potential source responsible for the onset of the disease rather than monitoring its secondary effects. In this dissertation a novel technique for non-invasive high-resolution functional imaging of RPE cells is envisaged by the use of two-photon excited fluorescence.

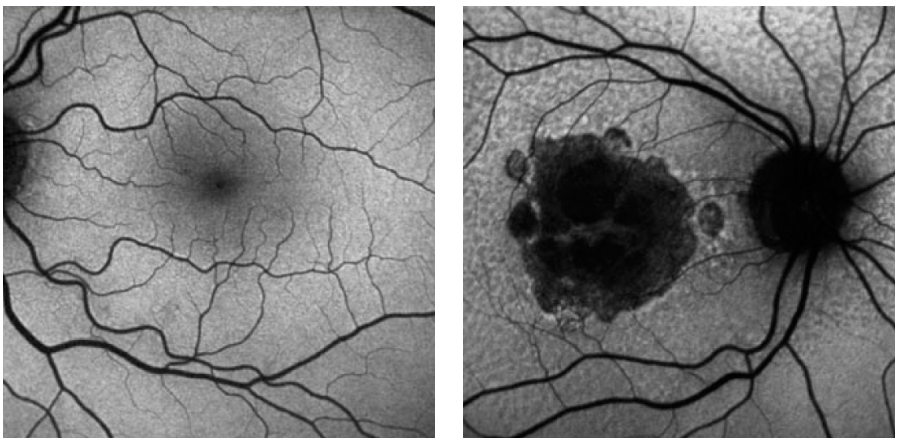

(a) (b)

Figure 4.2: cSLO fundus autofluorescence of a healthy patient (a); and an AMD patient with central geographic atrophy of the RPE (b). Image source: [Bindewald et al., 2005b].

4.3 Setup and Characterization of the Nonlinear Ophthalmoscope-based Microscope

Regarding the tremendous success of scanning laser ophthalmoscopy, combined with the advantages of two-photon excited fluorescence (section 3.3.2) and the transparency of the human eye to NIR light, we believe that nonlinear retinal imaging has undiscovered potential for non-invasive high-resolution diagnostic methods in ophthalmology that cannot be appreciated with single-photon imaging.

Today, TPEF imaging is particularly widely used in neurology and embryology [Denk et al., 1994; Mainen et al., 1999; Squirrell et al., 1999] for vital imaging, but applications in ophthalmology are still in their very early developments [Imanishi et al., 2004; Han et al., 2006; Bindewald-Wittich et al., 2006; Han et al., 2007; Piston et al., 1995]. Typical TPEF systems require one second or more for a full-frame scan, but many biological processes in cells and tissues undergo much faster changes [Fan et al., 1999]. Especially in any clinical ophthalmological applications, where the presence of motion artifacts like eye movements is a concern, high-speed scanning systems are necessary. To the best of our knowledge, there has been no work reported on the application and potential of TPEF through a fast scanning ophthalmoscope toward real-time in vivo imaging of the human eye.

The present study focuses on the design and development of a novel custom-made two-photon laser scanning ophthalmoscope for the study of the feasibility of a high-speed resonant scanning TPEF system for a potential in vivo clinical application.

4.3.1 The Optical Setup

The scanning and detection unit of a conventional confocal scanning laser ophthalmoscope (Heidelberg Retina Tomograph® (HRT), Heidelberg Engineering GmbH) with a modified epi-illumination light path, was coupled to a mode-locked Titanium-Sapphire ($Ti{:}Al_2O_3$ or Ti:Sa) femtosecond (fs) laser (Mira 900, Coherent Inc.[2]), pumped by a 532 nm DPSS CW laser (Verdi V5, Coherent Inc.) of 5.5 W output power. A schematic illustration of the final setup is shown in Figure 4.4.
The Ti:Sa laser employed has a pulse repetition rate of 76 MHz and a wavelength tunable from 700 to 980 nm with one set of optics. The maximum average output power of the horizontally polarized beam is about 500 mW and can be linearly attenuated by rotating a neutral density filter wheel (ND) (0.04–3.00 OD, Edmund Optics[3]) in the excitation beam to change the laser power transmitted as a function of the optical density range. Figure 4.3 shows the measured emission spectrum of the Ti:Sa laser before entering the optical setup. The central wavelength is set at $\lambda_0 = 831$ nm. By fitting a Gaussian profile to the measured values, the spectral FWHM is $\Delta\lambda = 5.58 \pm 0.02$ nm. Under the assumption of a transform-limited chirp-free Gaussian pulse, the pulsewidth respectively the temporal FWHM width τ_{FWHM} of the Ti:Sa laser can be calculated from the time-bandwidth product $\tau_{\mathrm{FWHM}}\Delta\nu = 0.441$, using $\Delta\nu = (c\Delta\lambda)/\lambda^2$ [Saleh and Teich, 1991] to be

$$\tau_{\mathrm{FWHM}} = 0.441 \cdot \frac{\lambda_0^2}{c \cdot \Delta\lambda} \approx 182 \pm 0.7 \text{ fs}, \tag{4.1}$$

where c is the speed of light ($c = 300$ nm/fs).

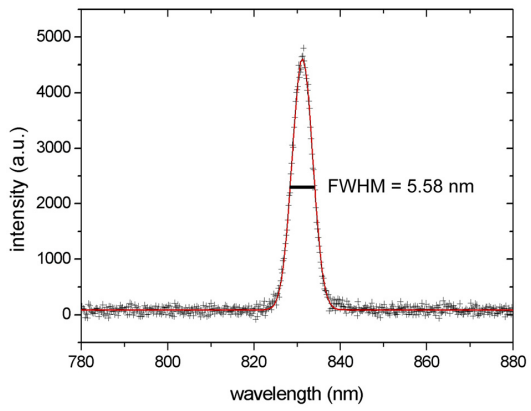

Figure 4.3: Emission spectrum of the mode-locked Ti:Sapphire laser.

After passing a long-pass dichroic mirror (DiM) (Semrock[4]), designed to transmit the laser light (T > 90 %: 750–1100 nm) and reflect the fluorescence light (R > 98 %: 350–

[2]Santa Clara CA, USA; `http://www.coherent.com`
[3]Karlsruhe, Germany; `http://www.edmundoptics.com`
[4]Rochester NY, USA; `http://www.semrock.com`

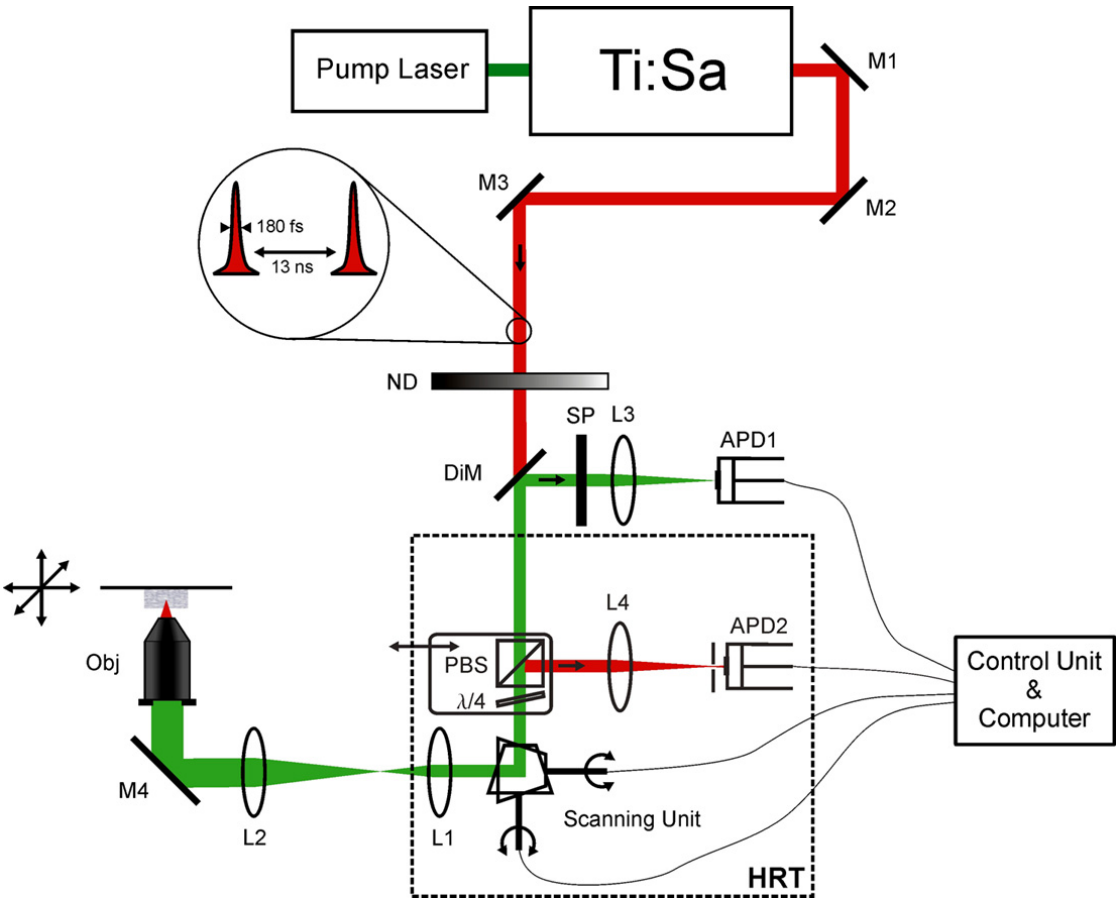

Figure 4.4: Diagram of the optical setup for fast TPEF imaging, based on a conventional scanning laser ophthalmoscope (HRT). The excitation light path is marked in *red* and the fluorescence emission path in *green*.

720 nm), (Fig. 4.5 a), the laser beam is raster scanned by a high-speed resonant 4 kHz scanning mirror in x-direction[5] and a linear galvanometer scanner for the slow scanning in y-direction. The ideal arrangement would place the two mirrors in telecentric planes. Alternatively, as described in our setup, the mirrors can be located in close proximity to one another with the telecentric plane in their middle (*close-coupled*-configuration). The scanning unit uses silver-coated mirrors and allows frame rates up to 20.83 Hz[6]. The original scan angle range of $30° \times 30°$, $15° \times 15°$, $10° \times 10°$ was electronically modified for

[5] It is also possible to acquire an image during the forward and backward scan, which results in an effective horizontal frequency of 8 kHz.

[6] including a 16 ms dead time between two consecutive frames used for retrace of the scanner

high-resolution optical 'zooming' to 16° × 16°, 8° × 8°, 1.6° × 1.6°. In order to overfill the back-aperture of the objective (Obj) (U-V-I Apochromat, 40×/0.8 W, working distance 3.3 mm, Leica[7]) for a diffraction-limited focus on the specimen, the entering beam is expanded by the scan (L1) (focal length $f_1 = 30$ mm[8]) and the tube lens (L2) (achromat $f_2 = 100$ mm) by a factor (f_2/f_1) of 3.3 to about 10 mm ($1/e^2$ width). The laser beam is deflected by 90° for a horizontal mount of the specimen to allow the use of the water immersion objective. A manual *xyz* translation stage is utilized for lateral and axial positioning of the sample under the excitation beam. Mirrors M2, M3 allow a proper alignment of the excitation beam relative to the scanning unit. With the three scan angle settings described above, the field-of-view is 420 µm × 420 µm, 210 µm × 210 µm and 42 µm × 42 µm, respectively.

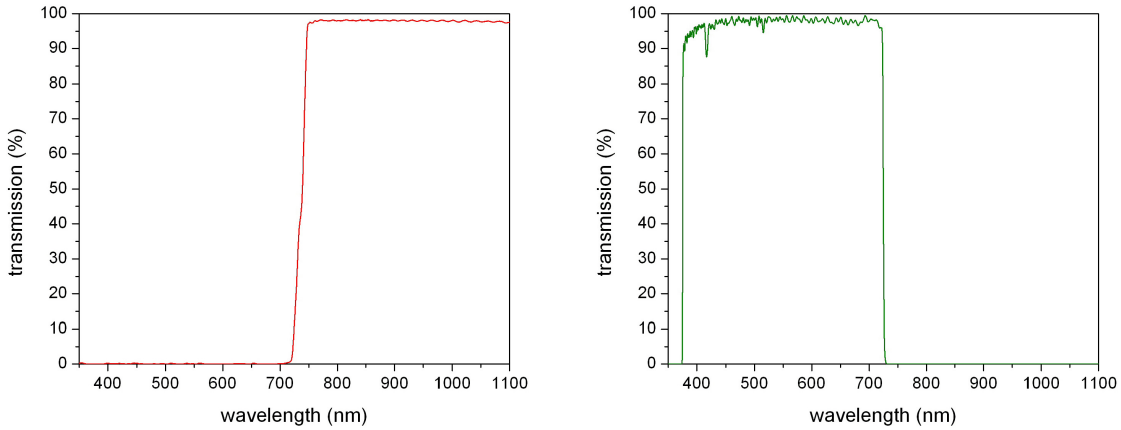

(a) (b)

Figure 4.5: Measured transmission spectra of the dichroic mirror (DiM, Semrock, FF735-Di01-25 × 36) at 45° reflection as average of *s*- and *p*-polarized light (a); and the short-pass filter (SP, Semrock, FF01-750/SP-25) at normal incidence (b). Both are so-called hard-coating interference filters providing high light transmission and a sharp edge between their reflection and transmission bands.

The fluorescence from the excited molecules in focus is collected by the same objective lens, descanned, and the collimated light beam is reflected by the dichroic mirror and focused by L3 (achromat, $f_3 = 60$ mm) onto a pre-amplified silicon avalanche photodiode (APD1) (C30950E, EG&G Optoelectronics, Canada) with an active area size of 0.8 mm in diameter. Backscattered laser light is further rejected by a short-pass barrier filter

[7] Wetzlar, Germany; `http://www.leica-microsystems.com`

[8] In order to reduce lens aberrations, two achromatic lenses of $f_{a/b} = 60$ mm separated by $d = 0.4$ mm are used, resulting in a total focal length of $f_1 = \left(\frac{1}{f_a} + \frac{1}{f_b} - \frac{d}{f_a f_b}\right)^{-1} \approx 30$ mm.

(750 nm cut-off wavelength, OD $>$ 6, Semrock), (Fig. 4.5 b). For optimal performance, the interference filter is placed in the collimated beam in between the dichroic mirror and the focusing lens. The excitation is point-by-point of a square raster scanned region of interest centered around the optical axis. Since no two-photon excited fluorescence is generated outside the focal volume, a confocal pinhole is left out. The time integration of the 50 MHz-bandwidth APD is synchronized to the scanner by a pixel clock in order to temporally and spatially reconstruct a digital two-dimensional 8-bit gray scale[9] image of 256×256 pixels as the laser sweeps across the sample with a pixel dwell time of 0.50 µs. The sensitivity of the APD is $\sim 2.3 \times 10^5$ V/W at 550 nm detection wavelength. The live image is displayed on a personal computer using Windows NT® and the standard HRT-software package *Heidelberg Eye Explorer*®. A stack of 32 successive images is recorded and subsequently averaged so that each pixel of the final image is obtained from measurements of the same pixel at different times. Effectively, noise[10] decreases with the square root of the number of combined frames. Temporally averaging over 32 images thus increases the signal-to-noise ratio (SNR) by a factor of $\sqrt{32} = 5.7$ compared to a single frame capture.
The setup also allows to exchange the APD with a spectrometer (USB4000-VIS-NIR, Ocean Optics[11]) of a spectral bandwidth from 350 to 1000 nm and optical resolution of about 1.3 nm (FWHM), to measure the fluorescence emission spectrum of the specimen region in focus.

Besides the fluorescence detection unit described above, the setup also provides the original confocal reflection mode of the HRT by simply inserting a polarizing beam-splitter (PBS) followed by a quarter-wave-plate ($\lambda/4$), mounted on a custom-made holder, into the beam pass. The horizontally polarized excitation laser light passes the PBS and is circularly polarized after the quarter-wave plate placed at 45° with respect to the incoming linear polarization. Upon reflection at the sample, the polarization state of the backscattered light is turned by 180°. Passing the quarter-wave-plate a second time provokes vertically polarized light that is reflected by the PBS and focused by another achromatic lens (L4), of $f_4 = 60$ mm focal length, to a second silicon avalanche photodiode (APD2) to generate backscattered light contrast. For better depth discrimination, a confocal pinhole of $\phi_{ph} = 75$ µm diameter is located in front of the photodiode, conjugate to the in-focus plane. An electronic switch permits to change between both detection modes while still being synchronized to the scanning unit.

For comparison measurements, the setup can as well be changed from two-photon detection mode to single-photon detection (Figure 4.6) with a 488 nm DPSS blue excitation laser (Kyma, Melles Griot GmbH[12]) of 20 mW maximal output power. The power of the

[9] containing $2^8 = 256$ different gray levels to display pixel intensities
[10] In fluorescence microscopy the limiting noise source is mainly Poisson noise.
[11] Dunedin FL, USA; `http://www.oceanoptics.com`
[12] Bensheim, Germany; `http://www.mellesgriot.com`

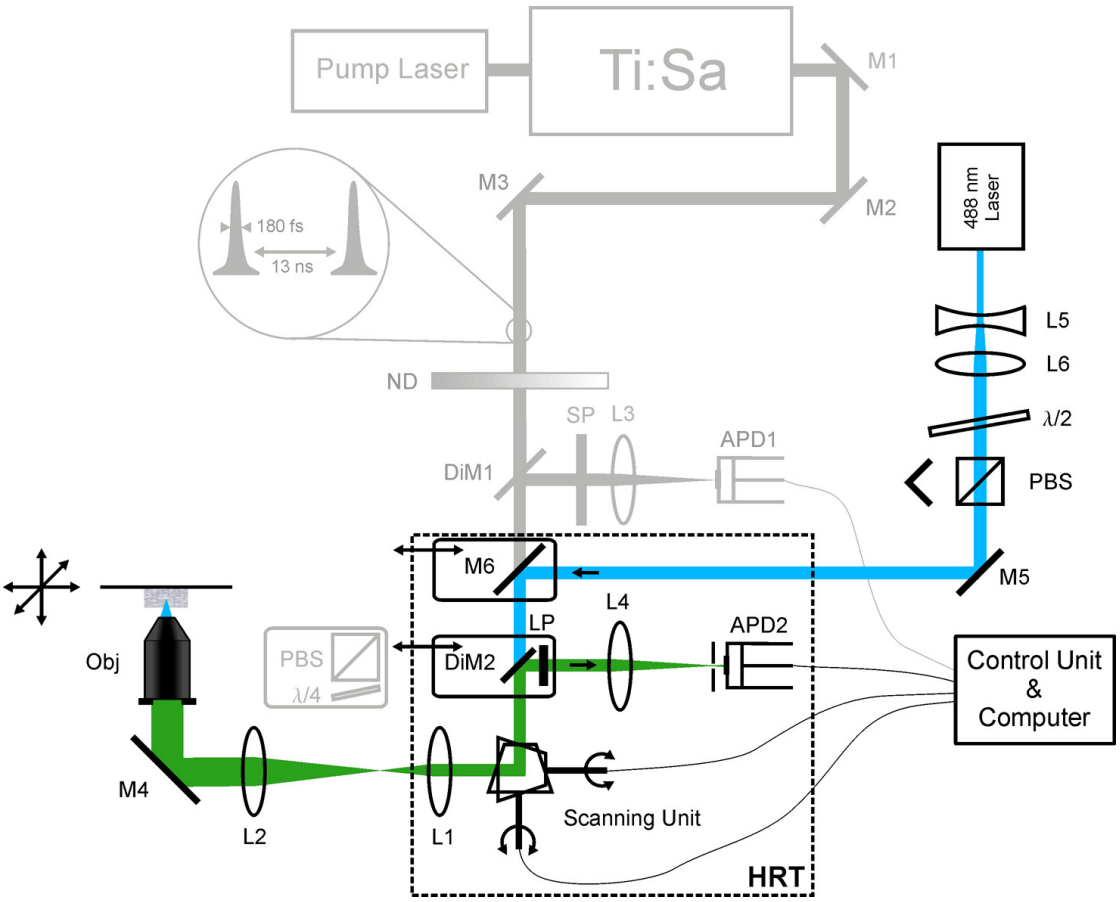

Figure 4.6: Diagram of the modified nonlinear imaging setup for single-photon fluorescence imaging with a blue illumination laser source at 488 nm. The excitation path is marked in *blue*, the fluorescence emssion path in *green*.

vertically polarized laser light at the sample is continuously controlled by a combination of half-wave-plate (λ/2) and polarized beam-splitter (PBS). Turning the half-wave-plate affects the amount of *p*-polarized laser light transmitted through the PBS acting as a polarizer. The laser beam is expanded by a Galilean telescope, consisting of L5 (focal length $f_5 = -10$ mm) and L6 (focal length $f_6 = 50$ mm), by a factor of 5 to 3.5 mm. Mirrors M5, M6 are used for proper alignment of the excitation beam relative to the scanning unit.
The single-photon excited fluorescence light is reflected by a short-pass dichroic mirror (DiM2) (adopted from the original 'Heidelberg Retina Angiograph (HRA)', Heidelberg Engineering GmbH), designed to transmit the laser light and reflect the longer fluorescence light. An additional long-pass filter with 500 nm cut-off wavelength further

separates the fluorescence light from residual backscattered light. The fluorescence intensity is recorded in the same confocal detection channel (APD2) as described above for the reflection imaging mode. Mirrors M6 and DiM2 are mounted on removable holders to quickly switch between single-photon and two-photon excited fluorescence imaging for the same sample in focus. A photograph of the setup for combined two- and single photon imaging is given in Figure 4.7.

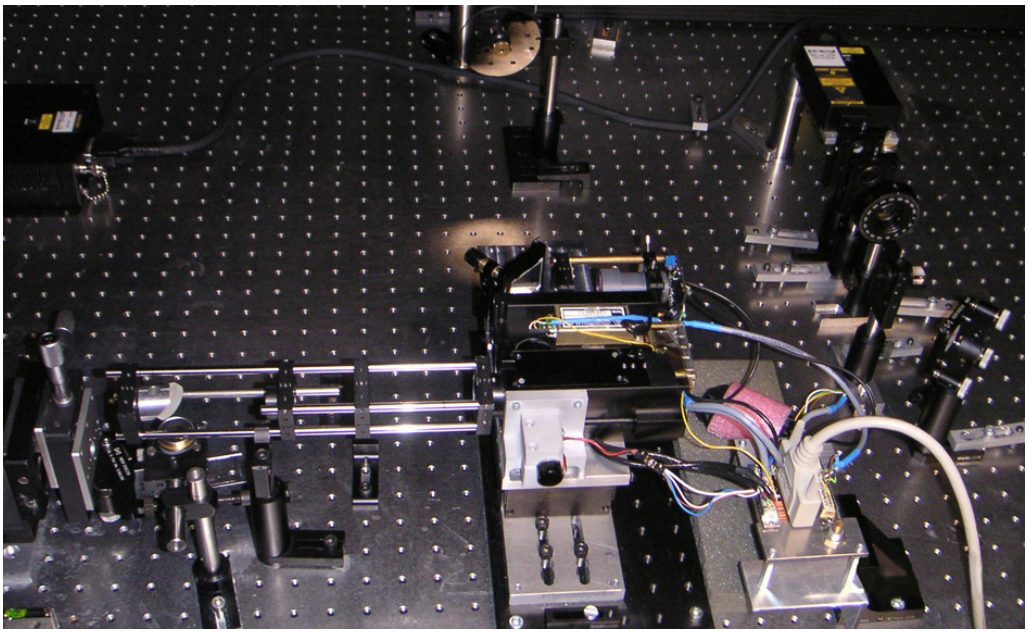

Figure 4.7: Photograph of the optical setup for combined two- and single-photon imaging.

The scanning unit, scan lens, tube lens and objective lens form together a telecentric system, i.e. two lenses are spaced the sum of their focal length apart. The entrance and exit pupils are both at infinity in object and image space, respectively. Consequently, rotation of the mirror moves the focused spot across the focal plane in a straight line (Figure 4.8). This is necessary as the microscope objective lens is telecentrically corrected to avoid converging lines effects[13] and has the advantage that the system is space invariant and linear, and all its properties are determined by the magnification factor of the objective lens M (see Table 4.1).

[13] When imaging the real eye, this effect is compensated by the curved surface of the eyeball and telecentricity is not required.

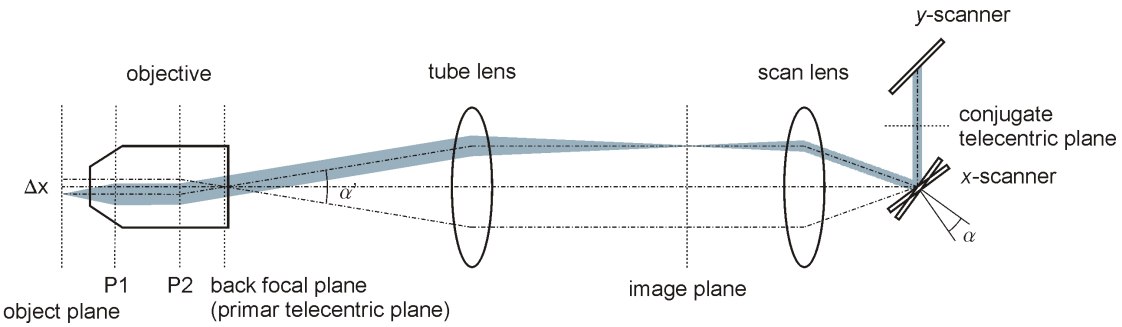

Figure 4.8: View of the flattened excitation path. P1, P2 are the principle planes of the objective, α is the tilt angle of the x-scanner, α' the scan angle along the x-axis in the telecentric plane, and Δx is the field of view.

Table 4.1: Properties of the optical setup.

Description	Symbol/formula	Value
focal length of scan lens	f_1	30 mm
focal length of tube lens	f_2	100 mm
focal length of objective lens	f_{Obj}	5 mm
effective magnification of objective lens	$M = f_2/f_{\mathrm{Obj}}$	20×[a]
numerical aperture of objective lens	NA	0.8
numerical aperture of scan and tube lens	$\mathrm{NA}' = \mathrm{NA}/M$	0.04
tilt angle of x-scanner	α	16°, 8°, 1.6°
tilt angle along x-axis in telecentric plane	$\alpha' = \alpha(f_1/f_2)$	4.8°, 2.4°, 0.48°
field of view in object plane	$\Delta x = 2f_{\mathrm{Obj}} \tan(\alpha'/2)$	420, 210, 42 µm
image size in primary image plane	$\Delta x' = M\Delta x$	8.40, 4.20, 0.84 mm
sampling frequency	$\Delta x/256$	1.64, 0.82, 0.16 µm/pixel

[a]The objective lens used has a nominal magnification of 40× referenced on a tube lens of $f_2 = 200$ mm.

4.3.2 Characterization of the Prototype

Initial Tests

For a first impression of the TPEF imaging efficiency of the setup, we used an artificial sample consisting of a drop of a diluted fluorescent dye (Alexa Fluor 514, Invitrogen-Molecular Probes[14]) dried on a piece of paper, which was fixed on a conventional sample holder that could be easily mounted under the objective. Alexa Fluor 514 shows a strong fluorescence over a broad excitation spectrum with a single-photon absorption maximum at 518 nm and an emission maximum around 540 nm. Figure 4.9 gives an example of these images, recorded at different locations within the sample for two-photon and one-

[14]Carlsbad CA, USA; `http://www.invitrogen.com`

photon excited fluorescence for two different scan angle settings. The single fluorescing paper fibers can clearly be distinguished in both imaging modi. To demonstrate that the

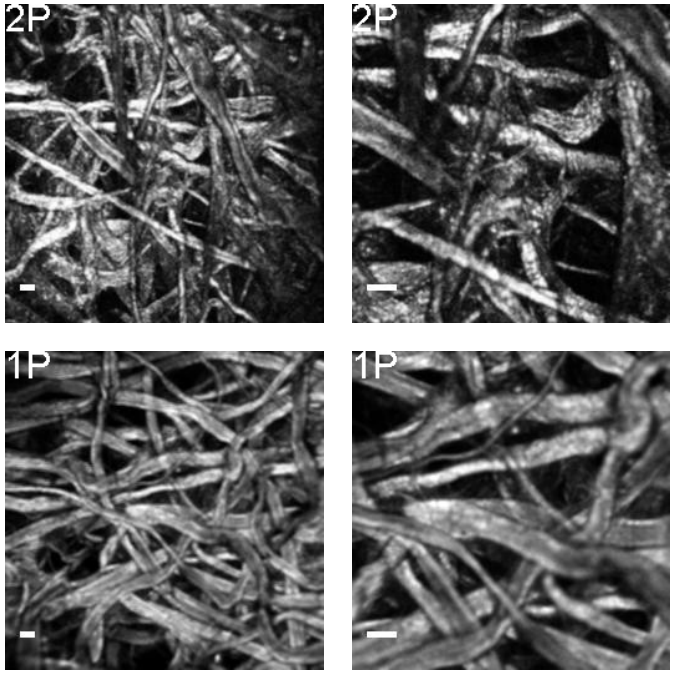

Figure 4.9: Two-photon (2P) and single-photon (1P) excited fluorescence of Alexa Fluor 514 for different scan angles. Scale bar, 20 µm.

detected signals do truly originate from a fluorescence process, the emission spectrum was measured in the two-photon and single-photon excited fluorescence mode by replacing the respective photodiode with the spectrometer. The results are plotted in Figure 4.10, and clearly indicate a fluorescence emission spectrum ranging from 500–700 nm, peaking around 540 nm.

Resolution

After this first verification, the lateral resolution of the described two-photon and single-photon imaging setup was experimentally quantified using fluorescent beads of 0.2 µm (TetraSpeck™ Fluorescent Microsphere Standards, Invitrogen-Molecular Probes). The beads are stained throughout with four different dyes, each with different excitation/emission characteristics: 365/430 nm (blue), 505/515 nm (green), 560/580 nm (orange), and 660/680 nm (red). Only the green dye was used in this study. As the PSF is the response of an optical system to a point source, it is important to use small beads compared to the diffraction limit. For larger particles, the results would be greatly determined by the

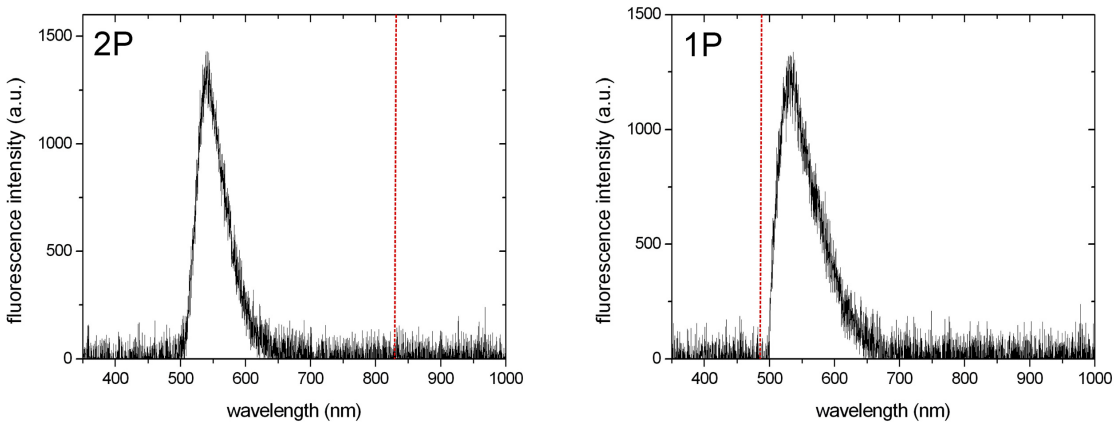

Figure 4.10: Two-photon (2P) and single-photon (1P) excited fluorescence emission spectra of Alexa Fluor 514. The excitation wavelength at $\lambda_{ex,2P} = 831$ nm and $\lambda_{ex,1P} = 488$ nm, respectively, is marked as a dashed vertical line.

bead shape and hence not by the PSF.
For the test, a drop of diluted beads suspended in aqueous low melting point agarose (1% in H_2O) was put on a custom-made sample holder and air-dried. Unfortunately, as the micrometer screws of our translation stage for positioning of the sample under the excitation beam only have a resolution of 10 µm, the axial resolution could not be determined experimentally. The focal plane was manually estimated by selecting the plane of the brightest signal. The mean lateral resolution was calculated as the FWHM of a Gaussian fit to different intensity profile plots along the optical center of four fluorescent beads in x-y-direction, as illustrated in Figure 4.11. The measured mean FWHM values ($\pm$ standard deviation) are 450 ± 77 nm and 380 ± 14, for two-photon and single-photon excitation, respectively.

The theoretical values for the lateral FWHM resolution in two-photon excited fluorescence can be calculated from Eq. (3.67) to be about 390 nm. In the single-photon fluorescence mode, the resolution depends on the size of the confocal pinhole. The confocal pinhole employed in our setup corresponds to 2.2 Airy units[15] for the given objective and intermediate optical system. For pinhole sizes greater than 1 Airy unit (geometric-optical confocality), the lateral resolution is essentially equivalent to conventional fluorescence microscopy [Cox and Sheppard, 2004] (except that the resolution is determined by the excitation wavelength) and can therefore be estimated using Eq. (3.18) to be 311 nm.

The experimentally estimated lateral PSFs are in both imaging modes larger than the theoretical predicted ones. Regarding the sampling frequency of 0.16 µm/pixel, Nyquist

[15] 1 Airy unit is defined as the diameter of the image of the first dark Airy ring in the pinhole plane, i.e. $1.22\frac{\lambda}{\mathrm{NA}}\frac{f_4}{f_1}M$, where λ is the fluorescence wavelength.

criterion is approximately met in our setup (slightly under-sampled in single-photon fluorescence mode). However, over-sampling would be more appropriate for practical imaging at the resolution limit, as smaller pixel size results in a smoother and more accurate representation of the PSF. Stelzer calculated a minimum of eight pixels per Airy disc to guarantee an accurate representation of the real image. Because pixelation tends to make maxima smaller and minima larger, the detected resolution is inherently reduced in digitalizing systems [Stelzer, 1998], even more when the signal-to-noise ratio is limited. The large standard variation probably results from the imprecision of choosing the correct focal plane. A piezo-driven z-scan would have given better results. Nevertheless do the experimentally determined PSFs give an estimate of what resolution to expect in real imaging conditions.

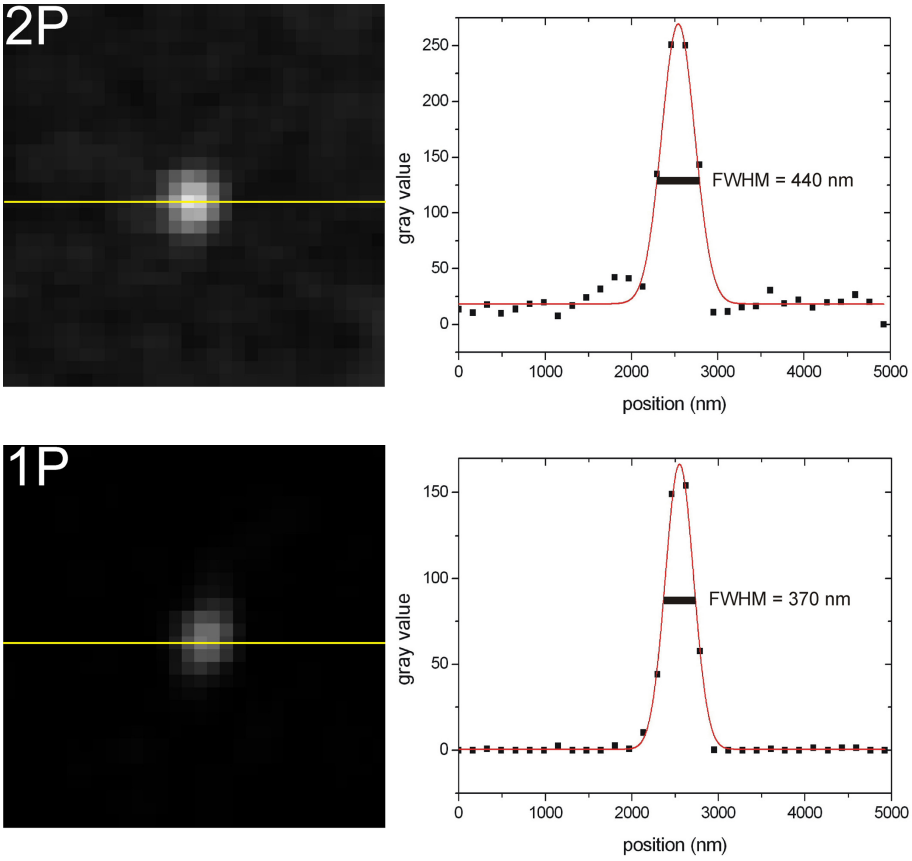

Figure 4.11: Representative fluorescence images of a 0.2 µm fluorescent bead and corresponding profile plot along the optical center in x-direction in a Gaussian fit; two-photon (2P) excitation at $\lambda_{ex,2P} = 831$ nm; and single-photon (1P) excitation at $\lambda_{ex}, 2P = 488$ nm. Emission wavelength $\lambda_{fl} = 515$ nm, image size 5 µm × 5 µm.

5 Measurements on Retina Specimens

This chapter describes and discusses representative measurements on retina specimens from human donor eyes in order to study the feasibility and potential of the fast scanning ophthalmoscope-based microscope for nonlinear retinal imaging. The autofluorescence properties of the RPE as well as the neural retina are investigated. Two-photon excited fluorescence measurements on RPE cells are further compared to conventional confocal single-photon excitation imaging. Finally a compact Nd:glass fs-laser system is tested toward its feasibility for two-photon fluorescence imaging of retinal endogenous fluorophores.
Unless otherwise specified, all images presented have not been processed in any way, except contrast enhanced for better visibility.

5.1 Sample Preparation

The retina samples were obtained from Caucasian postmortem donor eyes provided by the eye bank of the Department of Ophthalmology, University of Bonn. All donors had normal vision with no macroscopic visible retinal alterations such as soft drusen, retinal hemorrhage, or choroidal neurovascularization. The donor age varied between 54 and 62 years. Informed consent for corneal transplantation and further use of tissue for research purposes was obtained from a relative or documented in an organ donor pass according to the German law for organ donation.

After enucleation and cornea removal, the posterior half of the eyeball was cut and immediately fixed with paraformaldehyde solution (4% in phosphate buffered saline (PBS), pH 7.4). A 5 mm diameter full-thickness retina, choroid, sclera probe in the region of interest was cut with a surgical trephine. In most cases the neural retina separated from the RPE-choroid-sclera complex without manual assistance. The relative tissue probe was immersed in a custom-made specimen holder filled with PBS solution (pH 7.4) and positioned for imaging under the water immersion objective lens. After imaging, the specimens were stored at 4°C in the dark.

5.2 Imaging RPE Cells

5.2.1 TPEF Imaging of RPE Cells

As retinal autofluorescence is mainly derived from endogenous fluorophores present in the lipofuscin granules of the RPE cells, our first aim was to image the RPE cell layer by TPEF to verify the potential of nonlinear microscopy for fundus autofluorescence imaging.

Figure 5.1 shows the RPE cell layer from the macular region of a 54-year-old donor eye imaged by exciting their natural lipofuscin fluorophores, for the three available magnification settings. For the two lower zoom settings, the image is under-sampled which might sometimes be beneficial when high frequency image details are not required and fluorescence photons are scarce or radiation dose has to be minimized. In Fig. 5.1 c, Nyquist criterion is met and the single intrinsic fluorescent lipofuscin granules can easily be detected and localized. They appear as lateral round spots, distributed along the cytoplasm between the cell nucleus (no autofluorescence signal) and the cell wall.

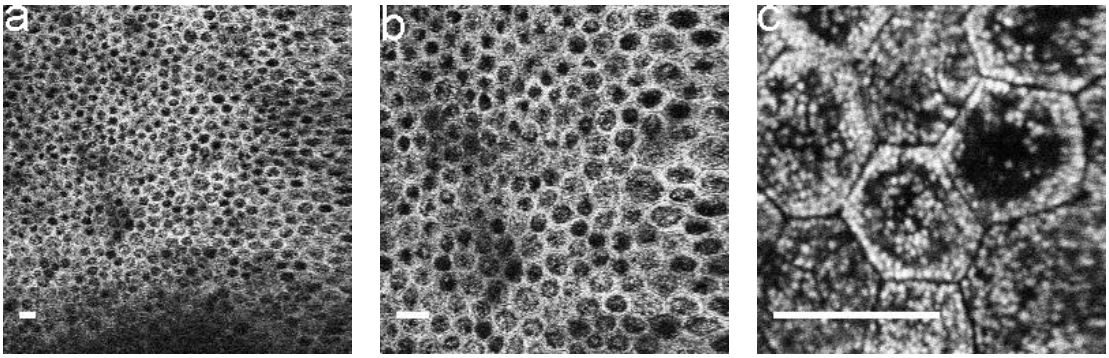

Figure 5.1: Two-photon excited autofluorescence images of RPE cells from a 54-year-old donor eye in the macular area for three different zoom settings. Each is an averaged stack of 32 images. Scale bar, 20 µm.

Figure 5.2 shows a group of RPE cells at two different representative locations in the macular area for three different donor eyes at the ages of 54, 55 and 62 years. Additionally, each image is represented in false-color LUT for better visualization of the relative fluorescence distribution inside the cell. Considerable variations in accumulated lipofuscin load appear in different eyes and location but have in common to be most dense in the peripheral cytoplasm along the cell wall and centrally above the cell nucleus (observed as non fluorescent dark region) (see also Figure 5.3). Most of the free cytoplasmic area is occupied by lipofuscin. The single granules typically have a spherical shape of 0.5 to 1.0 µm in diameter, which is consistent with other ultrastructural studies [Boulton et al., 1989; Haralampus-Grynaviski et al., 2001; Han et al., 2006]. The prominent fluorescence

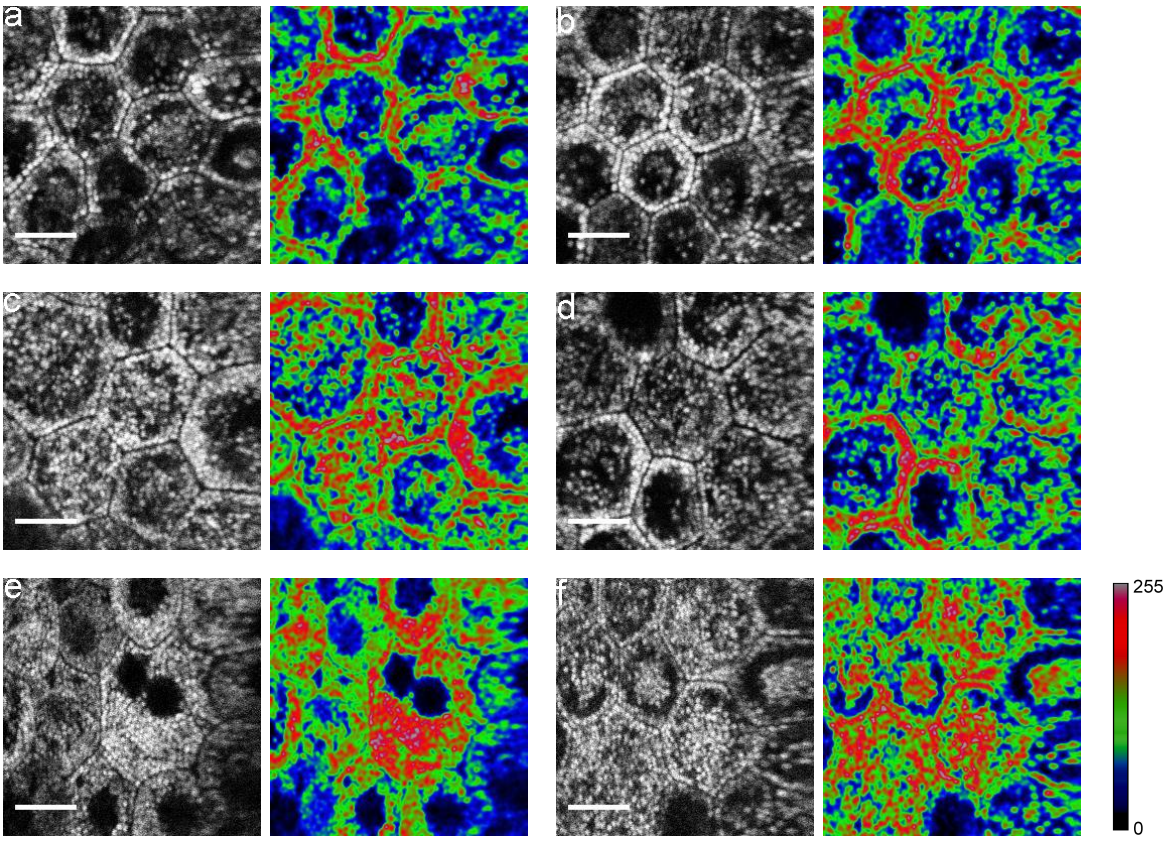

Figure 5.2: TPEF images of RPE cells of a 55 (a,b), 54 (c,d), and 62 (e,f) year-old donor eye at two different locations in the macular area. For better visualization of the fluorescence intensity distribution, a false-color representation of each image is shown, with high intensities mapped in red, low intensities in blue. Scale bar, 10 µm.

along the cell wall allows to delineate the size and shape of the RPE cells. Their typical size is around 15 µm but can be as large as 23 µm associated with alterations from their characteristic hexagonal shape. Larger double nuclei cells with increased lipofuscin load (Fig. 5.2 e, f) were observed, but most cells had one nucleus only.
The average excitation power of the Ti:Sa laser used for imaging the RPE cells was 4–6 mW at the sample. At this power level no noticeable photodamage nor bleaching was observed, even after repetitive exposures.

To demonstrate the dependency of the two-photon excited autofluorescence intensity to the square of the excitation laser light applied, a 50/50 beamsplitter was put in the excitation path directly behind the neural density filter wheel (ND), in order to split the laser beam into two parts, one leading as excitation beam to the sample, the other one

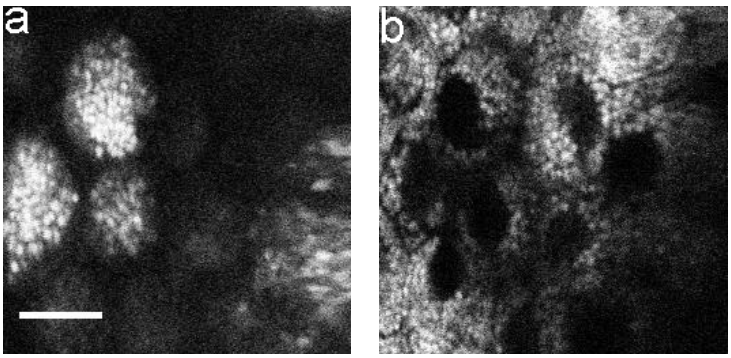

Figure 5.3: RPE cells of a 62-year-old human donor eye in the macular region, imaged at two different focusing depth along the optical axis, separated by approximately 10 µm. LF granules are most prominent along the cell wall and on top of the cell nucleus. Scale bar, 10 µm.

leading to a power meter (Nova, Ophir Optronics[1]) to measure the relative excitation laser power. The fluorescence intensity with changing laser power was measured as mean gray value of the recorded image of the RPE cells in focus. The results are plotted in Figure 5.4. Higher excitation powers than the ones listed, resulted in either saturation of the APD or bleaching of the specimen in focus. Measured values best fit to a nonlinear plot of 2.09 ± 0.06 power. This clearly indicates two-photon excitation.

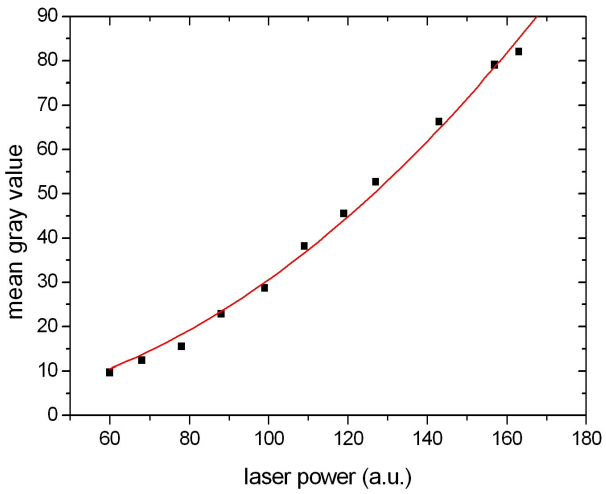

Figure 5.4: Fluorescence signal from RPE cells as a function of the applied excitation laser power at $\lambda_{ex} = 831$ nm. The *red* curve is a nonlinear best fit to the measured data of 2.09 ± 0.06 power.

The two-photon excited autofluorescence spectrum of the RPE cells was measured as the integrated signal from a 210 µm × 210 µm area (∼ 270 cells) for five different x-y-

[1]Logan UT, USA; `http://www.ophiropt.com`

locations on the specimen. The averaged emission spectrum is given in Figure 5.5. The calculated mean fluorescence emission band ranges from approximately 440 to 720 nm (limited by the barrier filter), and peaks at 553 ± 5 nm. These values are in general agreement with previously published results from different authors on single-photon emission spectra from cellular lipofuscin [Delori et al., 1990, 1995a; Haralampus-Grynaviski et al., 2003], most of which concentrated on the emission spectrum from individual lipofuscin granules. Because the lipofuscin granules are composed of a number of distinct blue-absorbing chromophores [Eldred and Katz, 1988], deviations in emission wavelength are likely to originate from the different excitation wavelength employed, as to the change in the relative contribution from different fluorophores to the overall emission spectrum as a function of excitation light. Age-dependent emission properties of lipofuscin have been reported as well [Han et al., 2006; Boulton et al., 1990], and are likely to result from concentration variations of the composing fluorophores or from the presence of other proteins inside the granules that reflect age-related modifications in the RPE but are yet to be identified.

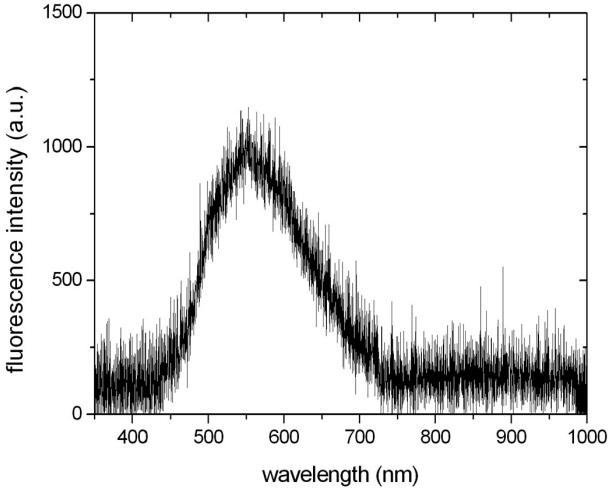

Figure 5.5: Two-photon excited autofluorescence emission spectrum of RPE cells from a 54-year-old human donor eye at $\lambda_{ex} = 831$ nm excitation wavelength, measured as the integrated signal from a 210 µm × 210 µm scanning area. The average of five measurements acquired at different x-y-locations within the same specimen is shown.

5.2.2 Comparison to Single-Photon Excitation

Due to the longer excitation wavelength employed in two-photon microscopy, resolution appears prima facie somewhat worse that in single-photon confocal fluorescence imaging. Whereas for confocal microscopy the axial extend of the PSF is not much better than for conventional microscopy, for thick specimens, the confocal and two-photon microscopes show a substantial improvement in true axial resolution, i.e. axial discrimination, due to their optical sectioning properties. In conventional fluorescence microscopy, the laterally integrated intensity of the PSF is constant as a function of depth. Consequently, a conventional microscope has no depth discrimination. The integrated intensities of the

confocal and two-photon fluorescence microscope PSFs $\int_r h_{ill}(r,z)h_{det}(r,z)2\pi r dr$ and $\int_r h_{ill}^2(r,z)2\pi r dr$, respectively, have a maximum in the focal plane. As a result, only the fluorophores in the immediate vicinity of the focus are observed.

For confocal microscopy, these figures are based on the ideal concept of an infinitely small pinhole. The effectiveness of a confocal pinhole is related to its size, and is always a compromise between achieved resolution and signal strength. In practical biological fluorescence imaging, where photons are scarce, one rarely appreciates the full resolving power of the confocal pinhole. Even though for a pinhole size larger than 1 Airy unit, the lateral and axial resolution are essentially equivalent to conventional fluorescence microscopy for point-like objects [Cox and Sheppard, 2004], it greatly affects the depth resolving capability in thick samples [Jonkman and Stelzer, 2002; Conchello and Lichtman, 2005].

Contrary to single-photon fluorescence, where illumination causes the entire specimen thickness to fluoresce, the two-photon absorption process is limited to the focal volume and out-of-focus fluorescence is absent. The resolution and optical sectioning capability are intrinsically only determined by the excitation process, and no pinhole is used. Therefore the *practically* achievable resolution in two-photon microscopy is comparable to ideal confocal microscopy (except for the longer wavelength), without compromising signal strength.

In Figure 5.6, a group of RPE cells from a 55-year-old donor eye is imaged in confocal single-photon excited fluorescence mode at two different focusing depths separated by approximately 10 µm (i.e. about the height of the RPE layer). The confocal pinhole has a size of 75 µm, corresponding to approximately 2.2 Airy units for a fluorescence emission wavelength of λ_{fl} peaking around 550 nm. One observes that "true" confocal sectioning is partially lost, as unwanted fluorescence light from the planes above and below the focal plane is not sufficiently removed and contributes to the image by reducing image detail and contrast. Figure 5.6 a is recorded above Figure 5.6 b. The strong autofluorescence from lipofuscin granules along the cell walls appears as diffuse out-of-focus background in Fig. 5.6 a, demonstrating the loss in depth discrimination power at the pinhole size employed. Also in Fig. 5.6 b, a background glow that degrades the image contrast is perceivable. The excitation power of the blue laser light was typically around 8 µW at the sample.

The effect on axial resolution in direct comparison to two-photon excitation is demonstrated in Figure 5.7, showing a group of RPE cells imaged by two-photon and single-photon excited fluorescence. Similar but not identical fields within the same sample were imaged. The loss in depth resolution in single-photon imaging mode is again obvious. In-focus details are largely obscured by superimposed out-of-focus fluorescence. On the other hand, the two-photon image gives a thin optical slice of the focal plane with markedly improved overall contrast and detail.

Obviously, the confocal pinhole employed in the setup for single-photon imaging is rel-

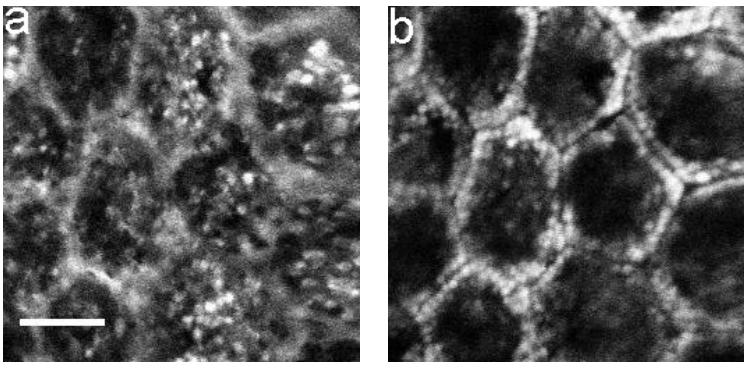

Figure 5.6: Single-photon excited autofluorescence optical sections through the RPE from a 55-year-old donor eye at two different focusing depths along the optical axis, separated by approximately 10 µm. Scale bar, 10 µm.

atively large for high-resolution imaging, and is always a compromise to achieved signal strength. Nevertheless, the direct comparison clearly puts the two imaging modalities in perspective. In two-photon microscopy, intrinsically optimal imaging conditions are achieved with no practical constraints on the resolution limit predicted by theory. Resolution and depth-of-field in thick samples are an only function of excitation wavelength and numerical aperture of the focusing optics (and are not dependent on the optical design of the detection system). Out-of-focus glare, as it occurs in practical confocal imaging, is absent, allowing more reproducible images for morphological analysis and mapping of quantitative data at fully available depth definition.

5.3 Imaging the Neural Retina

In the living eye, the neurons in the retina are all quite transparent so as not to interfere with the light on its way to the photoreceptors. In the following section, the neural retina from human donor eyes is imaged by two-photon excited fluorescence based on the tissue's intrinsic fluorophores.
The photoreceptor inner and outer segments as well as the retinal nerve fiber layer and the underlying ganglion cells are shown to generate an autofluorescence signal upon two-photon excitation. This is, to the best of our knowledge, the first report on two-photon excited fluorescence imaging on endogenous fluorophores of the retinal nerve fiber and ganglion cell layer from human donor eyes. These results are of particular importance, as they demonstrate a potential novel non-invasive diagnostic and monitoring technique for another large group of ocular pathologies that are characterized by a degeneration of the nerve fibers and the underlying ganglion cells, e.g. glaucoma.

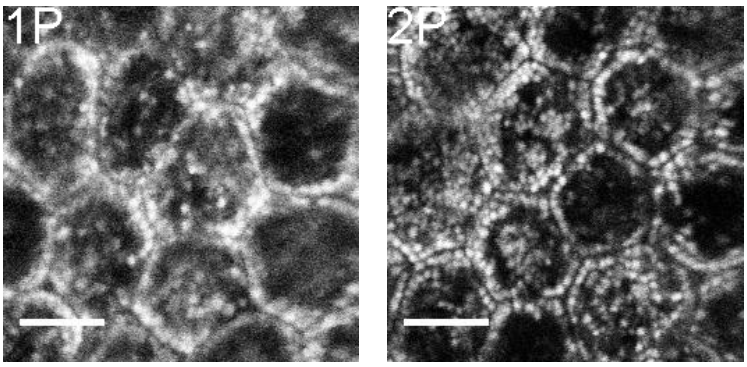

Figure 5.7: Comparative single-photon (1P) and two-photon (2P) excited autofluorescence imaging of RPE cells from a 55-year-old donor eye taken at a similar focal depth for $\lambda_{ex,1P} = 488$ nm and $\lambda_{ex,2P} = 831$ nm, respectively. Scale bar, 10 µm.

5.3.1 TPEF Imaging of Photoreceptors

Initial experiments on photoreceptor cells were done with the neural retina turned upside-down, i.e. with the photoreceptors facing the objective.

Figure 5.8 shows the photoreceptors of a 54-year-old human donor eye at the parafovea at different focusing depth. The spatial mosaic arrangement of individual rods and cones is clearly depicted by their relative two-photon excited autofluorescence signal.
Fig. 5.8 a shows the endings of the elongated outer segments of the rod cells. The endogenous fluorescence in the outer segments was shown to be mainly derived from all-*trans*-retinol, which is produced during the visual cycle [Chen et al., 2005].
The fainter autofluorescence in Fig. 5.8 b defines the photoreceptor inner segments. The signal was reported to originate predominately from mitochondrial reduced pyridine nucleotides NAD(P)H [Chen et al., 2005] in the ellipsoid region of the inner segments. Inner segment regions of both rods and cones are filled with numerous long thin mitochondria. However, NAD(P)H has a low two-photon excitation efficiency at wavelengths longer than 800 nm, and its fluorescent redox partner flavin adenin dinucleotide FAD, whose two-photon excitation spectrum extends up to 1000 nm, is more likely to be excited [Huang et al., 2002]. This is also supported by the measured fluorescence emission spectrum of the photoreceptor inner segments, shown in Figure 5.9, which is considerable blue-shifted compared to the fluorescence emission of NAD(P)H peaking at 450 nm. Contributions from outer segment retinol to the emission spectrum cannot be excluded, as it is not always obvious to differentiate between inner and outer segments from two-dimensional x-y-cross-sections. The average illumination power for imaging the photoreceptors was 8–10 mW at the specimen.

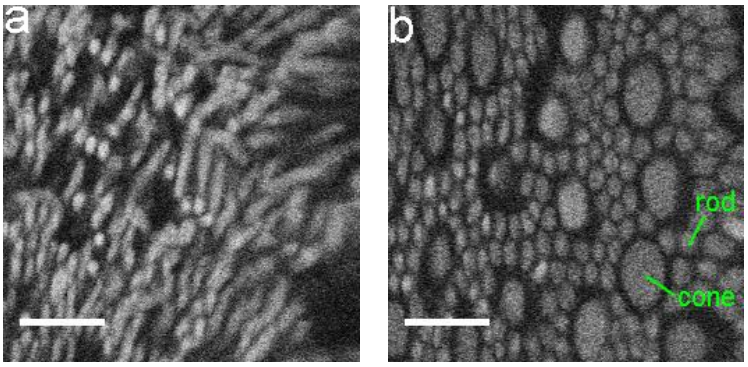

Figure 5.8: Two-photon excited autofluorescence optical sections through photoreceptors at two different focusing depth along the optical axis, at the level of the outer segments (a), and the inner segments (b), in the parafovea. Scale bar, 10 μm.

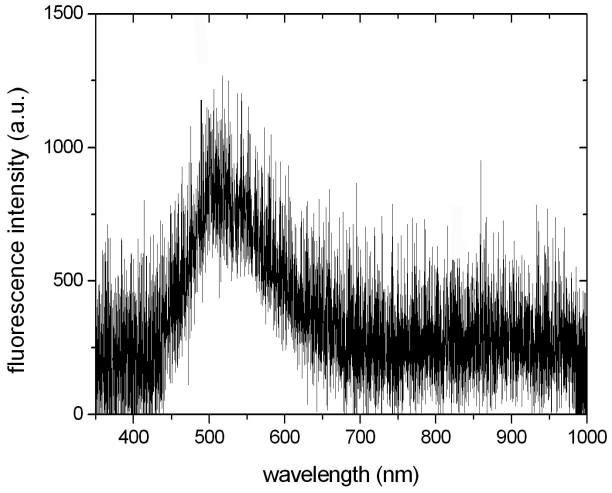

Figure 5.9: Two-photon excited autofluorescence emission spectrum of photoreceptor inner segments at $\lambda_{ex} = 831$ nm excitation wavelength, measured as the integrated signal from a 210 μm × 210 μm scanning area. The average of five measurements acquired at different x-y-locations within the same specimen is shown.

5.3.2 TPEF Imaging of Ganglion Cells

In the human eye, there are about one million retinal ganglion cells, each sending the visual information produced in the photoreceptors through one axon across the retina to the optic nerve head. They provide the retinal output signal to the visual cortex in the brain. The individual axons have a diameters of 0.2 to 3.9 µm [Odgen, 1984]. They are grouped into fiber bundles, with cross-sectional dimensions of 10–100 µm [Odgen, 1980], partitioned by vertical columns (glial tunnels) that are formed by Müller-cell processes within the retinal nerve fiber layer [Radius and Anderson, 1979].

A number of optic neuropathies are associated with a degeneration of the nerve fiber bundles. Pathologies of the nerve head, papilla, or superficial layer of the retina have in common a focal destruction of the nerve fiber layer [Hoyd et al., 1972]. Particularly glaucoma, the second leading cause for irreversible legal blindness worldwide, is characterized by a progressive loss of retinal ganglion cells associated with visual functional deficits [Harwerth and Quigley, 2006]. As the ganglion cells die in glaucoma, there is a progressive thinning of the nerve fiber layer due to died fibers (along with their cell bodies). The underlying pathophysiological mechanisms of the disease, however, still remain unclear.
Clinically detectable nerve fiber atrophy precedes the onset of glaucomatous field loss [Sommer et al., 1977, 1991; Tuulonen et al., 1993]. Recognizing the morphological abnormalities prior to visual field loss is clinically important for the early diagnosis of the disease. The optic nerve head and the retinal nerve fiber layer are the sites for early detectable glaucomatous tissue damage [Quigley and Sommer, 1987]. The early diagnostic and assessment of degenerative patterns is of primary importance in disease abatement to provide treatments before resulting functional damage occurs.

In clinical practice, the retinal nerve fiber layer is traditionally observed by direct red-free (green or blue reflectance) ophthalmoscopy. As green/blue light is absorbed by melanin of the RPE and choroid, the reflectance at the nerve fiber layer stands out against a black background [Quigley and Sommer, 1987], its brightness being proportional to its thickness. It is recognized as a pattern of subtle striations near the inner surface of the retina [Radius and Anderson, 1979; Hoyd et al., 1972]. The boundaries of the axon bundles are delimited by the dark thickened Müller's cell end-plates.
Early defect findings of glaucoma are a localized thinning of the nerve fiber layer or, most commonly encountered but more difficult to detect, a mild diffuse fiber loss in the upper or lower arcuate area around the optic nerve head. The sensitivity of this method is however limited in detecting early atrophic stages, as variations in nerve fiber layer thickness are only observable when a considerable number of fibers are already lost [Quigley and Sommer, 1987; Kerrigan-Baumrind et al., 2000].
In the last ten years a variety of new non-invasive imaging technologies (including confocal scanning laser ophthalmoscopy, optical coherence tomography, scanning laser polarimetry) emerged for the objective measurement of structural changes secondary to retinal

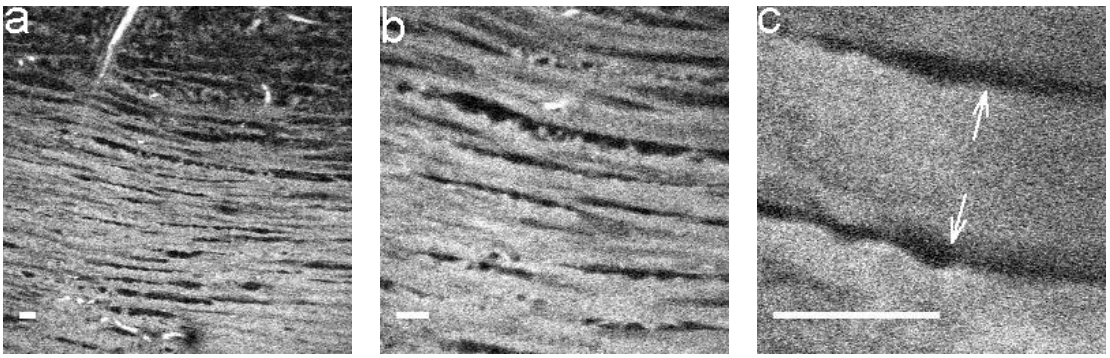

Figure 5.10: Two-photon excited autofluorescence of the retinal nerve fiber layer for different scan angles in the parafovea. Scale bar, 20 µm.

ganglion cell damage, involving the detection of characteristic glaucomatous damage by automated analysis of quantitative variables, such as the size and volume of the neuroretinal rim, disc area, cup-to-disc ratio, and thickness of the retinal nerve fiber layer at the optic disc border [Renard et al., 2005; Hoffmann et al., 2007]. Even though these methods have the advantage of additional objective precision and reproducibility for quantitative follow-up, glaucoma still remains a challenging disease as there is no general agreement on criteria for glaucoma diagnosis [Quigley, 1996].

In this study, we found an intrinsic fluorescence signal generated from the inner surface of the retina upon two-photon excitation. Figure 5.10 shows the retinal nerve fiber layer for different scan angles in the parafovea. The retinal striations, which represent bundles of individual axons, are clearly differentiated from non-fluorescing dark boundaries presumably formed by Müller-cell end-plates near the retinal surface, marked by arrows in Fig. 5.10 c. At the level of the blood vessels that supply the inner retina, one can see at the upper end in Fig. 5.10 a what are believed to be the underlying ganglion cells bodies whose axons compose the nerve fiber layer. Figure 5.11 shows individual axons processing from the underlying ganglion cell bodies into nerve fiber bundles. In Figure 5.12, a z-stack from the nerve fiber layer (Fig. 5.12 a) through the ganglion cell layer (Fig. 5.12 b–f) is shown. The non-fluorescing band in the image center is a blood vessel. The ganglion cellular region is delimited by its intrinsic blue/green fluorescence. The cell nucleus appears dark (no fluorescence signal).

Figure 5.13 shows the central part of the optic nerve head cup imaged by intrinsic two-photon excited fluorescence. Fig. 5.13 a displays the innermost layer of the retinal nerve fiber bundles that merge into the optic head where they form the neuroretinal rim. The striations become less distinct as the crowded bundles are thicker and incompletely divided by Müller cells [Quigley and Addicks, 1982]. Fig. 5.13 b is imaged deeper into the tissue than Fig. 5.13 a and shows the optic head with the most central nerve fibers

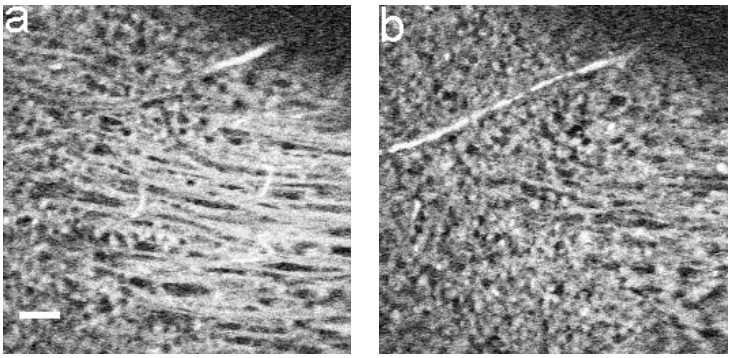

Figure 5.11: Optical sections through the retinal ganglion cell bodies and their axons processing into nerve fiber bundles imaged by two-photon excited autofluorescence. The images are separated by approximately 10 µm in z-direction. Scale bar, 50 µm.

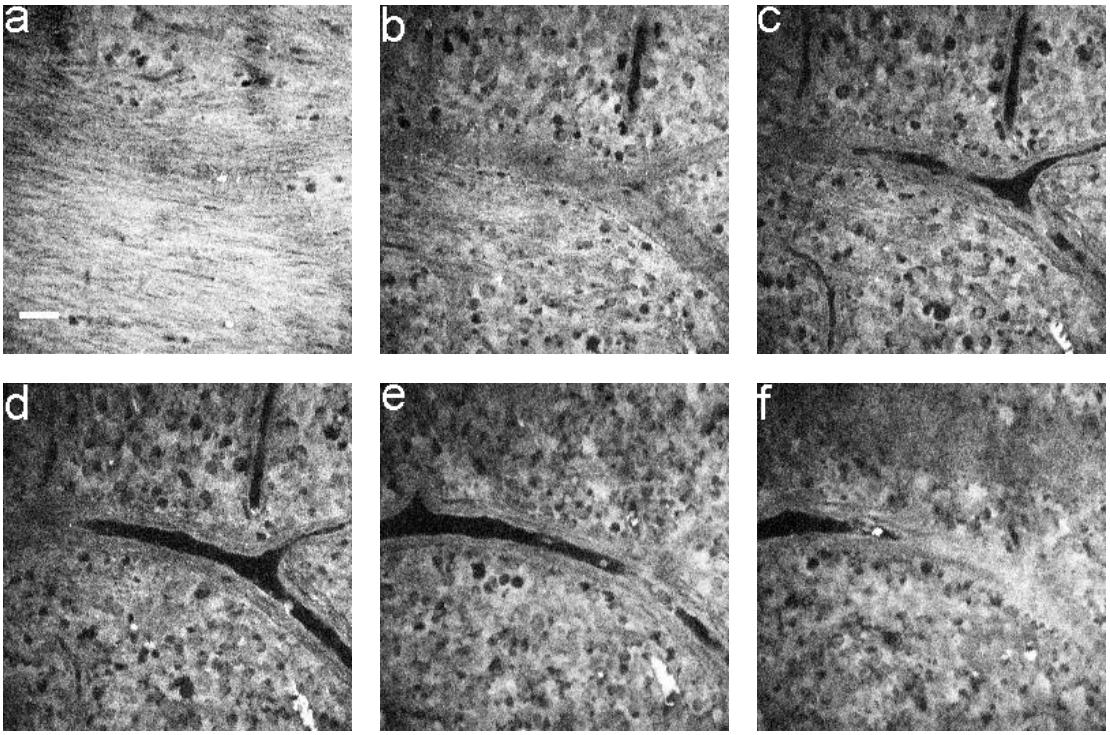

Figure 5.12: Optical sections through the inner retina, from the retinal nerve fiber layer (a) through the ganglion cell layer (b–f) imaged by two-photon excited autofluorescence. The individual images are separated by approximately 10 µm in z-direction. Scale bar, 50 µm.

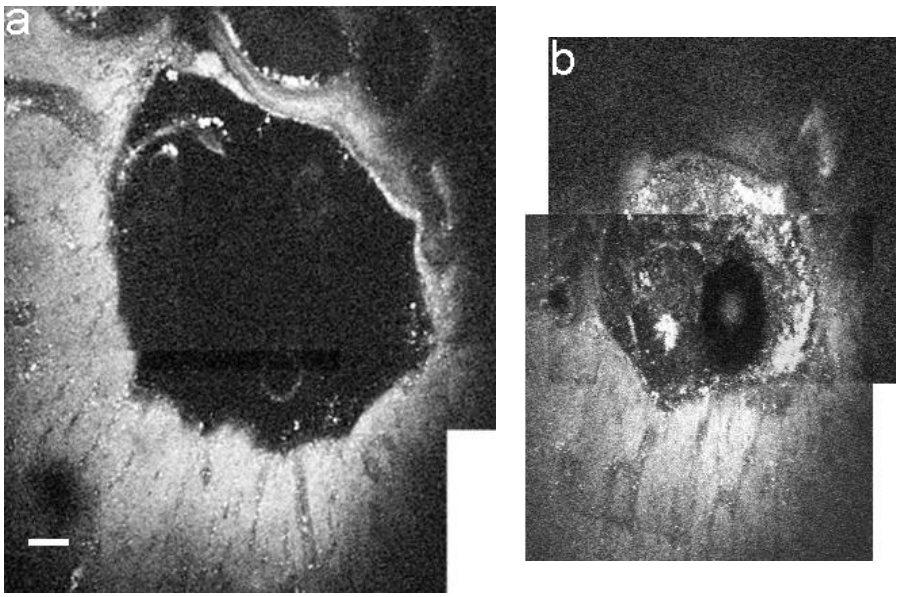

Figure 5.13: Intrinsic two-photon excited fluorescence of the retinal nerve fibers at the center of the optic nerve head at two different focusing depth. All 10^6 nerve fibers curse into the optic nerve head forming the neuroretinal rim (a). Deeper within the tissue, the fibers merge toward the brain, perpendicular to the retinal surface (b). Scale bar, 50 µm.

already facing perpendicular to the retina surface. The bright fluorescence is believed to arise from the optical cross-section through the high density of all the central retinal nerve fibers collected together that proceed to the brain, and possibly also from collagen and elastin in the connective tissue of the optic nerve head. The dark circle in the center outlines the central retinal artery that provides the blood supply to the inner retina. The average excitation power used for imaging was typically 8–10 mW at the specimen.

The fluorescence spectrum of the ganglion cell complex (cell bodies and axons) upon two-photon excitation has been measured in Figure 5.14 as the average value for three different x-y-locations within the specimen. The fluorescence emission ranges from approximately 430 to 690 nm and peaks at about 525 ± 5 nm. Several native fluorophores may be contributing to the fluorescence intensity in this blue emission range. From the combined emission spectrum alone one cannot directly back-reference on a specific marker, and additional immunochemistry or fluorescence decay time measurements [Schweitzer et al., 2007] would be necessary, so we can only speculate on the responsible fluorophores. In the nerve fibers the fluorescent components are unknown, whereas in the ganglion cell bodies the major fluorescence would be expected to originate from mitochondrial oxidized flavin proteins, such as the yellow emitting flavin adenine dinucleotide (FAD, the oxidized

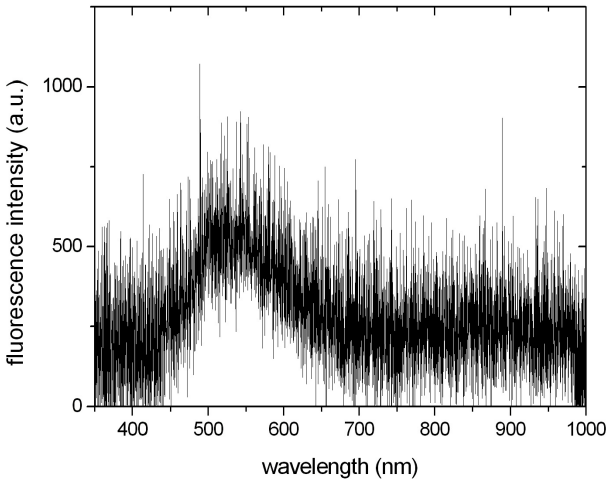

Figure 5.14: Two-photon excited autofluorescence emission spectrum of the ganglion cell layer (cell bodies and axons) at $\lambda_{ex} = 831$ nm excitation wavelength, measured as the integrated signal from a 210 µm × 210 µm scanning area. The average of three measurements acquired at different x-y-locations within the specimen is shown.

fluorescent form of the redox pair FAD-FADH2) that has a single emission maximum at 524 nm and has been proposed before as contributing fluorophore to FAF [Teich, 1985; Schweitzer et al., 2002]. Contributions from reduced NAD(P)H are likely as well, but their excitation efficiency is considerably reduced above 800 nm [Huang et al., 2002].

Concluding, we found that intrinsic two-photon excited fluorescence makes it possible to image the "transparent" ganglion cell bodies as well as the localized structure of their axons in their natural state, which possibly allows to look "deeper" in retinal nerve fiber defects as expected by simple ophthalmoscopy based on reflective structures. Defects in the ganglion cell bodies can potentially be localized before being detected in the nerve fiber layer. This may help in the understanding and early diagnostic of associated visual degenerative impairments. In particular, it may provide an answer to the important open question whether the glaucomatous optic neuropathy is the result of an axonal insult or whether its origins are found in the ganglion cell soma [Nickells, 2007]. Experimental studies on animal models toward this goal are thinkable.

5.4 Imaging through the Neural Retina

For a potential clinical application of two-photon excited fluorescence in the intact retina, the excitation laser light has to be focused through the neural part of the retina for imaging the RPE cells. Due to the long excitation wavelength in the NIR, TPEF has been reported to be the technique of choice for fluorescence imaging of cellular structures in thick scattering tissue [Helmchen and Denk, 2005; Periasamy et al., 1999]. During the specimen preparation, the RPE layer usually separated without any manual assistance from the overlying photoreceptors. On one specimen from 54-year-old donor eye however, parts of the RPE layer remained attached to the retina around the foveal region, which

could be used for imaging. The result is shown in Figure 5.15. In order to reduce single pixel noise, a 2D Gauss filter was applied.

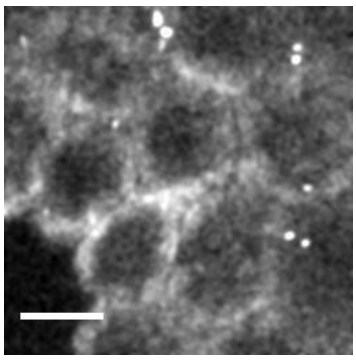

Figure 5.15: Two-photon excited autofluorescence of RPE cells of a 54-year-old donor eye in the foveal region, imaged through the overlying neural retina. Scale bar, 10 µm.

Most of the structural details are lost, which is probably related to the fixation in paraformaldehyde, provoking a change in the tissue's optical properties of the nearly transparent neural retina under normal conditions. Scattering and local changes in refractive index or heterogeneities caused by cellular components in the neural retina induce depth-dependent degradations to the illumination PSF, which further reduce the two-photon excitation effectiveness [Enger and Hell, 2006; Gerritsen and De Grauw, 1999]. Large-angle rays of the illumination cone are more likely to be scattered than central-rays, as they travel a longer distance to the focus, which leads to a reduction of the objective's effective NA in scattering samples. The scattering effect is dependent on imaging depth and wavelength, and is even more pronounced in single-photon imaging employing a blue excitation source, where additionally scattered photons will excite fluorophores, adding out-of-focus background to the detected signal. This was shown to result in a penetration depth of less than half the one achieved with two-photon microscopy [Centonze and White, 1998; Gerritsen and De Grauw, 1999].
Fluorescence emission scattering is another source of signal loss in deep tissue imaging. But since in two-photon microscopy no background fluorescence is produced due to the spatially localized nonlinear signal generation, all scattered emission photons carry useful signal in-focus information and losses in signal can be compensated by increasing the average excitation power without compromising imaging contrast.
The present measurements were done using an average excitation power of the scanning illumination laser beam at the sample of $\sim$ 10–12 mW and show that even under very weak optical conditions of the overlying retina ($\sim$ 250 µm thick around the fovea) still an appreciable two-photon excited fluorescence signal can be gathered from the strong autofluorescing lipofuscin granules in the RPE cells. One can however expect much better results in fresh resp. living tissue in both spatial resolution and signal strength, so

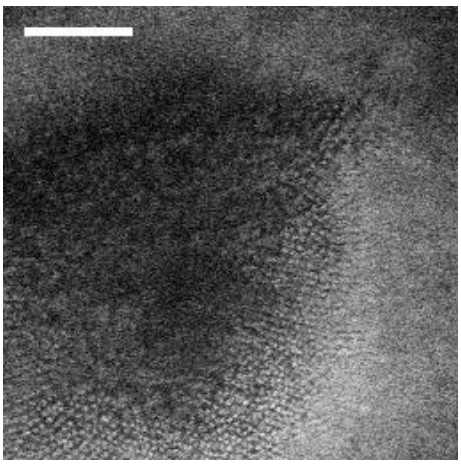

Figure 5.16: Two-photon excited autofluorescence of the foveal cones imaged in the upright, intact tissue around the foveal pit. Scale bar, 50 µm.

that the above result on fixed-tissue is not really representative to reflect in vivo imaging conditions.

Figure 5.16 shows the tightly packed cones in the central fovea. Here, most of the overlying inner neural retinal layers are concentrically displaced, and the cones reveal to be accessible by TPEF in the upright, intact tissue.

5.5 Measurements with a Nd:Glass Oscillator

The feasibility of two-photon excited autofluorescence imaging for the human retina is also tested using a compact, all-diode pumped Nd:Glass femtosecond laser oscillator (*femto*TRAIN™ Nd:Glass, High Q laser production GmbH[2]) instead of the Ti:Sa laser unit in Figure 4.4. The Nd:Glass oscillator has a pulse repetition rate of 75 MHz. The pulse width at a fixed central wavelength of 1054 nm is 256 fs. The maximum average output power is around 140 mW.
The advantage of the Nd:glass system is its compactness that makes it suitable for a miniaturized, turn-key clinical two-photon imaging setup without the need of an external pumping laser. The less-scattering long-wavelength laser light allows even deeper penetration depth at potentially reduced photodamage in the living eye. The optimal excitation wavelength is however ultimately determined by the absorption spectrum of the fluorophores to be excited.

Figure 5.17 a shows the two-photon autofluorescence signal of RPE cells from a 54-year-old donor eye excited at 1054 nm. The loss in lateral resolution due to the longer

[2]Hohenems, Austria; `http://www.highQlaser.com`

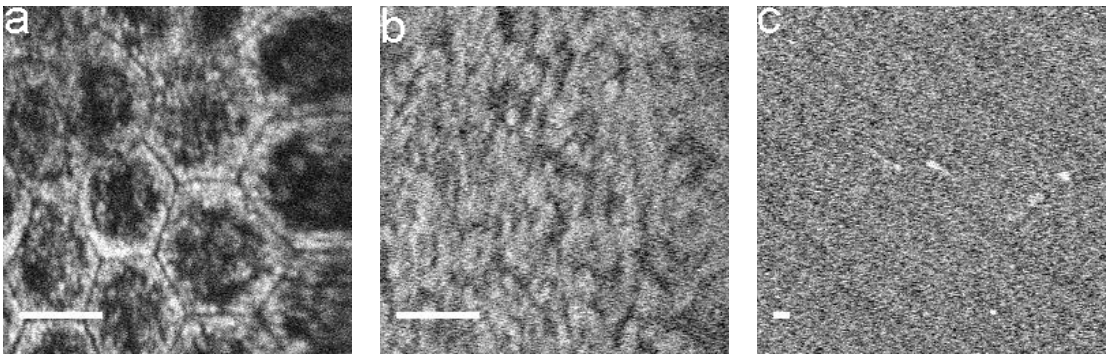

Figure 5.17: Two-photon excited autofluorescence of RPE cells (a), and photoreceptor outer segments (b) at 1054 nm excitation wavelength from a Nd:glass fs-oscillator. Scale bar, 10 µm.

wavelength compared to the Ti:Sa laser employed in the previous measurements is obvious. From Eq. (3.67) one calculates a reduction by a factor of $1054/831 = 1.27$, for the same objective used. The average excitation power of the Nd:glass laser for imaging the RPE was typically ~ 13 mW after the objective.

The photoreceptors excited at 1054 nm are shown in Figure 5.17 b. The outer segments give a very weak fluorescent signal at full excitation power, i.e. 26 mW at the sample. Due to strong losses of the 1054 nm illumination light in the optical pathway (mirrors, lens surfaces), the setup did not allow more excitation power at the sample. Also was it not possible to get an autofluorescence signal from the photoreceptor inner segment. This is most probably because for the major endogenous fluorophores NAD(P)H in the inner segment, the two-photon excitation efficiency for wavelengths over ~ 920 nm becomes vanishingly small [Zipfel et al., 2003b]. For the nerve fiber layer (Fig. 5.17 c) the fluorescent signal was very poor at the illumination power levels available.

Even though the absolute two-photon action cross sections for RPE lipofuscin and POS retinol are not known, using the expression for the time averaged two-photon fluorescence intensity per molecule

$$I_f \propto \frac{P^2}{\tau f}\sigma(\lambda)\left(\frac{\mathrm{NA}^2}{2\hbar c\lambda}\right)^2, \tag{5.1}$$

one can estimate from

$$\frac{I_{fl,A}}{I_{fl,B}} = \frac{P_A^2}{P_B^2}\cdot\frac{\sigma(\lambda_A)}{\sigma(\lambda_B)}\cdot\frac{\tau_B f_B}{\tau_A f_A}\cdot\frac{\lambda_B}{\lambda_A} \tag{5.2}$$

with the parameters of the Ti:Sa and the Nd:Glass lasers[3], resumed in Table 5.1, that the

[3]except for the laser source, the optical setup was identical in both cases

two-photon cross section, i.e. the two-photon absorption efficiency, for RPE lipofuscin at 1054 nm is reduced by a factor

$$\frac{\sigma(831)}{\sigma(1054)} \approx 5.3 \pm 1.2 \tag{5.3}$$

as compared with an excitation at 831 nm. For the photoreceptor outer segments, this ratio can be expected to be 12.4 ± 3.2. For the nerve fiber layer the signal was to weak to make any meaningful comparison. Consequently, the Nd:Glass oscillator does not appeal very attractive for two-photon excited fluorescence imaging on the human retina, even more when considering the ocular spectral transmission properties which decrease to less than 50% at 1054 nm [Geeraets and Berry, 1968].

Table 5.1: Measurement parameters for imaging RPE and photoreceptor cells with a Ti:Sa and a Nd:Glass laser system. POS = photoreceptor outer segment.

		Ti:Sa	Nd:Glass
wavelength λ [nm]		831	1054
pulse width τ [fs]		182	256
repetition rate f [MHz]		76	75
excitation power P [mW]	RPE	5 ± 1	13 ± 1
	POS	9 ± 1	26 ± 1
fluorescence intensity[a] I_{fl} [a.u.]	RPE	220 ± 3	159 ± 9
	POS	163 ± 12	62 ± 13

[a] The relative fluorescence intensity was calculated as the mean value of the difference between highest and lowest gray value (spread over a minimum of 10 pixels) in the fluorescence image for three different x-y-locations on the specimen after being Gauss filtered to reduce single pixel noise.

6 Testing the Influence of Pixel Dwell Time on Fluorescence Yield

Surprised by the brightness of the fluorescence images acquired with our resonant scanning ophthalmoscope-based microscope, we are interested in the influence of the scan speed on the fluorescence outcome.

In the past, resonant scanning devices have been ignored for fluorescence microscopy, as to the common believe that, due to the fast scanning, not enough signal would be excited to get a reasonable signal-to-noise ratio if not the illumination intensity was increased considerably. However, recent studies have shown that the fluorescence yield can be substantially improved when choosing an illumination scheme that avoids the build-up of fluorophores caught in a non-fluorescing triplet state. Pulsed laser sources for two-photon excited fluorescence imaging typically operate at a repetition rate of 70–100 MHz, which corresponds to a time period Δt of 10–15 ns between two consecutive pulses. Reducing Δt increases the probability of illuminating molecules still in the excited state of a typical lifetime of a few ns, whereas longer Δt would leave the fluorophore idle between two excitation events, which both seem unattractive at first sight. Considering however that with every absorption event a number of molecules get caught in long-lived triplet states with typical lifetimes of a few µs, it was demonstrated by Donnert et al. that for both single- and two-photon excitation, the detected fluorescence signal is substantially increased by reducing the repetition rate below 1 MHz [Donnert et al., 2007]. Intermissions of $\Delta t > 1$ µs allow transient molecular dark states, such as the triplet state, of similar lifetime, to relax between two molecular absorption events and consequently increase the total number of photons emitted by a dye. This illumination scheme was shown to also depress photobleaching which is commonly generated over secondary triplet absorption pathways. Such an all-physical increase in fluorescence signal is of particular interest when imaging endogenous fluorophores that inherently suffer from low absorption cross-sections and excitation efficiency needs to be maximized.

Although there is no experimental data published yet, the above findings suggest that alternatively to reducing the repetition rate of the excitation laser, fast scanning devices may produce similar results [Donnert et al., 2007; Borlinghaus, 2006; Tsien et al., 2006; Conchello and Lichtman, 2005]. As succeeding pulses will illuminate different molecules, the build-up of dark triplet states is repressed and consequently, signal yield will be increased.

6.1 Methods

To study the effect of scan speed on two-photon excited fluorescence yield in RPE cells, we used a commercial multiphoton laser scanning microscope (Zeiss LSM 510 NLO[1]) which allowed variable scan speed settings. The microscope was equipped with a Ti:Sa fs-laser (Chameleon XR, Coherent Inc.) operating at 80 MHz repetition rate. The excitation wavelength was set according to our previous measurements to 831 nm. The fluorescence signal was detected in non-descanned mode by a PMT assigned to a 500–550 nm spectral window.
Our aim was to compare image brightness for different scanning speeds at fixed detector/amplifier settings (i.e. gain, offset) and identical excitation power for a group of RPE cells.
All images were acquired using a 63×/1.0 W objective (W-Plan Apochromat VIS-IR, Zeiss) at 256 × 256 pixels, corresponding to a field of view of 60 µm × 60 µm.

The effective time that is ruling the dose-rate effect, is the time a fluorophore is illuminated. This time depends on the diameter of the illumination spot at the sample and on the speed at which it is moved. Using Eq. (3.67), the diffraction limited FWHM of the squared illumination PSF is approximately 320 nm. As the laser sweeps across the sample, a molecule is thus excited during the effective time $t_{\text{eff}} = \text{FWHM}/v$, where v is the speed of the illumination laser beam in the focal plane determined by the pixel dwell time. With the above configuration, the microscope allowed a maximum scan speed of 1.92 µs/pixel, corresponding to an effective excitation time of $t_{\text{eff}} = 0.32\mu\text{m}/(\frac{0.23\mu\text{m}}{1.92\mu\text{s}}) = 2.6$ µs. Accordingly, as the laser sweeps across the sample, a molecule is hit by ~ 210 pulses. The slowest scan speed setting was chosen to correspond to a pixel dwell time of 102.4 µs/pixel, which is about the time scale for scan speeds traditionally encountered in two-photon microscopy. In this case, a molecule is hit by ~ 11200 consecutive pulses for one pixel. To minimize the effect of photobleaching during the measurements, the laser power was reduced as much as possible while still generating enough fluorescence to be quantitatively detectable. All images to be compared were performed using the same excitation dose, i.e. the same number of pulses per molecule but for different time intervals compared to the slowest pixel dwell time setting of 102.4 µs/pixel, by repeatedly scanning over multiple frames. Table 6.1 lists the effective illumination time per molecule, number of pulses per molecule per frame, and number of averaged frames for each scan speed setting. For each image the corresponding dark image was subtracted, and brightness, as measure for the fluorescence yield, was calculated as mean gray value.

Further it was found, upon communication with Zeiss GmbH, that despite fixed system parameters for PMT voltage, amplifier gain and offset, the Zeiss LSM 510 works with a second internal signal amplification that is dependent on the scanning speed and cannot be controlled by the user. Therefore, the system was first calibrated on the relative

[1] Carl Zeiss Microimaging GmbH, Jena; `http://www.zeiss.de`

Table 6.1: Overview of the different available scanning speeds and corresponding illumination parameters chosen to probe the dependency of fluorescence yield on scan speed.

pixel dwell time (µs/pixel)	t_{eff} (µs)	pulses per molecule per frame	number of frames
1.92	2.6	210	53
3.2	4.4	350	32
6.4	8.7	700	16
12.8	17.5	1400	8
51.2	70	5600	2
102.4	140	11200	1

fluorescence of fluorescein. Fluorescein is known for its high fluorescence quantum yield (about 0.9) and low triplet crossing rate (about 0.02–0.03) [Song et al., 1999, 1996]. An aqueous solution of fluorescein (200 µM in Na-salt in 100 µM Tris-HCl pH 8) was filled in a custom-made chamber of approximately 1 ml volume. This assured molecular diffusion to act as source of signal replenishment while reducing the effects of triplet state population and bleaching on the detected fluorescence signal. Variations in fluorescence signal with scan speed can therefore be approximated to be predominately derived from the system's scan speed dependent signal amplification. The chamber was sealed with a coverslip (0.17 mm thickness) and imaged using identical detector/amplifier and scanning speed settings as for the RPE specimen.

The fluorescence signal variation of fluorescein with scan speed is shown in Figure 6.1 for two consecutive runs, the first one starting at 1.92 µs/pixel toward longer dwell times, and the second one starting at 102.4 µs/pixel toward shorter dwell times. The corresponding dark image was subtracted from every measurement point. For both directions, the measured fluorescence intensities for different pixel dwell times overlap quite well, confirming that photobleaching is not influencing the detected signal, and scan speed dependent variations are attributed to the system's internal signal amplification.

6.2 Signal Increase through Fast Scanning

Figure 6.2 shows the relative two-photon excited fluorescence intensity of a group of RPE cells normalized on the average value of fluorescein as a function of the pixel dwell time for two recorded runs at different locations within the specimen. Fig. 6.2 a was recorded starting at 1.92 µs/pixel toward longer dwell times, and suggests a substantial increase in fluorescence intensity for shorter pixel dwell times. However, as for each measurement point a molecule is hit by $\sim$ 11200 pulses, one might expect that photobleaching contributes to part of the signal decrease toward longer dwell times. This is confirmed in Fig 6.2 b starting at 102.4 µs/pixel toward shorter dwell times. In comparison to

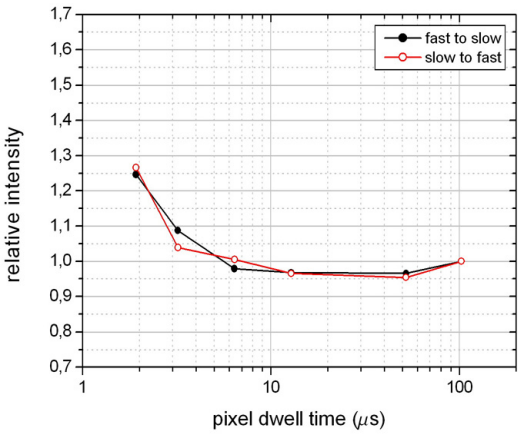

Figure 6.1: Relative detected fluorescence signal from fluorescein for different pixel dwell times used for system calibration. For each measurement point the same excitation dose was applied and the fluorescence emission was recorded as averaged signal over the corresponding number of frames.

Fig. 6.2 a, the signal increase is repressed, confirming that photobleaching is partially contributing to the results. If photobleaching was the only factor accounting for the signal decrease throughout a measurement run, the fluorescence intensity variations in Fig. 6.2 a and 6.2 b should be more or less symmetric. This suggests another physical influence of scan speed on signal variation which might be explained by considering the fluorophore's photophysics.

Applying the fluorescence model in Figure 6.3, a fluorophore faced to an illumination laser pulse is excited by the simultaneous absorption of two photons from its ground state S_0 to the first excited state S_1. Fluorescence then occurs upon relaxation from S_1 back to S_0, or the fluorophore gets trapped in a relatively long-lived triplet state T_1, which can relax, with or without emission of a photon, back to S_0 or undergoes photodissociation and irreversibly exits the fluorescence process to a bleached state. Popular bleaching pathways are generated over the highly reactive excited triplet state T_1 prone to undergo photodynamic interactions with environmental molecular oxygen [Diaspro et al., 2006]. Further excitations of T_1 to $T_{n>1}$, as well as the multi-photon events or the absorption of a second photon by a molecule in S_1 in the excited singlet state $S_{n>1}$ are assumed to all degrade into a bleached state. The typical fluorescence lifetime of organic fluorophores is in the order of 1 ns whereas excited triplet state lifetimes are typically in the order of 1 µs. Once a molecule is trapped in the long-lived triplet state T_1, it cannot relax to the ground state before the next pulse hits in and consequently does not contribute to a fluorescence signal. Furthermore, molecules in T_1 are prone to secondary excitation to higher excited states which likely degrade via photobleaching. The longer the effective illumination time of the fluorophore t_{eff}, compared to the excited triplet state lifetime, the more molecules get quenched in non-fluorescing dark states which reduces the amount of available molecules for the fluorescence process and effectively lowers the average detected intensity over the corresponding pixel dwell time. Short dwell times therefore

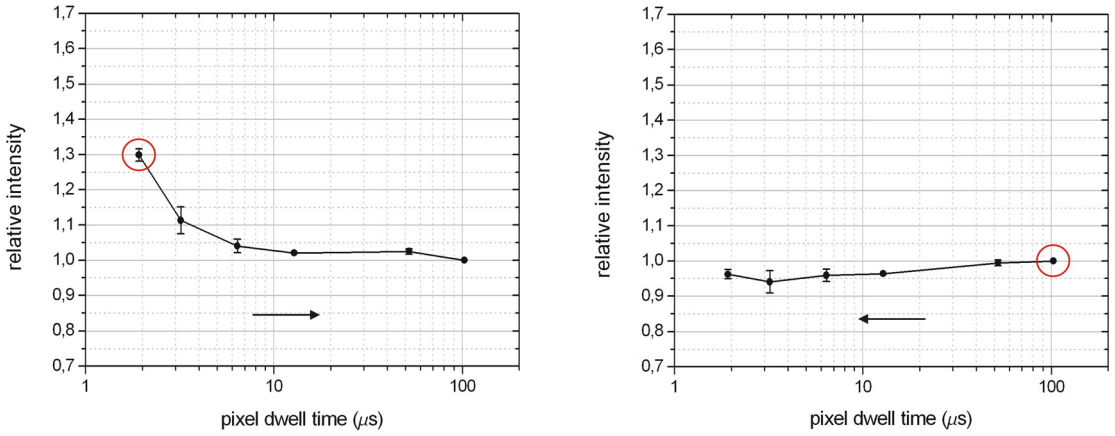

(a) (b)

Figure 6.2: Dependency of fluorescence yield on pixel dwell time for RPE lipofuscin normalized on the relative signal of fluorescein; the red circle indicates the starting point for each run.

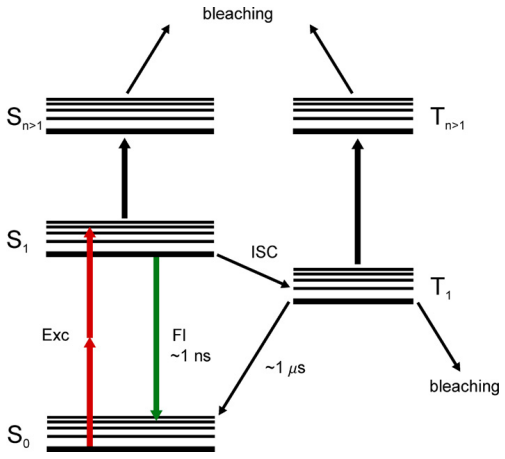

Figure 6.3: Energy diagram of the major molecular pathways of a typical fluorescent molecule upon absorption of a photon pair (Exc) for fluorescence (Fl), intersystem crossing (ISC), and photobleaching. Singlet states: S_0, S_1, $S_{n>1}$; triplet states: T_1, $T_{n>1}$. The lifetime of the first excited singlet state S_1 is in the order of 1 ns, whereas that of long-lived exited triplet state T_1 is in the order of a few µs.

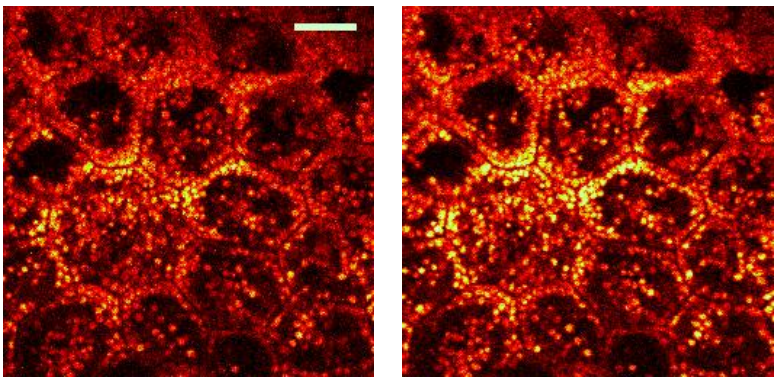

(a) 102.4 µs/pixel (b) 1.92 µs/pixel

Figure 6.4: RPE cells imaged at a pixel dwell time of 102.4 µs/pixel (a), and 1.92 µs/pixel (b). Scale bar, 10 µm.

result in lower triplet population, which leads to less ground depletion and less multi-step photobleaching. Further, as triplet states are allowed to completely depopulate during repetitive scans, the integrated fluorescence emission is potentially increased by suppressing the accumulation of triplets.

Regarding the phototoxic properties of lipofuscin in RPE cells and its ability to produce ROS [Gaillard et al., 1995; Rózanowska et al., 1995; Avallet et al., 2005; Pawlak et al., 2002; Boulton et al., 2004], lipofuscin can be expected to have a high intersystem crossing rate to the triplet state from where it might transfer its energy to molecular oxygen (which is a triplet in ground state) to its singlet excited state. It can therefore be assumed that faster scanning speeds effectively increase the detected fluorescence signal from lipofuscin due to less ground depletion. A more detailed study, however, including more measurement points is required to confirm the above initial experimental assumptions.

A direct comparison of a two-photon excited fluorescence image taken at 102.4 µs/pixel followed by another at 1.92 µs/pixel for the same location within the specimen of RPE cells, is shown in Figure 6.4. In both cases the dark image is subtracted and normalized on fluorescein for the corresponding scan speed. Even though the illumination dose is the same, a signal increase of $\sim 25\%$ is achieved in the fast scanning mode.

The ideal scan speed would require succeeding pulses to illuminate different molecules. This is achieved for an effective illumination time shorter than $t_{\text{eff}} = 12.5$ ns. For the above configuration, this equals a pixel dwell time of ~ 10 ns. Our results however indicate that for fluorophores with a high bias for triplet state crossing, a relief can already be expected for lower speeds, which might be an explanation for the high two-photon excited fluorescence signal achieved with our resonant ophthalmoscopic scanner ($t_{\text{eff}} = 1.25$ µs, i.e. 95 pulses per molecule) described above.

7 TPEF for the *Living* Human Eye?

In the following chapter, the feasibility of two-photon excited fluorescence for diagnostic purposes on RPE cells in the living human eye will be discussed in terms of achievable resolution, and laser safety according to the ANSI Z136.1-2000 Standard.

7.1 Resolution

The performance of an optical system for imaging the living eye is ultimately limited by the eye's focusing optics (cornea and lens). The human eye has an optimistic numerical aperture of approximately 0.3[1].

A 10×/0.3 W water immersion objective (Achroplan, Zeiss) was available on the Zeiss LSM 510 NLO microscope that could be used to approximate the eye's optical performance for imaging the RPE layer. From Eqs. (3.67) and (3.68), the two-photon lateral and axial FWHM resolution are calculated to be about 1 µm and 15 µm, respectively. In Figure 7.1 the RPE layer from a 55-year-old human donor eye is shown. For better estimation of the eye's imaging conditions, the image size was chosen to be approximately identical to the retinal field of view in the human eye using the smallest scan angle available on our modified ophthalmoscope, i.e. 170 µm × 170 µm.

The laser excitation power used for imaging at the specimen was 6–7 mW . The RPE cells are outlined by their containing fluorescent lipofuscin granules near the cell membrane. Also individual granules are clearly resolved for quantitative evaluation of their topographic distribution within the cell.

It should be noted that optical errors caused by the eye's optics, can strongly degrade the illumination PSF on the retina and reduce the detected signal and resolution. This effect is even more pronounced for larger pupil sizes. For a pupil size of approximately 3 mm the best compromise between pupil size and aberrations is achieved [Bille et al., 2003]. For smaller pupil sizes, image quality is limited by diffraction, whereas for larger pupil sizes, resolution is adversely affected by aberrations at the marginal areas (away from the optical axis) of the human eye. These are in particular spherical aberration, coma, and trefoil. Distortions in the excitation beam provoke a lateral and axial broadening of the focal spot, accompanied by a reduction in the focal intensity and hence, a loss of the two-photon excitation efficiency causing a reduction in the amplitude of the detected signals. Increasing the excitation power to compensate for the lower focal

[1] For a relaxed emmetropic eye with a dilated pupil size of 8 mm in diameter.

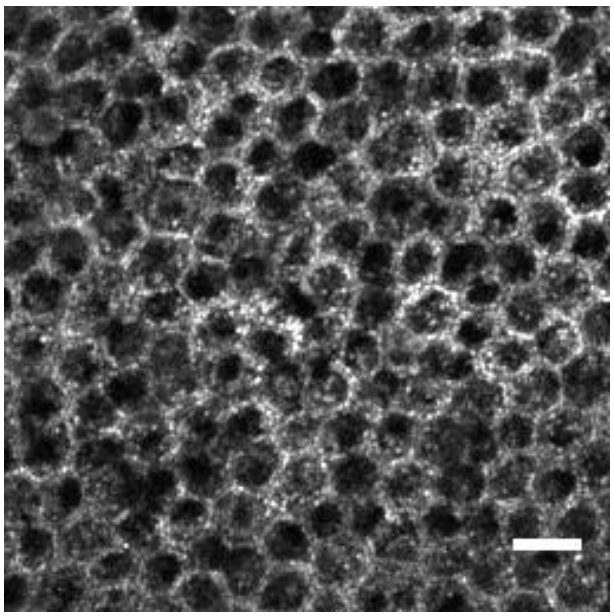

Figure 7.1: Two-photon excited autofluorescence imaging of RPE cells from a 55-year-old human donor eye using a low NA objective (10×/0.3 W Achroplan, Zeiss). The image size is identical to the retinal field of view in the human eye using the smallest scan angle available on our modified ophthalmoscope of section 4.3.1. Scale bar, 20 µm.

intensity is rarely desirable in ophthalmology as one is always concerned to minimize retinal exposure to radiation.

Because a large pupil size is necessary to maximize the achievable numerical aperture of the human eye, the optimal performance of a two-photon ophthalmoscope can only be achieved in combination with adaptive optics, capable of measuring and actively compensating for the eye's "large-pupil" aberrations. In an adaptive-optical system the wavefront distortion due to aberrations is conventionally measured by a wavefront sensing device, e.g. a Hartmann-Shack sensor, and used as feedback to a wavefront correction device, e.g. a deformable mirror, in a closed-loop system. Adaptive optics have been successfully applied to scanning laser ophthalmoscopy in the history of our research group for aberration-free confocal retinal imaging [Dreher et al., 1989; Müller, 2001; Zhang et al., 2008] and are readily applicable to nonlinear ophthalmoscopy for pre-shaping of the excitation beam [Bille et al., 2008].

7.2 Laser Safety Considerations

Due to its imaging characteristics, the retina is particularly vulnerable to injury from radiation. Focusing by the cornea and the lens can cause light intensities high enough to potentially damage the retina. Extensive radiation exposure to the retina always gives rise to degenerative changes involving vision loss. As for a potential in vivo application of the described nonlinear SLO for diagnostic fundus imaging in disease abatement, the excitation laser power has to be applied non-invasively to the eye and special considerations on laser safety are essential. Hazardous retinal effects are possible upon optical radiation in the visible and near infrared regions (400–1400 nm) as it is transmitted through the ocular media with little loss of intensity. This is also referred to as the *retinal hazard region*. Wavelengths outside this spectral band are primarily absorbed in the cornea and the lens.
The majority of the optical radiation reaching the retina is absorbed in the melanin granules of the RPE, the optically most dense absorbing layer. Consequently the RPE is the most sensitive and vulnerable site upon radiation exposure. However, the retina absorbs very little radiation in the NIR band compared to visible light, thus reducing the relative effectiveness for causing retinal injury.

The effects of optical radiation on the eye vary greatly with wavelength, exposure duration and retinal spot size. Retinal injury occurs principally from three mechanisms, each having its own interaction duration and/or wavelength region where it is the principle cause of threshold injuries [Delori et al., 2007; Sliney and Wolbarsht, 1980]:
Thermal damage, where the absorbed radiation photon energy by melanin in the RPE is transfered to molecular kinetic energy, resulting in a macroscopic temperature rise inducing protein denaturation. For exposure durations longer than the thermal relaxation time (~ 20 µs), heat can dissipate out of the exposed area during the exposure and the

energy needed to produce retinal damage increases with less than a linear dependence on exposure duration ($t^{0.75}$ dependence). For exposure durations shorter than ~ 20 µs, injury will take place before any significant heat flow, as the absorbed energy is confined to the irradiated volume of tissue. The energy needed to produce retinal damage is then basically independent of exposure duration.
Photoacoustic damage is produced by short pulses (< 1 ns) and is associated with various nonlinear mechanisms such as laser-induced optical breakdown (LIOB), self-focusing, two-photon absorption leading to blue light injury radiation, etc., which further reduce the energy level to cause retinal injury compared to longer pulse durations.
Photochemical injury occurs at short wavelength visible radiation for exposure duration longer than ~ 1 s as a result of photo-oxidative insult to the photoreceptors and RPE lipofuscin pigments.

The maximum permissible exposure of the eye to laser sources is limited by laser safety thresholds. The most recent consensus standard providing guidance for the the safe use of lasers has been promulgated by the *American National Standards Institute (ANSI) Z136.1-2000*. It defines a *maximum permissible exposure (MPE)* value in units of radiant exposure ($\mathrm{J/cm^2}$) or irradiance ($\mathrm{W/cm^2}$) for the direct ocular exposure to optical radiation without adverse effects. It is based on the best knowledge available from actual biological injury thresholds gained from numerous experimental studies (mainly on monkeys and rabbits) that incorporate the above injury considerations for different combinations of exposure (interaction) duration, wavelength and retinal spot size in a more or less conservative way.

Tables A.1 and A.2 provide the relevant safety limits to be considered for thermal and photoacoustic damage for laser radiation in the optical spectrum of 700–1049 nm and exposure durations from 100 fs to 3×10^4 s for direct intrabeam viewing. Figure 7.2 gives a graphic representation of the intrapupillary maximum permissible beam power (MPP in watts) at 831 nm for different collimated single-pulse laser exposure durations following Table A.1. The function of t reflects how the risk of injury varies with exposure time and the spectral factor A indicates the spectral variations in the risk. Photochemical damage is specified for a 400–600 nm wavelength band and is consequently irrelevant for the further considerations on safety limits of our nonlinear SLO operating at 831 nm excitation wavelength.

In the retinal hazard region, i.e. 400–1400 nm, the aperture area over which the incident radiation can be averaged is determined by the pupil of the eye. The ANSI Standard defines a pupil size of 7 mm (i.e. an area of 0.385 $\mathrm{cm^2}$) which corresponds to the maximum natural pupil dilation. Another assumption in the Standard is the minimal retinal image of a collimated beam, which was chosen to be 25 µm in diameter (1.5 mrad visual angle $\alpha_{\min}$), corresponding to the smallest experimentally observed thermal lesions upon laser radiation.
Even though a collimated laser beam would not be considered as an extended light source, the correction factors in Table A.2 have to be considered for scanning laser devices where

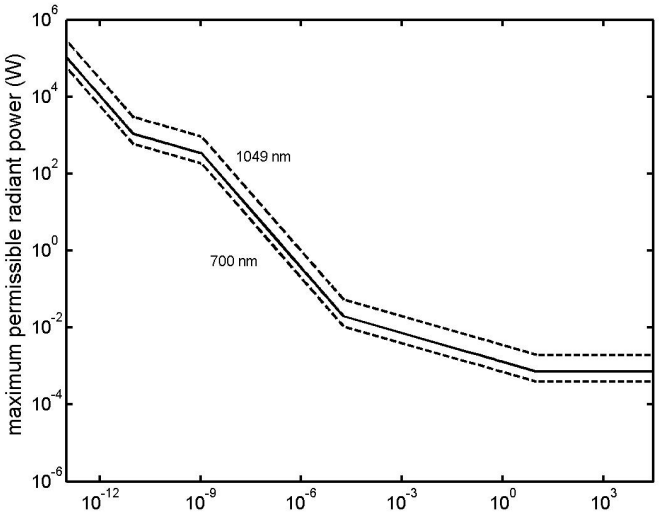

Figure 7.2: Intrapupillary maximum permissible beam power (in watts) at 831 nm (*solid curve*) for collimated single-pulse laser exposure according to Table A.1.

the laser beam is imaged over a large retinal area corresponding to a viewing angle $\alpha > \alpha_{\min}$. For a rectangular scanning field on the retina, one derives the correction factor B from Table A.3.

The tissue's reaction to ultrashort laser pulse radiation is relatively unknown. As already mentioned above, pulse durations smaller than the thermal relaxation time $t_{\min}$ are usually not associated with additive thermal effects. At high pulse repetition rates however, as commonly encountered in two-photon microscopy, the damage threshold from multiple laser pulses is anticipated to approach the CW laser threshold with the same average power, and is accurately predicted by thermal models [Thomas et al., 2002]. The ANSI Standard defines a critical pulse repetition rate $f_{cr} = 1/t_{\min}$ of 55.5 kHz (for $400 < \lambda < 1049$ nm) above which damage thresholds from repetitively-pulsed lasers become indistinguishable from CW exposures of duration $T = n/f$, where n is the number of pulses and f the pulse repetition rate.

The ANSI standard does not specify a clear maximum permissible radiation threshold for laser scanning devices. The most commonly used simulation for the MPE of a fast scanning SLO is that of a CW beam uniformly dispersed over the entire scanning field [Delori et al., 2007], considering the scanned laser beam as an extended light source of the retinal dimensions $0.48° \times 0.48°$ (or 8.4 mrad $\times$ 8.4 mrad)[2]. The following calculations

[2]The smallest scan angle of $1.6° \times 1.6°$ available on our modified ophthalmoscope translates to

imply that the laser beam is blocked during retrace of the scanner. The frame rate f is 20.83 Hz including a 16 ms dead time between consecutive frames used for retrace of the scanner, i.e. the active time per frame (the time to illuminate the extended source once) is 32 ms for a 256 × 256 pixels scan field at 8 kHz horizontal frequency.
Consecutive frames can than be simulated as pulsed exposure of duration $t = 32$ ms. The maximum permissible laser power at the cornea can be calculated using Tables A.1 and A.3 from

$$\mathrm{MPP}_{beam} = n^{-0.25}\ 6.93 \times 10^{-4}\ A\ \left(\frac{4\alpha}{\pi\alpha_{\min}}\right)\ t^{-0.25}, \tag{7.1}$$

where the factor $n^{-0.25}$ accounts for the cumulative effect of multiple pulses of duration t according to the ANSI Standard[3], with n the number of frames during the total exposure time.
For a stack of 32 images the MPP_{beam} value thus calculates to 9 mW. For a single frame, the laser power can be increased up to 21 mW.

As seen in section 7.1, the average illumination power required for imaging the human fundus in two-photon excited fluorescence mode in combination with adaptive optics, is below the threshold calculated from the ANSI Standard. For a MPP value of 7 mW, the acquisition can even be increased up to 86 frames for better SNR. The calculated value should however be approached with caution, as there is probably no perfect method to determine the potential retinal hazards from a SLO. Furthermore, the tissue's response to ultrashort pulses is relatively unknown and the complexity of the damage mechanisms probably does not allow a general conclusion. The Standard does not explicitly account for injury effects by repetitively pulsed ultrashort pulses. By simply modeling a CW illumination, blue-light mediated photochemical effects that might occur from ultrashort pulse exposures due to two-photon absorption processes are not considered.
The above MPP value can be increased by either choosing a larger scan angle, although at the expense of digital resolution, or by increasing the frame acquisition time by implementing a faster scanner.
As the excitation laser for two-photon excited fluorescence imaging only needs to be switched on during image acquisition, one can use a low power laser in reflection mode to align the retinal exposure site and thus limit the exposure time to the fs-laser. Eye movements that occur during acquisition can be compensated by appropriate software where image motions are calculated from the relative displacements of characteristic spatial structures within one image for subsequent averaging.

$0.48^\circ \times 0.48^\circ$ at the retina according to Table 4.3.1.
[3]The rule essentially tests whether an exposure by a long pulse of duration $n \cdot t$ is safe.

8 Conclusion and Outlook

In the present dissertation, a novel two-photon epifluorescence microscope, based on the fast scanning unit of a conventional scanning laser ophthalmoscope (Heidelberg Retina Tomograph HRT), was designed and developed for non-invasive structural and functional imaging of the human retina. The scan angle was modified for high-resolution optical 'zooming' at $0.48^\circ \times 0.48^\circ$ (smallest scan setting), corresponding to a retinal field of view of approximately 170 µm × 170 µm. The prototype was further extended for comparative confocal single-photon excited fluorescence imaging. The photodiodes for detecting the single- and two-photon excited fluorescence light are replaceable by a spectrometer for direct quantitative analysis of the spectral characteristics of the specimen region in focus. Using this prototype, the autofluorescence properties of the retina from human donor eyes have been successfully studied for their diagnostic value. To our knowledge, this is the first application of fast two-photon excited fluorescence (TPEF) imaging on endogenous fluorophores of the human retina toward a potential ophthalmoscopic application for fundus autofluorescence imaging on a cellular level. The image quality of the fast scanning ophthalmoscope-based microscope is comparable to that achieved with commercial two-photon microscopes [Han et al., 2006, 2007], with the advantage of resonant scanning (20.83 Hz frame rate). Fast scanning is required for imaging the living eye to compensate for inter-frame eye movements.

In a first application toward a feasibility study of two-photon ophthalmoscopy in the living eye, we studied the retinal pigment epithelium (RPE) from human donor eyes. The high-resolution selective visualization of RPE lipofuscin is of particular interest in ophthalmology, as alterations in RPE lipofuscin are features of the pathophysiology of retinal degenerative disease. Excessive accumulations of lipofuscin might reflect metabolically stressed RPE cells and are hypothesized to be responsible for the pathogenesis of age-related macular degeneration (AMD) prior to clinically apparent pathologic manifestations. High resolution in vivo functional characterization of the RPE might therefore reveal new insights in the understanding of the mechanisms that trigger this important sight impairing disease of yet unknown origin.

We could demonstrate a strong autofluorescence of the RPE cells upon two-photon excitation in the NIR at moderate average excitation powers. Single cytoplasmic lipofuscin granules that accumulate with age and disease in the lysosomal compartments of the RPE cells were clearly outlined by their intrinsic fluorescence. The two-photon imaging modality showed a substantial increase in depth resolution and contrast compared to single-photon excitation using the same optical configuration. TPEF imaging is able to

resolve a narrow optical layer absent of out-of-focus glare with no practical constraints on achieved resolution by a confocal pinhole. Simulating the emmetropic living eye's imaging conditions at a numerical aperture of 0.3 in combination with the small scan field, we proved that it is still possible to evaluate individual lipofuscin granules for a morphological and topographic analysis within the RPE cell. According to the maximum permissible laser exposure limit for NIR illumination following the newest ANSI Z136.1-2000 Standard, the two-photon ophthalmoscope was calculated to be non-invasive for diagnostic in the human eye.

We are the first to report on imaging individual photoreceptors and the overlying ganglion cell bodies and axons (retinal nerve fibers) in the intact human neural retina upon two-photon excitation of their endogenous fluorophores. Profiting from the advantages of NIR excitation, the highly complex and fragile "transparent" retinal neurons can be selectively studied in their natural environment, requiring neither labeling nor slicing. This could be useful in retinal disease experiments to potentially provide fresh insights in the overall understanding of the pathology causing ganglion cell death in a number of optic neuropathies. In particular, the important open question whether glaucoma is the result of an axonal insult or whether its origins are found in the ganglion cell soma might be addressed. However, overall higher average excitation power was necessary to yield an adequate fluorescence signal as compared with RPE imaging, which may restrict this method to basic research in experimental studies with appropriate animal models.

Further, the fluorescence yield dependency on pixel dwell time was probed on a commercial two-photon microscope with variable scan speed. We experimentally found an increase in RPE fluorescence yield upon fast scanning, presumably as a result of repressed triplet sate build up. These findings favor the use of resonant scanning devices in the excitation of fluorophores with a high crossing rate to the long-lived triplet state where illumination power is to be minimized, and support the use of fast scanning devices for two-photon ophthalmoscopy on RPE cells.

Regarding the present ex vivo results, it is demonstrated that endogenous retinal fluorophores provide functional information on retinal health upon fast two-photon excitation. The high-resolution in vivo capability of the novel two-photon scanning laser ophthalmoscope has the potential to provide new insights in the understanding of pathogenic mechanisms of retinal dysfunction that cannot be appreciated with current methods of fundus imaging. The resolution and selectivity for monitoring single cells in their natural environment is essential to advance our understanding in the physiological and biological processes in the normal and diseased retina.
The full capability and reach of information gained by the newly developed device will, however, ultimately only be appreciated in medical or biological applications of retinal disease experiments.

A number of improvements on the prototype are possible, in particular for increasing the two-photon efficiency in order to minimize the excitation power level in potential in vivo applications:

The avalanche photodiode implemented in the setup might, due to its relatively small active area, not be the best choice when imaging in scattering tissue as only a small fraction of the fluorescence light can be refocused and reach the detector. Most of the scattered fluorescence photons that still carry useful in-focus information are not detected. The contribution of ballistic fluorescence photons becomes even negligible several hundred microns deep in strongly scattering tissue [Helmchen and Denk, 2005]. Improved detection sensitivity is achieved with a large area PMT in non-descanned mode which assures to collect ballistic as well as scattered photons. Especially when imaging the living eye, the blue/green fluorescence light is strongly scattered in the different ocular media, especially in the cornea, and is prevented from reaching the "confocal" detector. A non-descanned detection scheme further simplifies the optical setup at the benefit of a minimum number of optical surfaces in the emission pass, resulting inherently in improved detection efficiency.

In order to further minimize unnecessary retinal exposure to radiation, the excitation beam should be blanked during scanner turnaround and flyback by an acousto-optical modulator (AOM), which is also used to modulate the excitation beam intensity.

In order to benefit from the full numerical aperture of the human eye at large pupil size and achieve an in vivo resolution comparable to the presented ex vivo results, a combination of the two-photon ophthalmoscope to adaptive optics is mandatory. "Large-pupil" aberrations degrade the efficiency of the two-photon excitation process, and its optimal performance, both in resolution and signal strength, can only be restored when actively compensating for the eye's aberrations. First experiments in this direction are in preparation [Bille et al., 2008]. In an idealized setup, the aberrations of the human eye are measured by a Hartmann-Shack wavefront sensor. Defocus is compensated via a telescope or a compact prism design located in between the scan and the tube lens, which is also used as z-scan (along the optical axis) to control the focal depth. The eye's remaining aberrations, i.e. astigmatism, trefoil, and spherical aberration, are compensated by a deformable mirror. Wavefront measurements are conducted with a low power IR laser diode and the wavefront of the two-photon excitation beam is modulated (pre-shaped) to compensate for the aberrations of the human eye. As the excitation laser only needs to be switched on during image acquisition, the same low power laser diode can be used in confocal reflection mode to align the retinal exposure site. A schematic of an optical setup, implementing the above considerations, for the next step of adaptive-optical two-photon fluorescence fundus imaging is illustrated in Figure 8.1.

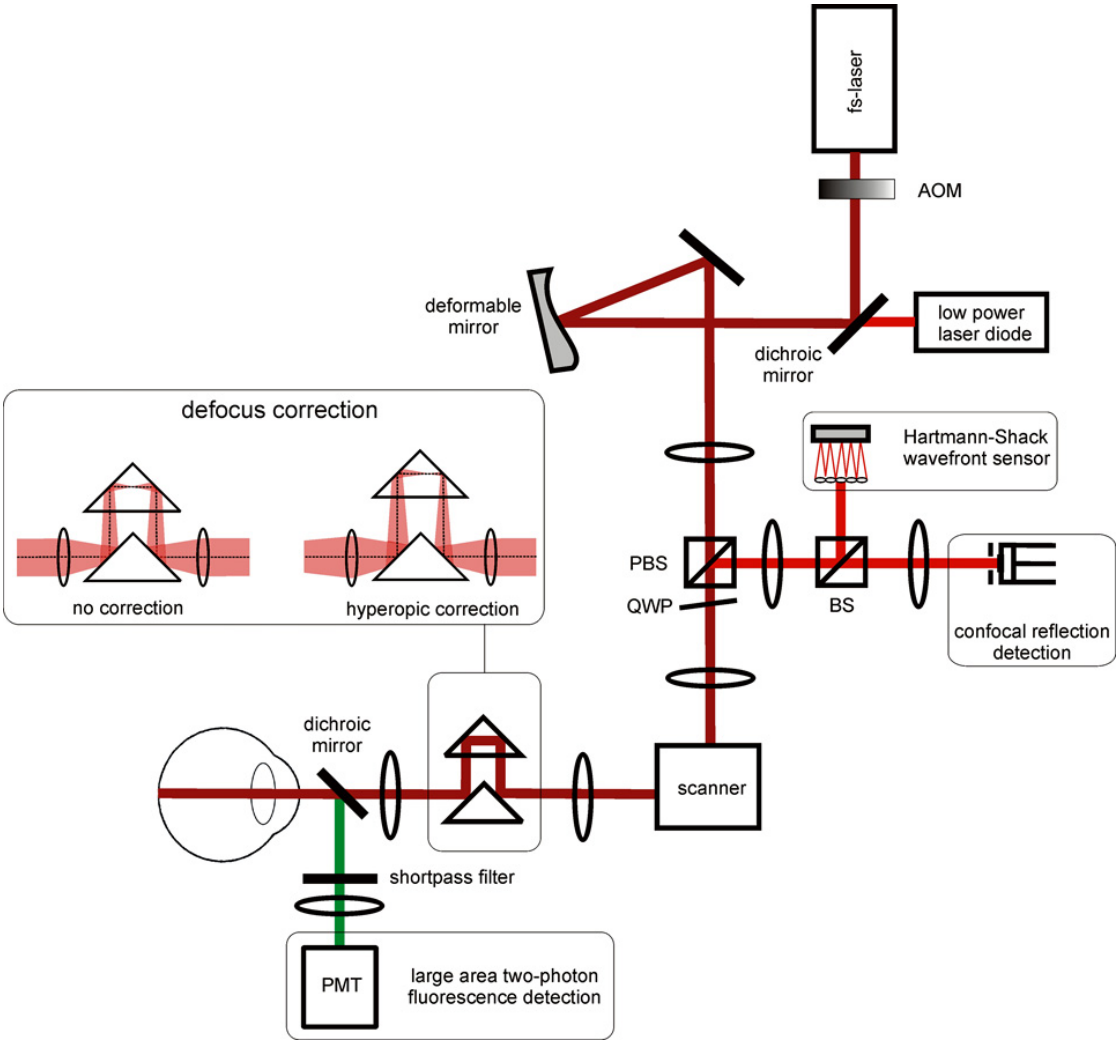

Figure 8.1: Idealized adaptive-optical setup for in vivo two-photon fundus imaging.

A Laser Safety

Tables to be used in the calculation of the maximum permissible exposure MPE (in J/cm^2) and corresponding maximum permissible beam power MPP (in W) at the cornea (7 mm pupil) for direct ocular exposure in the 700–1049 nm wavelength band, according to the ANSI Z136.1-2000 Standard [ANSI, 2000].

Table A.1: Maximum permissible exposure (MPE) and corresponding maximum permissible beam power (MPP) at the cornea (7 mm pupil) for direct ocular exposure for single-pulse laser radiation in the 700–1049 nm wavelength band, according to the ANSI Standard. Wavelength-dependent correction factor $A = 10^{0.002(\lambda-700)}$.

exposure duration t	MPE (J/cm^2)	MPP (W)
10 s to 3×10^4 s	$1.8 \times 10^{-3}\ A\ B\ C^{-0.25}\ t$	$6.93 \times 10^{-4}\ A\ B\ C^{-0.25}$
18 µs to 10 s	$1.8 \times 10^{-3}\ A\ B\ t^{0.75}$	$6.93 \times 10^{-4}\ A\ B\ t^{-0.25}$
1 ns to 18 µs	$5 \times 10^{-7}\ A\ B$	$1.93 \times 10^{-7}\ A\ B\ t^{-1}$
10 ps to 1 ns	$2.7\ A\ B\ t^{0.75}$	$1.04\ A\ B\ t^{-0.25}$
100 fs to 10 ps	$1.5 \times 10^{-8}\ A\ B$	$5.77 \times 10^{-9}\ A\ B\ t^{-1}$

Table A.2: Correction factors B and C depending on visual angle α defined as full angular subtense of retinal area measured from the center of pupil (in mrad), to be used in Table A.1. $\alpha_{\min} = 1.5$ mrad, $\alpha_{\max} = 100$ mrad.

visual angle α	B	C
$\alpha \leq \alpha_{\min}$	1	10
$\alpha_{\min} < \alpha \leq \alpha_{\max}$	$0.667\ \alpha$	$10^{0.0102(97+\alpha)}$
$\alpha > \alpha_{\max}$	$6.67 \times 10^{-3}\ \alpha^2$	100

Table A.3: Correction factor B for exposures in rectangular areas. α_{L} and α_{W} denoting the length and width of the rectangular field, respectively. After [Delori et al., 2007].

exposure area	B	visual angle
rectangular	$\frac{8\alpha_{\mathrm{L}}\alpha_{\mathrm{W}}}{\pi\alpha_{\min}(\alpha_{\mathrm{L}}+\alpha_{\mathrm{W}})}$	$\alpha_{\mathrm{W}} < \alpha_{\max}, \quad \alpha_{\mathrm{L}} < \alpha_{\max}$
	$\frac{8\alpha_{\mathrm{L}}\alpha_{\mathrm{W}}}{\pi\alpha_{\min}(\alpha_{\max}+\alpha_{\mathrm{W}})}$	$\alpha_{\mathrm{W}} < \alpha_{\max}, \quad \alpha_{\mathrm{L}} \geq \alpha_{\max}$
	$\frac{4\alpha_{\mathrm{L}}\alpha_{\mathrm{W}}}{\pi\alpha_{\min}\alpha_{\max}}$	$\alpha_{\mathrm{W}} \geq \alpha_{\max}, \quad \alpha_{\mathrm{L}} \geq \alpha_{\max}$
square	$\frac{4\alpha}{\pi\alpha_{\min}}$	$\alpha < \alpha_{\max}$
	$\frac{4\alpha^2}{\pi\alpha_{\min}\alpha_{\max}}$	$\alpha \geq \alpha_{\max}$
slit	$\frac{8\alpha_{\mathrm{L}}}{\pi(\alpha_{\mathrm{L}}+\alpha_{\min})}$	$\alpha_{\mathrm{W}} = \alpha_{\min}, \quad \alpha_{\mathrm{L}} < \alpha_{\max}$
	$\frac{8\alpha_{\mathrm{L}}}{\pi(\alpha_{\max}+\alpha_{\min})}$	$\alpha_{\mathrm{W}} = \alpha_{\min}, \quad \alpha_{\mathrm{L}} \geq \alpha_{\max}$

Bibliography

ANSI (2000). *American National Standard for Safe Use of Lasers*. ANSI Z136.1-2000 (The Laser Institute of America).

Avallet, L. B., Dillon, J., Tari, S., and Gaillard, E. R. (2005). A new approach to measuring the action spectrum for singlet oxygen production by human retinal lipofuscin. *Photochem. Photobiol.*, 81(6):1347–1350.

Bellmann, C., Rubin, G. S., Kabanarou, S. A., Bird, A. C., and Fitzke, F. W. (2003). Fundus autofluorescence imaging compared with different confocal scanning laser ophthalmoscopes. *Br. J. Ophthalmol.*, 87(11):1381–1386.

Bhutto, I. A., McLeod, D. S., Hasegawa, T., Kim, S. Y., Merges, C., Tong, P., and Lutty, G. A. (2006). Pigment epithelium-derived factor (PEDF) and vascular endothelial growth factor (VEGF) in aged human choroid and eyes with age-related macular degeneration. *Exp. Eye Res.*, 82(1):99–110.

Bille, J. F., Agopov, M., Alvarez-Diez, C., Han, M., Korablinova, N., von Pape, U., La Schiazza, O., Schwingel, M., Zhang, H., and Müller, F. (2008). Compact adaptive optics system for multiphoton fundus imaging. *J. Mod. Opt.*, 55(4–5):749–758.

Bille, J. F., Büchler Costa, J., and Müller, F. (2003). Optical quality of the human eye: The quest for perfect vision. In Bille, J. F., Harner, C. F. H., and Loesel, F. H., editors, *Aberration-Free Refractive Surgery. New Frontiers in Vision*, pages 25–46. Springer Verlag, Berlin, Heidelberg, third edition.

Bindewald, A., Bird, A. C., Dandekar, S. S., Dolar-Szczasny, J., Dreyhaupt, J., Fitzke, F. W., Einbock, W., Holz, F. G., Jorzik, J. J., Keilhauer, C., Lois, N., Mlynski, J., Pauleikhoff, D., Staurenghi, G., and Wolf, S. (2005a). Classification of fundus autofluorescence patterns in early age-related macular disease. *Invest. Ophthalmol. Vis. Sci.*, 46(9):3309–3314.

Bindewald, A., Jorik, J. J., Roth, F., and Holz, F. G. (2005b). cSLO-Fundusautofluoreszenz-Imaging. *Ophthalmologe*, 102(3):259–264.

Bindewald-Wittich, A., Han, M., Schmitz-Valckenberg, S., Snyder, S., Giese, G., Bille, J. F., and Holz, F. G. (2006). Two-photon-excited fluorescence imaging of human RPE

cells with a femtosecond Ti:Sapphire laser. *Invest. Ophthalmol. Vis. Sci.*, 47(10):4553–4557.

Bok, D. (2002). New insights and new approaches toward the study of age-related macular degeneration. *Proc. Natl. Acad. Sci. U.S.A.*, 99(23):14619–14621.

Borlinghaus, R. T. (2006). MRT letter: High speed scanning has the potential to increase fluorescence yield and to reduce photobleaching. *Microsc. Res. Tech.*, 69(9):689–692.

Born, M. and Wolf, E. (1980). *Principles of Optics*. Pergamon Press, Oxford, sixth edition.

Boulton, M., Docchio, F., Dayhaw-Barker, P., Ramponi, R., and Cubeddu, R. (1990). Age-related changes in the morphology, absorption and fluorescence of melanosomes and lipofuscin granules of the retinal pigment epithelium. *Vision Res.*, 30(9):1291–1303.

Boulton, M., McKechnie, N. M., Breda, J., Bayly, M., and Marshall, J. (1989). The formation of autofluorescent granules in cultured human RPE. *Invest. Ophthalmol. Vis. Sci.*, 30(1):82–89.

Boulton, M., Rózanowska, M., Rózanowski, B., and Wess, T. (2004). The photoreactivity of ocular lipofuscin. *Photochem. Photobiol. Sci.*, 3(8):759–764.

Bourla, D. H. and Young, T. A. (2006). Age-related macular degeneration: A practical approach to a challenging disease. *J. Am. Geriatr. Soc.*, 54(7):1130–1135.

Boyd, R. W. (2003). *Nonlinear optics*. Academic Press, San Diego, second edition.

Brakenhoff, G. J., Blom, P., and Barends, P. (1979). Confocal scanning light microscopy with aperture immersion lenses. *J. Microsc.*, 117:219–232.

Centonze, V. E. and White, J. G. (1998). Multiphoton excitation provides optical sections from deeper within scattering specimens than confocal imaging. *Biophys. J.*, 75(4):2015–2024.

Chen, C., Tsina, E., Cornwall, M. C., Crouch, R. K., Vijayaraghavan, S., and Koutalosz, Y. (2005). Reduction of all-trans retinal to all-trans retinol in the outer segments of frog and mouse rod photoreceptors. *Biophys. J.*, 88(3):2278–2287.

Conchello, J.-A. and Lichtman, J. W. (2005). Optical sectioning microscopy. *Nat. Methods*, 2(12):920–931.

Cox, G. and Sheppard, C. J. R. (2004). Practical limits of resolution in confocal and non-linear microscopy. *Microsc. Res. Tech.*, 63(1):18–22.

Cremer, C. and Cremer, T. (1978). Considerations on a laser-scanning-microscope with high resolution and depth of field. *Microsc. Acta*, 81(1):31–44.

Delori, F. C., Dorey, C. K., Staurenghi, G., Arend, O., Goger, D. G., and Weiter, J. J. (1995a). In vivo fluorescence of the ocular fundus exhibits retinal pigment epithelium lipofuscin characteristics. *Invest. Ophthalmol. Vis. Sci.*, 36(3):718–729.

Delori, F. C., Fitch, K. A., and Gorrand, J.-M. (1990). In-vivo characterization of intrinsic fundus fluorescence. Noninvasive assessment of the visual system. *J. Opt. Soc. Am.*, 3:72–74.

Delori, F. C., Fleckner, M. R., Goger, D. G., Weiter, J. J., and Dorey, C. K. (2000). Autofluorescence distribution associated with drusen in age-related macular degeneration. *Invest. Ophthalmol. Vis. Sci.*, 41(2):496–504.

Delori, F. C., Goger, D. G., and Dorey, K. C. (2001). Age-related accumulation and spatial distribution of lipofuscin in RPE of normal subjects. *Invest. Ophthalmol. Vis. Sci.*, 42(8):1855–1866.

Delori, F. C., Staurenghi, G., Arend, O., Dorey, C. K., Goger, D. G., and Weiter, J. J. (1995b). In vivo measurement of lipofuscin in Stargardt's disease - fundus flavimaculatus. *Invest. Ophthalmol. Vis. Sci.*, 36(11):2327–2331.

Delori, F. C., Webb, R. H., and Sliney, D. H. (2007). Maximum permissible exposures for ocular safety (ANSI 2000), with emphasis on ophthalmic devices. *J. Opt. Soc. Am. A*, 24(5):1250–1265.

Denk, W. (2006). Multiphoton molecular excitation in laser-scanning microscopy. In Pawley, J. B., editor, *Handbook of Confocal Biological Microscopy*, pages 535–549. Springer Science+Business Media LLC, New York, third edition.

Denk, W., Delaney, K. R., Gelperin, A., Kleinfeld, D., Strowbridge, B. W., Tank, D. W., and Yuste, R. (1994). Anatomical and functional imaging of neurons using 2-photon laser scanning microscopy. *J. Neurosci. Methods*, 54(2):141–162.

Denk, W., Strickler, J. H., and Webb, W. W. (1990). Two-photon laser scanning fluorescence microscopy. *Science*, 248(4951):73–76.

Denk, W. and Svoboda, K. (1997). Photon upmanship: Why multiphoton imaging is more than a gimmick. *Neuron*, 18(3):351–357.

Diaspro, A., Chirico, G., Uasi, C., Ramoino, P., and Dobrucki, J. (2006). Photobleaching. In Pawley, J. B., editor, *Handbook of Confocal Biological Microscopy*, pages 690–702. Springer Science+Business Media LLC, New York, third edition.

Donders, F. C. (1855). Beiträge zur pathologischen Anatomie des Auges. *Arch. Ophthalmol.*, 1:106–118.

Donnert, G., Eggeling, C., and Hell, S. W. (2007). Major signal increase in fluorescence microscopy through dark-state relaxation. *Nat. Methods*, 4(1):81–86.

Dorey, C. K., Wu, G., Ebenstein, D., Garsd, A., and Weiter, J. J. (1989). Cell loss in the aging retina. Relationship to lipofuscin accumulation and macular degeneration. *Invest. Ophthalmol. Vis. Sci.*, 30(8):1691–1699.

Dreher, A. W., Bille, J. F., and Weinreb, R. N. (1989). Active optical depth resolution improvement of the laser tomographic scanner. *Appl. Opt.*, 28(4):804–808.

Egger, M. D. and Pétrăn, M. (1967). New reflected-light microscope for viewing unstained brain and ganglion cells. *Science*, 157(3786):305–307.

Eichner, D. (1958). Zur Histologie und Topochemie der Netzhaut des Menschen. *Z. Zellforsch. Mikrosk. Anat.*, 48(2):137–186.

Eldred, G. E. (1993). Age pigment structure. *Nature*, 364(6436):396.

Eldred, G. E. and Katz, M. L. (1988). Fluorophores of the human retinal pigment epithelium: Separation and spectral characterization. *Exp. Eye Res.*, 47(1):71–86.

Eldred, G. E. and Lasky, M. R. (1993). Retinal age pigments generated by self-assembling lysosomotropic detergents. *Nature*, 361(6414):724–726.

Enger, A. and Hell, S. W. (2006). Aberrations in confocal and multi-photon fluorescence micrsocopy induced by refractive index mismatch. In Pawley, J. B., editor, *Handbook of Confocal Biological Microscopy*, pages 404–413. Springer Science+Business Media LLC, New York, third edition.

Fan, G. Y., Fujisaki, H., Miyawaki, A., Tsay, R. K., Tsien, R. Y., and Ellisman, M. H. (1999). Video-rate scanning two-photon excitation fluorescence microscopy and ratio imaging with cameleons. *Biophys. J.*, 6(5):2412–2420.

Feeney-Burns, L., Hilderbrand, E. S., and Eldridge, S. (1984). Aging human RPE: Morphometric analysis of macular, equatorial and peripheral cells. *Invest. Ophthalmol. Vis. Sci.*, 25(2):195–200.

Framme, C., Roider, J., Sachs, H. G., Brinkmann, R., and Gabel, V.-P. (2005). Non-invasive imaging and monitoring of retinal pigment epithelium patterns using fundus autofluorescence - review. *Curr. Med. Imaging Rev.*, 1(1):89–103.

Gaillard, E. R., Atherton, S. J., Eldred, G., and Dillon, J. (1995). Photophysical studies on human retinal lipofuscin. *Photochem. Photobiol.*, 61(5):448–453.

Gauderon, R., Lukins, P. R., and Sheppard, C. J. (1999). Effect of a confocal pinhole in two-photon microscopy. *Microsc. Res. Tech.*, 47(3):210–214.

Geeraets, W. J. and Berry, E. R. (1968). Ocular spectral characteristics as related to hazards from lasers and other light sources. *Am. J. Ophthalmol.*, 66(1):15–20.

Gerritsen, H. C. and De Grauw, C. J. (1999). Imaging of optically thick specimen using two-photon excitation microscopy. *Microsc. Res. Tech.*, 47(3):206–209.

Göppert-Mayer, M. (1931). Über Elementarakte mit Zwei Quantensprüngen. *Ann. Phys.(Leipz.)*, 401(3):273–294.

Han, M., Blindewald-Wittich, A., Holz, F. G., Giese, G., Niemz, M. H., Snyder, S., Sun, H., Yu, J., Agopov, M., La Schiazza, O., and Bille, J. F. (2006). Two-photon excited autofluorescence imaging of human retinal pigment epithelial cells. *J. Biomed. Opt.*, 11(1):010501.

Han, M., Giese, G., Schmitz-Valckenberg, S., Bindewald-Wittich, A., Holz, F. G., Yu, J., Bille, J. F., and Niemz, M. H. (2007). Age-related structural abnormalities in the human retina-choroid complex revealed by two-photon excited autofluorescence imaging. *J. Biomed. Opt.*, 12(2):024012.

Haralampus-Grynaviski, N. M., Lamb, L. E., Clancy, C. M. R., Skumatz, C., Burke, J. M., Sarna, T., and Simon, J. D. (2003). Spectroscopic and morphological studies of human retinal lipofuscin granules. *Proc. Natl. Acad. Sci. U.S.A.*, 100(6):3179–3184.

Haralampus-Grynaviski, N. M., Lamb, L. E., Simon, J. D., Krogmeier, J. R., Dunn, R. C., Pawlak, A., Rózanowska, M., Sarna, T., and Burke, J. M. (2001). Probing the spatial dependence of the emission spectrum of single human retinal lipofuscin granules using near-field scanning optical microscopy. *Photochem. Photobiol.*, 74(2):364–368.

Harwerth, R. S. and Quigley, H. A. (2006). Visual field defects and retinal ganglion cell losses in patients with glaucoma. *Arch. Ophthalmol.*, 124(6):853–859.

Hell, S. W. (2005). Hochauflösende 3D-Lichtmikroskopie. In Bille, J. and Schlegel, W., editors, *Band 3: Medizinische Laserphysik*, Medizinische Physik, pages 179–314. Springer Verlag, Heidelberg.

Helmchen, F. and Denk, W. (2005). Deep tissue two-photon microscopy. *Nat. Methods*, 2(12):932–940.

Hoffmann, E. M., Zangwill, L. M., Crowston, J. G., and Weinreb, R. N. (2007). Optic disc size and glaucoma. *Surv. Ophthalmol.*, 52(1):32–49.

Holz, F. G., Bellman, C., Staudt, S., Schütt, F., and Völcker, H. E. (2001). Fundus autofluorescence and development of geographic atrophy in age-related macular degeneration. *Invest. Ophthalmol. Vis. Sci.*, 42(5):1051–1056.

Holz, F. G., Schütt, F., Kopitz, J., Eldred, G. E., Kruse, F. E., Volcker, H. E., and Cantz, M. (1999). Inhibition of lysosomal degradative functions in RPE cells by a retinoid component of lipofuscin. *Invest. Ophthalmol. Vis. Sci.*, 40(3):737–743.

Hooper, C. Y. and Guymer, R. H. (2003). New treatments in age-related macular degeneration. *Clin. Experiment. Ophthalmol.*, 31(5):376–391.

Hopt, A. and Neher, E. (2001). Highly nonlinear photodamage in two-photon fluorescence microscopy. *Biophys. J.*, 80(4):2029–2036.

Hoyd, W. F., Schlicke, B., and Eckelhoff, R. J. (1972). Fundoscopic appearance of a nerve-fibre-bundle defect. *Brit. J. Ophthal.*, 56(8):577–583.

Huang, S., Heikal, A. A., and Webb, W. W. (2002). Two-photon fluorescence spectroscopy and microscopy of NAD(P)H and flavoprotein. *Biophys. J.*, 82(5):2811–2825.

Imanishi, Y., Batten, M. L., Piston, D. W., Baehr, W., and Palczewski, K. (2004). Noninvasive two-photon imaging reveals retinyl ester storage structures in the eye. *J. Cell Biol.*, 164(3):373–383.

Jonkman, J. E. N. and Stelzer, E. H. K. (2002). Resolution and contrast in confocal and two-photon microscopy. In Diaspro, A., editor, *Confocal and Two-Photon Microscopy: Foundations, Applications, and Advances*, pages 101–151. Wiley, New York.

Kaiser, W. and Garrett, C. G. B. (1961). Two-photon excitation in CaF_2:Eu^{2+}. *Phys. Rev. Lett.*, 7(6):229–231.

Kennedy, C. J., Rakoczy, R. E., and Constable, I. J. (1995). Lipofuscin of the retinal pigment epithelium: A review. *Eye*, 9(6):763–771.

Kerrigan-Baumrind, L. A., Quigley, H. A., Pease, M. E., Kerrigan, D. F., and Mitchell, R. S. (2000). Number of ganglion cells in glaucoma eyes compared with threshold visual field tests in the same persons. *Invest. Ophthalmol. Vis. Sci.*, 41(3):741–748.

König, K. (2000). Multiphoton microscopy in life sciences. *J. Microsc.*, 200(2):83–104.

Kunz, W. S., Kuznetsov, A. V., Winkler, K., Gellerich, F. N., Neuhof, S., and Neumann, H. W. (1994). Measurement of fluorescence changes of NAD(P)H and of fluorescent flavoproteins in saponin-skinned human skeletal muscle fibers. *Anal. Biochem.*, 216(2):322–327.

Kuznetsov, A. V., Mayboroda, O., Kunz, D., Winkler, K., Schubert, W., and Kunz, W. S. (1998). Functional imaging of mitochondria in saponin-permeabilized mice muscle fibers. *J. Cell. Biol.*, 150(5):1091–1099.

Lois, N., Halfyard, A. S., Bird, A. C., and Fitzke, F. W. (2000). Quantitative evaluation of fundus autofluorescence imaged "in vivo" in eyes with retinal disease. *Br. J. Ophthalmol.*, 84(7):741–745.

Lois, N., Halfyard, A. S., Bunce, C., Bird, A. C., and Fitzke, F. W. (1999). Reproducibility of fundus autofluorescence measurements obtained using a confocal scanning laser ophthalmoscope. *Br. J. Ophthalmol.*, 83(3):276–179.

Mainen, Z. F., Maletic-Savatic, M., Shi, S. H., Hayashi, Y., Malinow, R., and Svoboda, K. (1999). Two-photon imaging in living brain slices. *Methods*, 18(2):231–239.

Masters, B. R. (1984a). Noninvasive corneal redox fluorometry. *Curr. Top. Eye Res.*, 4:139–200.

Masters, B. R. (1984b). Noninvasive redox fluorometry: How light can be used to monitor alterations of corneal mitochondrial function. *Curr. Eye Res.*, 3(1):23–26.

Minsky, M. (1961). Microscopy apparatus. United States patent 3013467.

Minsky, M. (1988). Memoir on inventing the confocal scanning microscope. *Scanning*, 10:128–138.

Müller, F. K. (2001). *Konzeption und Entwicklung eines adaptiv-optisch korrigierten Laser-Scanning Retina-Tomographen.* PhD thesis, Ruprecht-Karls-Universität, Heidelberg.

Nickells, R. W. (2007). Ganglion cell death in glaucoma: from mice to men. *Vet. Ophthalmol.*, 10(Suppl 1):88–94.

Nowak, J. Z. (2006). Age-related macular degeneration (AMD): pathogenesis and therapy. *Pharmacol. Rep.*, 58(3):353–363.

Odgen, T. E. (1980). Thickness of the retinal nerve fiber layer in primate eyes. *Arch. Ophthalmol.*, 98(9):1625–1629.

Odgen, T. E. (1984). Nerve fiber layer of the primate retina: morphological analysis. *Invest. Ophthalmol. Vis. Sci.*, 25(10):19–29.

Ogden, T. E. (1978). Nerve fiber layer astrocytes of the primate retina: morphology, distribution, and density. *Invest. Ophthalmol. Vis. Sci.*, 17(6):499–510.

Pawlak, A., Rózanowska, M., Zareba, M., Lamb, L. E., Simon, J. D., and Sarna, T. (2002). Action spectra for the photoconsumption of oxygen by human ocular lipofuscin and lipofuscin extracts. *Arch. Biochem. Biophys.*, 403(1):59–62.

Pawley, J. B. (2006). Fundamental limits in confocal microscopy. In Pawley, J. B., editor, *Handbook of Confocal Biological Microscopy*, pages 20–42. Springer Science+Business Media LLC, New York, third edition.

Periasamy, A., Skoglund, P., Noakes, C., and Keller, R. (1999). An evaluation of two-photon excitation versus confocal and digital deconvolution fluorescence microscopy imaging in Xenoptus morphogenesis. *Microsc. Res. Tech.*, 47(3):172–181.

Piston, D. W., Master, B. R., and Webb, W. W. (1995). Three-dimensionally resolved NAD(P)H cellular metabolic redox imaging of the in situ cornea with two-photon excitation laser scanning microscopy. *J. Microsc.*, 178(1):20–27.

Quigley, H. A. (1996). Number of people with glaucoma worldwide. *Br. J. Ophthalmol.*, 80(5):389–393.

Quigley, H. A. and Addicks, E. M. (1982). Quantitative studies on nerve fiber layer defects. *Arch. Ophthalmol.*, 100(5):807–814.

Quigley, H. A. and Sommer, A. (1987). How to use nerve fiber layer examination in the management of glaucoma. *Trans. Am. Ophthalmol. Soc.*, 85:254–272.

Radius, R. L. and Anderson, D. R. (1979). The histology of retinal nerve fiber layer bundles and bundle defects. *Arch. Ophthalmol.*, 97(5):948–950.

Reim, M. (1993). *Augenheilkunde*. Ferdinand Enke Verlag, Stuttgart, forth edition.

Renard, J.-P., Giraud, J.-M., May, F., Rigal-Sastourné, J.-C., Oubaaz, A., Reda, K., and Maurin, J.-F. (2005). Les lasers diagnostiques dans le glaucome: la polarimétrie à balayage laser (GDx VCC) et la tomographie confocale par balayage laser (HRT). *J. Fr. Ophthalmol.*, 28(2):177–184.

Rózanowska, M., Jarvis-Evans, J., Korytowski, W., Boulton, M. E., Burke, J. M., and Sarna, T. (1995). Blue light-induced reactivity of retinal age pigment in vitro generation of oxygen-reactive species. *J. Biol. Chem.*, 270(32):18825–18830.

Saleh, B. E. A. and Teich, M. C. (1991). *Fundamentals of Photonics*. Wiley, New York.

Sarna, T. (1992). Properties and function of the ocular melanin - a photobiophysical view. *J. Photochem. Photobiol. B*, 12(3):215–258.

Schmitz-Valckenberg, S., Bültmann, S., Dreyhaupt, J., Bindewald, A., Holz, F. G., and Rohrschneider, K. (2004). Fundus autofluorescence and fundus perimetry in the junctional zone of geographic atrophy in patients with age-related macular degeneration. *Invest. Ophthalmol. Vis. Sci.*, 45(12):4470–4476.

Schütt, F., Davies, S., Kopitz, J., Holz, F. G., and Boulton, M. E. (2000). Photodamage to human RPE cells by A2-E, a retinoid component of lipofuscin. *Invest. Ophthalmol. Vis. Sci.*, 41(8):2303–2308.

Schweitzer, D., Kolb, A., Hammer, M., and Anders, R. (2002). Zeitaufgelöste Messung der Autofluoreszenz - Ein Werkzeug zur Erfassung von Stoffwechselvorgängen am Augenhintergrund. *Ophthalmologe*, 99(10):776–779.

Schweitzer, D., Schenke, S., Hammer, M., Schweitzer, F., Jentsch, S., Birckner, E., Becker, W., and Bergmann, A. (2007). Towards metabolic mapping of the human retina. *Microsc. Res. Tech.*, 70(5):410–419.

Sheppard, C. J. R. and Choudgury, A. (1977). Image formation in the scanning microscope. *Opt. Acta*, 24(10):1051–1073.

Shiino, A., Haida, M., and Chance, B. B. B. (1999). Functional imaging of mitochondria in saponin-permeabilized mice muscle fibers. *Neuroscience*, 91(4):1581–1685.

Sliney, D. and Wolbarsht, M. (1980). *Safety with Lasers and other optical sources*. Plenum Press, New York.

Sommer, A., Katz, J., Quigley, H. A., Miller, N. R., Robin, A. L., Richter, R. C., and Witt, K. A. (1991). Clinically detectable nerve fiber atrophy precedes the onset of glaucomatous field loss. *Arch. Ophthalmol.*, 109(1):77–83.

Sommer, A., Miller, N. R., Pollack, I., Maumenee, A. E., and George, T. (1977). The nerve fiber layer in the diagnosis of glaucoma. *Arch. Ophthalmol.*, 95(12):2149–2156.

Song, J. M., Inoue, T., Kawazumi, H., and Ogawa, T. (1999). Determination of two photon absorption cross section of fluorescein using a mode locked titanium sapphire laser. *Anal. Sci.*, 15(6):601–603.

Song, L., Varma, C. A., Verhoeven, J. W., and Tanke, H. J. (1996). Influence of the triplet excited state on the photobleaching kinetics of fluorescein in microscopy. *Biophys. J.*, 70(6):2959–2968.

Sparrow, J. R., Nakanishi, K., and Parish, C. A. (2000). The lipofuscin fluorophore A2E mediates blue light-induced damage to retinal epithelial cells. *Invest. Ophthalmol. Vis. Sci.*, 41(7):1981–1989.

Squirrell, J. M., Wokosin, D. L., White, J. G., and Bavister, B. D. (1999). Long-term two-photon fluorescence imaging of mammalian embryos without compromising viability. *Nat. Biotechnol.*, 17(8):763–767.

Stelzer, E. H. K. (1998). Contrast, resolution, pixelation, dynamic range and signal-to-noise ratio: Fundamental limits to resolution in fluorescence light microscopy. *J. Micrsc.*, 189(1):15–24.

Strauss, O. (2005). The retinal pigment epithelium in visual function. *Physiol. Rev.*, 85(3):845–881.

Suter, M., Remé, C., Grimm, C., Wenzel, A., Jäättela, M., Esser, P., Kociok, N., Leist, M., and Richter, C. (2000). Age-related macular degeneration. *J. Biol. Chem.*, 275(50):39625–39630.

Tan, Y. P., Llano, I., Hopt, A., Würriehausen, F., and Neher, E. (1999). Fast scanning and efficient photodetection in a simple two-photon microscope. *J. Neurosci. Methods*, 92(1–2):123–135.

Teich, J. M. (1985). *The theory and development of a noninvasive retinal fluorescence scanner with application to early diagnosis of diabetic retinopathy*. PhD thesis, Massachusetts Institute of Technology, Cambridge, Massachusetts.

Theer, P., Hasan, M. T., and Denk, W. (2003). Two-photon imaging to a depth of 1000 µm in living brains by use of a $Ti:Al_2O_3$ regenerative amplifier. *Opt. Lett.*, 28(12):1022–1024.

Thomas, R. J., Noojin, G. D., Stolarski, D. J., Hall, R. T., Cain, C. P., Toth, C. A., and Rockwell, B. A. (2002). A comparative study of retinal effects from continuous wave and femtosecond mode-locked lasers. *J. Biomed. Opt.*, 31(1):9–17.

Tsien, R. Y., Ernst, L., and Waggoner, A. (2006). Fluorophores for confocal microscopy: Photophysics and photochemistry. In Pawley, J. B., editor, *Handbook of Confocal Biological Microscopy*, pages 338–352. Springer Science+Business Media LLC, New York, third edition.

Tuulonen, A., Lehtola, J., and Airaksinen, P. J. (1993). Nerve fiber layer defects with normal visual fields. Do normal optic disc and normal visual field indicate absence of glaucomatous abnormality? *Ophthalmology*, 100(5):587–597.

von Helmholtz, H. (1851). *Beschreibung eines Augen-spiegels zur Untersuchung der Netzhaut im lebenden Auge*. Forstner, Berlin.

von Rückmann, A., Fitzke, F. W., and Bird, A. C. (1995). Distribution of fundus autofluorescence with a scanning laser ophthalmoscope. *Br. J. Ophthalmol.*, 79(5):407–412.

von Rückmann, A., Fitzke, F. W., and Bird, A. C. (1997). Fundus autofluorescence in age-related macular disease imaged with a laser scanning ophthalmoscope. *Invest. Ophthalmol. Vis. Sci.*, 38(2):478–486.

Webb, R. H., Hughes, G. W., and Delori, F. C. (1987). Confocal scanning laser ophthalmoscope. *Appl. Opt.*, 26(8):1492–1499.

Weingeist, T. A., Kobrin, J. L., and Watzke, R. C. (1982). Histopathology of Best's macular dystrophy. *Arch. Ophthalmol.*, 100(7):1189–1200.

White, J. G., Amos, W. B., and Fordham, M. (1987). An evaluation of confocal versus conventional imaging of biological structures by fluorescence light microscopy. *J. Cell. Biol.*, 105(1):41–48.

Wilke, V. (1985). Optical scanning microscopy - the laser scan microscope. *Scanning*, 7(2):88–96.

Wilson, T. and Sheppard, C. (1984). *Theory and Practice of scanning optical microscopy.* Academic Press, New York.

Xu, C., Williams, R. M., Zipfel, W., and Webb, W. W. (1996). Multiphoton excitation cross-sections of molecular fluorophores. *Bioimaging*, 4(3):198–207.

Zeiss (2003). Confocal laser scanning microscopy. Zeiss brochure.

Zhang, H., Agopov, M., La Schiazza, O., and Bille, J. F. (2008). Rotating pairs of Zernike phase plates for compensating for the higher-order aberrations of the human eye. *J. Mod. Opt.*, 55(4–5):727–735.

Zhong, Y. S., Leung, C. K., and Pang, C. P. (2007). Glial cells and glaucomatous neuropathy. *Chin. Med. J.*, 120(4):326–335.

Zipfel, W. R., Williams, R. M., Christie, R., Nikitin, A. Y., Hyman, B. T., and Webb, W. W. (2003a). Live tissue intrinsic emission microscopy using multiphoton-excited native fluorescence and second harmonic generation. *Proc. Natl. Acad. Sci. U.S.A.*, 100(12):7075–7080.

Zipfel, W. R., Williams, R. M., and Webb, W. W. (2003b). Nonlinear magic: Multiphoton microscopy in the biosciences. *Nat. Biotechnol.*, 21(11):1369–1377.

List of Figures

Danksagung

Mein Dank gilt all denen, die zum Zustandekommen dieser Doktorarbeit beigetragen haben und mich in vielfältiger Weise unterstützt haben. Hierbei ein besonderes Danke an

Prof. Dr. Josef F. Bille, für die interessante Themenstellung im Gebiet der medizinischen Physik und die Betreuung der Doktorarbeit,

Prof. Dr. Dr. Christoph Cremer, für die freundliche Übernahme des Zweitgutachtens, und die Bereitstellung seines Titan-Saphir Lasers während der ersten kritischen Tests,

Prof. Dr. Winfried Denk, vom Max-Planck-Institut für medizinische Forschung Heidelberg, für die Nutzung seines Labors inklusive Titan-Saphir Laser und des Multiphoton Mikroskops am MPIMF,

Mikael Agopov, für zahlreiche, manchmal frustrierende Stunden im Labor,

Heidelberg Engineering GmbH, besonders Gerhard Zinser, Konrad and Wolfgang Dinter, Heino Krüger, Frank Müller, Jörg Fischer, für die technische Unterstützung am HRT,

Prof. Dr. Frank G. Holz, vom Universitäts-Augenklinikum Bonn, für die Bereitstellung der Spenderaugen,

Meng Han, für seine fachliche Hilfestellungen in den ersten Jahren,

Caroline Müllenbroich, fürs stundenlange Aushalten vorm Mikroskop,

allen Mitglieder der F1-Gruppe,

“Ministère de la Culture, de l’Enseignement Supérieur et de la Recherche, G.-D. de Luxembourg”, dem “Centre de Recherche Public Gabriel Lippmann”, und dem “Fonds National de la Recherche Luxembourg” für die finanzielle Unterstützung während dieser Doktorarbeit,

meinen Eltern Marie-Thérèse und Vincent La Schiazza, für die kontinuerliche, kompromisslose Unterstützung.

März 2008 Olivier La Schiazza